Cryogenic Instrumentation using Planar Inductor based Eddy Current Sensors

A Thesis

Submitted for the Degree of

Doctor of Philosophy

in the Faculty of Engineering

By

Pankaj Sagar

Department of Instrumentation and Applied Physics
Indian Institute of Science
Bangalore - 560 012
India

January 2019

Dedicated to my baby niece Leela..

You are the master of your own destiny.
No one and nothing can come between
you and your destiny except you.
Take the destiny by the horns and have fun.
-Kung Fu Panda

Declaration

I hereby declare that, the work embodied in this thesis entitled **"Cryogenic Instrumentation using Planar Inductor based Eddy Current Sensors"** is entirely original and is the result of investigations carried out by me in the Department of Instrumentation and Applied Physics, Indian Institute of Science, Bangalore, India under the supervision of Professor R. Karunanithi (CCT).

I further declare that this work has not formed the basis for the award of any degree, diploma, fellowship, associate ship or similar title of any other university or institution. In keeping with the general practice of reporting scientific observations, due acknowledgement has been made wherever the work described is based on the findings of other investigators. Any omission that might have occurred by oversight or error in judgment is regretted.

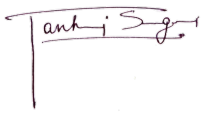

January 2019 **Pankaj Sagar**

Certificate

This is to certify that the thesis entitled **"Cryogenic Instrumentation using Planar Inductor based Eddy Current Sensors"** by Pankaj Sagar is a record of original bonafide work carried out under my guidance and has not been submitted to any other university or institute.

Prof. R. Karunanithi
Associate Professor
Centre for Cryogenic Technology
Indian Institute of Science,
Bangalore – 560012,
India

Acknowledgements

I have had the good fortune to have around me an abundance of friendly, kind, thought provoking and guiding personalities and science luminaries of great repute who made this period a truly remarkable and memorable one; helped me overcome many tough times and offered words of encouragement valuable advice when required. I take this opportunity to acknowledge, appreciate and thank all of them from the core.

First and foremost among them comes my supervisor - Prof. R. Karunanithi. I thank him from the bottom of my heart for his ever- readiness to guide, help and encourage me and for his enthusiasm and involvement in my research. His guidance and interest in my work has benefited me greatly, both scientifically and personally.

The former and present chairmen of the both the departments (CCT & IAP) have been kind in allowing access to department facilities when the need arose.

I would like to put on record my sincere and deep gratitude towards Mr. D. S. Nadig, Principal Research Scientist, CCT, IISc for his unconditional support and willingness to help even in the middle of night. The humanely side of his being has influenced me on more than one occasions. His calm demeanor and caring personality has left an indelible mark on my mind.

I would like to acknowledge Dr. T. S Datta of IUAC, New Delhi and Mr. Anand Yadav of RRCAT, Indore for providing me with Niobium samples of different RRR that was used to calibrate and develop the sensors.

A cordial, youthful and pleasant environment provided by all members of Centre for Cryogenic Technology, IISc ensured that I perform my research work with focus and aplomb. This would include but not limited to my senior in lab and the brotherly figure of Dr. Abhay Singh Gour, who guided me through the intricacies of doing experiments on cryogenics. I would like acknowledge his contributions

in me completing my thesis. I would also like to acknowledge the hard work, the dedication and help provided to me by Mr. Harris K. Hassan, without whom my work would not have progressed so smoothly. He provided me ears to bounce ideas, discuss new methods to do experiments and be there as a friend when I needed him the most. I would like to thank Ms. E. D. A Lakshmi, Ms. Gowri Nanda, Mr. Kashif Akber, Mr. Chandan Mahishi, Mr. Nagendra H. N. and Mr. Bharath G. J for providing me with any help I required at anytime as well as being my pillars of strength when times were rough.

I would also like to acknowledge the unconditional support provided by people who helped me with my work at different point of times. These include Mr. Gowtham Mahalingam, Mr. Sudharshan Gowda, Mr. Vignesh Krishna, Mr. Yash Hiremath, Mr. Umashanker H. P., Mr. Mallapa Achanur, Mr. Sai Guru Srinivas, Mr. Joewin Joy, Mr. Girish P. S., Mr. Pavan V. K., Mr. Ranjith G. R., Mr. Daniel F., Mr. Sandeep A. and Dr. Ravi Verma.

In particular, I would like to extend my heartfelt appreciation for the non-teaching staff in CCT lead by Mr. Raju H. C., Mr. Basavachari N., Mr. R. Rajendiran, Mr. Satisha G. V. and Mr. Muniraj G who worked tirelessly to provide me and the institute with sufficient amount of cryogen to conduct the experiments. I am thoroughly indebted to them and without whom my work would never have progressed beyond theoretical stage. I would also like to acknowledge other non-teaching staff of both the departments (CCT & IAP) notably, Mr. Upendra K. R., Mr Govinda, Mrs Veena and Mrs Udaya Kumari for all their support they provided me.

A number of friends in the Institute made my stay at IISc feel like an extension of a homely experience. I would like to acknowledge my close friends Ms. Jyothi Prabha G., Dr. Swati Balakrishnan, Dr. Tarandeep Singh, Dr. Aswani Kanchvrla, Dr. Chetana Daliga and Mr. Vijayanth for their support throughout my stay in IISc.

I wish to thank my closest friends Mr. Abdul Nazer, Mrs Neethu Agustine, Ms Tina Thomas, Mrs Vani Vijay, Mrs Renju Devassy and Mr Krishnaraj for their relentless support for every venture that I took. I would also like to thank Mrs. Meghana A. Gurjar, Mrs Jithu Priya, Mr Nipun Kumar A. and Mr Vishak M. G. for the fun times and relaxing trips that we had which gave me the focus and energy to finish this arduous endeavor.

Last but not least, my mother Anita Vidyasagar and my father S. Vidyasagar; they raised me, supported me, taught me, and loved me. I am indebted to them for inculcating in me the dedication and discipline to do well whatever I undertake. I am fortunate enough to receive the untiring love from my sister Pooja Sagar, my brother Prannoy Sagar, my brother-in-law Yadu Rajiv and my niece Leela K Rajiv, and their immense patience for tolerating my tantrums, stubbornness and mistakes. I am also blessed enough to have received unconditional love and support from my fiancé Soniya Chandran who entered as a pleasant surprise in my life. To them I dedicate this thesis.

Preface

Cryogenic sensors have become vital in measurement of crucial parameters in the modern scientific research. My thesis dissertation addresses the design, development and testing of PCB based planar inductors and associated cold electronics for different types of sensors working at cryogenic temperatures. PCB based sensors utilize commercial FR4 fabrication process involving layered bonding processes and selective etching to produce the required structure. Sensors that perform three different operations but use planar inductors are presented here.

The first sensor that was designed was a multilayer planar inductor based eddy current proximity/displacement transducer. First part of the work on the sensor involved the study of behavior of PCB (FR4) based multilayer inductors at low temperature. A structural analysis of the sensor was done using Ansoft structural analysis software. The structural changes (warping) that was observed in the simulation studies was experimentally verified using the variation of capacitance between the layers of the inductors when the sensor was cooled. This data was also compared with the Ansoft Maxwell models of the same sensors. The second part of the work used the designed multilayer inductor to develop a proximity sensor capable of working down to 4.2 K. Proximity/displacement of a metal surface/target in the range of 0-5 mm could be measured using this sensor. The use of a cold electronics based LC oscillator operating at 4.2 K using thermal cycled stable components was also reported. Effective realization of inductor based sensors require the signal conversion and signal conditioning elements to be as close to the sensing element as possible. This required me to develop electronic circuits which are capable of working at cryogenic temperatures without any drastic changes in parameters or at least predictable changes in parameters. A detailed study of performance analysis of unbuffered inverter based LC development is also discussed. This is a part of the sensor system used in the proximity sensor as

well as angular displacement sensor. The effect of temperature variation on cold electronics based LC Oscillator is analyzed. This variation in temperature causes oscillator to change its operating frequency. Certain additional harmonics are also introduced into the output waveform at the lower temperatures. Variation in the output of the oscillator is studied from 300 K to 4.2 K. The frequency modulated (FM) oscillator output is a function of displacement. Calibration of the developed sensor at cryogenic temperatures were performed to ascertain the sensitivity and repeatability. Impedance analysis of the planar multilayer inductor is presented and its Q-factor is determined. Experimental results of the noise characteristics of the oscillator at various temperatures are also discussed. The developed sensor has good thermal stability, sensitivity and repeatability at the cryogenic operating temperatures.

The second sensor was a cryogenically operated (down to 4.2 K) multilayer planar inductor array based eddy current angular position/rotation transducer. An array of four multi-layered coils is used to divide the 360° into four sectors of 90° each. Switching between each of the inductor is done by a cold electronics based multiplexer circuit coupled to an unbuffered inverter LC oscillator that has been described in the previous section. The angular displacement is a function of frequency of cold electronic LC oscillator. The pickup coil forms the inductor of the oscillator which is operated down to 4.2 K and uses thermal cycled stable components. The design and optimization of the rotor components are also discussed in detail. The change in frequency as a function of angular displacement was calibrated at cryogenic temperatures. The developed sensor was found to have good thermal stability, sensitivity and repeatability over the entire cryogenic range.

The final section describes different methods to measure the Residual Resistivity Ratio (RRR) of Nb samples. RRR is an important parameter that dictates the purity and in turn the performance of the Superconducting Radio Frequency (SRF) cavity at low temperatures ($\leq$ 4.2 K). The usual method of 4-wire electrical resistance measurement is both destructive in nature and produces a non-local (average) measurement of electrical conductivity. Here, a non-contact and local RRR measurement technique utilizing eddy current principle is presented utilizing multilayer planar inductor sensing element. Three different approaches are explored; all utilizing the impedance variation of the sensing coil and correlating it directly with the RRR of the sample. The initial approach uses the slope of

lift-off lines generated by the impedance variation when the conductivity of the Nb sample changes. The ratio of the slopes of the lift-off lines becomes equal to the ratio of the conductivity of the metal (RRR). The second approach correlates the inductance variation of the sensing coil with the RRR of the sample. Here the sensing element is coupled to a multiplexed cold electronics based LC oscillator. The changes in inductances are converted to changes in frequency and hence a calibration chart relating frequency to RRR is obtained. The third approach utilize the direct relation of the eddy current penetration depth of the conductivity of the metal. If a sample's conductivity increases, the penetration depth changes (decreases). So, in order to maintain a skin depth equal to the thickness of the sample, frequency has to be reduced. From the value of absolute inductance at these inflection frequency points, RRR can be calculated. It should also be noted that the principles used to measure the RRR of Nb samples can be extended to measure the conductivity change of any nonmagnetic metals at cryogenic temperatures. Here, a different approach is undertaken utilizing cold electronics based dual switched oscillator circuits to measure the impedance changes associated with the sensing element. Two different oscillator circuits are used in tandem to achieve the above. This switched oscillator circuit technique is used to determine the impedance of a cryogenic sensing coil at 295 K and 77 K with different metal targets kept at specific distances. Experimental data is compared with that of an impedance analyzer circuit and measurement errors are also presented.

Contents

List of Figures

List of Tables

Patent

[1] Pankaj Sagar, Abhay Singh Gour, and Karunanithi R. Multilayer planar inductor based proximity sensor and associated electronics operating down to liquid helium temperature, December 2016. IN Patent R20,164,035,984.

List of Journal Publications

[1] Pankaj Sagar, Abhay Singh Gour, and R Karunanithi. A multilayer planar inductor based proximity sensor operating at 4.2 k. *Sensors and Actuators A: Physical*, 264:151–156, 2017.

[2] P. Sagar, H.K. Hassan, and R. Karunanithi. A technique for measuring impedance of cryogenic eddy current sensors using dual switched oscillators. *Journal of Instrumentation*, 13(08):T08006, 2018.

[3] Pankaj Sagar, Harris K Hassan, Abhay Singh Gour, and R. Karunanithi. Multilayer planar inductor array based angular position sensor for cryogenic application. *Cryogenics*, 96(C):18–24, 2018.

[4] Abhay Singh Gour, Pankaj Sagar, and R Karunanithi. Investigation of cryogenic level sensors for ln2 and lox. *Cryogenics*, 84:76–80, 2017.

[5] Abhay Singh Gour, Pankaj Sagar, and R Karunanithi. Design, development and testing twin pulse tube cryocooler. *Cryogenics*, 86:87–96, 2017.

[6] Pankaj Sagar, Vignesh Krishna, Abhay S Gour, M Gowthaman, H Sudharshan, S Srinivasan, R Karunanithi, and S Jacob. Design and development of experimental setup to measure the rrr values of a thin film coated superconducting sample. *Indian Journal of Cryogenics*, 42(1):152–155, 2017.

[7] Pankaj Sagar, Abhay Singh Gour, and R Karunanithi. Capacitance level sensor with integrated cold electronics. *Indian Journal of Cryogenics*, 43(1):160–163, 2018.

[8] R Karunanithi, S Jacob, DS Nadig, MVN Prasad, Abhay S Gour, S Pankaj, M Gowthaman, and H Sudharshan. Calibration of a hts based lox 400 mm level sensor. *Physics Procedia*, 67:1169–1174, 2015.

[9] Abhay S Gour, Pankaj Sagar, H Sudharshan, R Karunanithi, and S Jacob. Hts based 400 mm level sensor for liquid nitrogen. *Indian Journal of Cryogenics*, 43(1):143–147, 2018.

List of Conference Publications

[1] Pankaj Sagar, Harris K. Hassan, E.D. A. Lakshmi, Kashif Akber, Girish P. S., and R Karunanithi. An eddy current based rrr measurement technique for srf cavities. In *27th International Cryogenic Engineering Conference and the International Cryogenic Materials Conference in 2018, Oxford UK, ICEC 27–ICMC 2018*. Elsevier B.V., 2018.

[2] Pankaj Sagar, R. Karunanithi, and Abhay Singh Gour. Effect of temperature variation on cold electronics based lc oscillator for rrr measurement. In *14th Cryogenics 2017*. IIR International Conference, 2017.

[3] Karunanithi R, Jacob S, D. S. Nadig, M.V.N. Prasad, Abhay S. Gour, Pankaj S, Gowthaman M, and Sudharshan H. Calibration of an hts based lox 400mm level sensor. In *25th International Cryogenic Engineering Conference and the International Cryogenic Materials Conference in 2014, ICEC 25–ICMC 2014,*, volume 67, pages 1169–1174. Elsevier B.V., 2014.

[4] Abhay S Gour, Joewin Joy, Pankaj Sagar, H Sudharshan, A Mallappa, R Karunanithi, and S Jacob. Experimental studies on twin ptcs driven by dual piston head linear compressor. In *IOP Conference Series: Materials Science and Engineering*, volume 171, page 012075. IOP Publishing, 2017.

Chapter 1

Introduction

1.1 Cryogenics: A short overview

The term Cryogenics was coined from the Greek words Kryos and genics which means pertaining to icy cold. Cryogenics is the science and technology of producing and measuring the cold- temperature and studying its effects. Nowadays, the cryogenic technology is used in various fields from the preservation of food to quantum computing. The cryogenic temperature is defined to be temperatures below 123K.

The lowest temperature existing in the universe is 2.7K. This temperature found in nature is dependent on the decoupled photons from the big bang and is diminishing continuously due to the expansion of universe. Nowadays, atoms and molecules are being cooled to temperature as low as 10^{-6} to about 500pK in condensed matter laboratories. The Large Hadron collider, which is the largest cryogenic system, has the main magnet operating at a temperature of 1.9K.

The origin of cryogenics can be traced back to the 19^{th} century where experiments were conducted by various scientists to liquefy the permanent gases. In 1825, Michael Faraday liquefied gases such as CO_2 and NH_3 by initially immersing the gases in ether and dry ice bath to cool it and then pressurizing it till it liquefied. By 1845, he had successfully managed to liquefy most of the then known gases. However, his method did not work with permanent gases such as oxygen, nitrogen and hydrogen. In the 1860s, Thomas Andrews determined the critical point in CO_2 isotherms (304K) which is a necessary condition required for liquefaction of

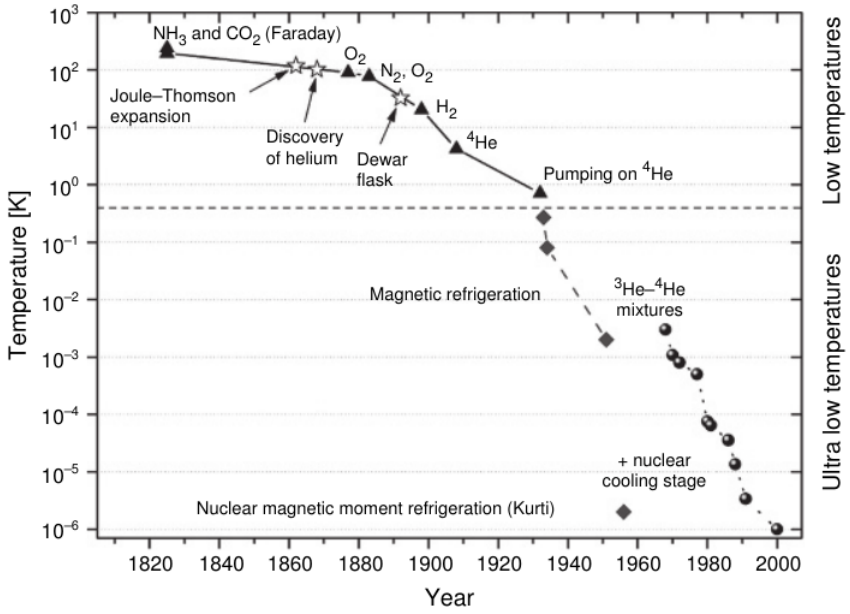

Figure 1.1: A historical overview of Cryogenics

a gas.

The year 1877 was the turning point for the cryogenics with the successful transportation of refrigerated meat using NH_3 refrigerator from Argentina to France and the liquefaction of oxygen at 90K by Louis Cailletet in France and Raoul Picted in Switzerland. Due to lack of good thermal insulation, the experiments proved to be difficult and it was only in 1883 at the University of Cracow, S.F. von Wroblewski and K.Olszwski obtained the liquid oxygen at 90K and liquid nitrogen in 77K.

James Dewar in 1898 was able to liquefy hydrogen at 14K using his silvered doubled-walled glass vacuum flask which is able to store cryogenic liquids for longer period before it evaporated. This was the lowest temperature achieved at that time. The successful liquefaction of hydrogen depended on Joule and Thomson's discovery of process of expansion and also on the use of dewar flasks or storage vessels. In 1902, Linde separated for the first time pure oxygen from air and by 1907, the first air liquefaction station was installed in USA. In the same year of 1902, Claude and Delorme formed L'Air Liquide which used the double pressure column for the separation of air. This yielded more efficiently in comparison to the Linde system of using expansion machine.

The successful liquefaction of hydrogen and oxygen lead to the next elusive gas to be liquefied. After the discovery of helium by Lockyer and Frankland during the solar eclipse in 1868, the first liquefaction of helium was done by Kamerling-Onnes at Leiden University in 1908. He had also observed the superfluidity in helium at the same time and superconductivity of mercury in liquid helium in the year 1911. Some of the major milestones in cryogenics are shown in the figure 1.1
The application of the cryogenics stemmed from various methods for obtaining low temperature. The production of the low temperature is via the usage of cryogens (Nitrogen, Helium etc).

1.2 Applications for cryogenics

Cryogenic technology is applied in numerous fields at present. It is used in several fields in such a way that it connects different fields due to the similarity in the application.

1. Storage and transport of gases
2. Separation of gases
3. Biological and medical applications
4. Altering material properties by reduced temperature
5. Electronics
6. Superconductivity

One of the common commercial applications of the cryogenics is the large scale storage and transportation of the liquefied gases such as (Liquefied Natural Gas) LNG. The transportation can be more efficiently done in a liquid form compared to gaseous form in terms of volume and weight. The liquid rocket propellants such as LOX and LH_2 stored in fuel tanks in rocket is another common application. These propellants are used due to the higher specific impulse (thrust produced per propellant mass consumed). Food industry is also using cryogenics for better quality and purity of food under storage, leading to the longer shelf life and for maintaining freshness while transporting them.

The separation of air and various other gas mixtures is a major application of cryogenics. This is based on the differences in the boiling points of various components in a gas mixture. This separation of gaseous mixture is used to obtain LOX, LN_2 and LH_2 of high purity which have several industrial applications.
In medical field, cryogenic technology is used for the storage and transportation of cellular structures such as blood plasma, for cancer treatment and cryosurgery using LN_2. Cryosurgery is done by the usage of liquid nitrogen to remove abnormal tissues.
Cryo-preservation is the process of preserving biological materials such as cells, tissues and organs. MRI (Magnetic Resonance Imaging) which is common imaging technique found in many hospitals works on the on NMR (Nuclear Magnetic Resonance) principles. It is non-invasive diagnostic tool to obtain the image of the tissues of organs such as brain, heart and also, of muscles and random growth found in the body. Liquid helium is used to submerge the superconducting magnetic coil to maintain the persistent mode of these magnets which are the main components of MRI systems.
As the temperature is reduced, the basic properties of the material are observed to vary. These changes of material properties at different temperature have a broad application in the engineering fields. Many components are required to be cryo-treated for a particular use in the industry. The cryo-treated components have increased wear resistance, toughness and reduced electrical resistance. The cryogenic sensors used in astronomical telescopes reduce the thermal effect and increase the signal to noise ratio to obtain a better image.
In the electronics industry, cryogenics is used extensively. The cooling of sensors and other electronic components can be done using cryogenics. At cryogenic temperatures, the performance of the electronics is improved due to low noise, increased efficiency, increased sensitivity and reduced losses. Many of the space missions require infrared, gamma ray and X-ray detectors that operate at cryogenic temperature.
The superconductivity has several scientific and industrial applications. It is used in fields such as particle physics, medical imaging etc. The application of this is based on the superconducting magnets cooled using liquid helium. These superconducting magnets are used in particle accelerators, magnetic levitation, MRI, NMR spectroscopy and power transmission. RF cavity used for particle acceler-

ators is made of high purity (higher Residual Resistivity Ratio) Niobium. This becomes superconductors at liquid helium temperature.

1.3 Cryogenic sensors

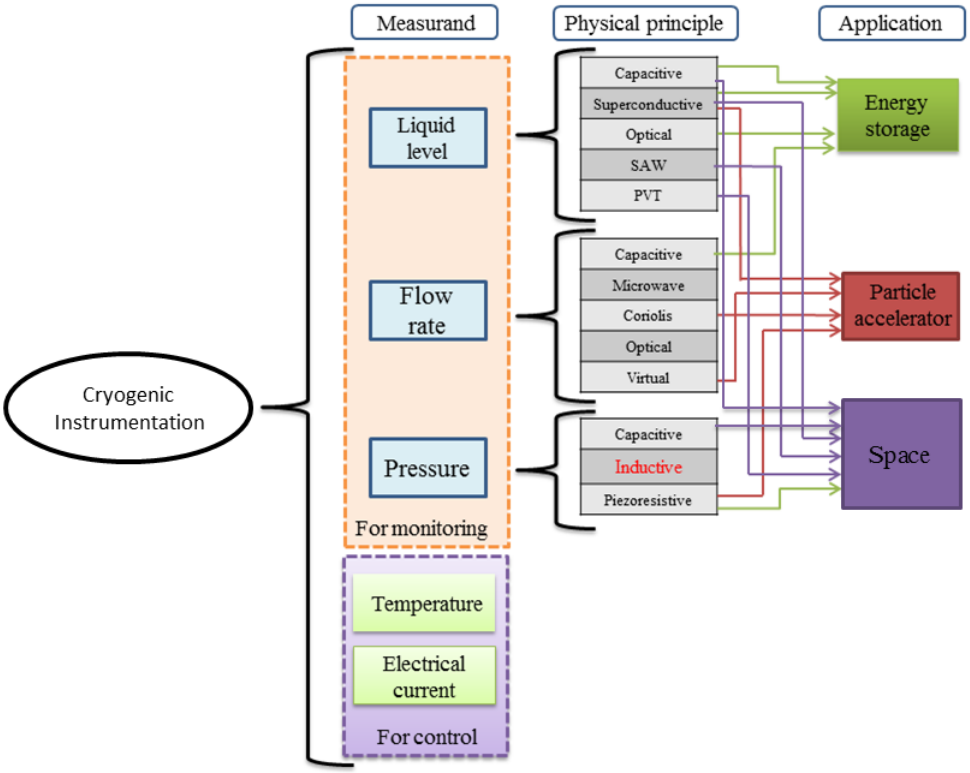

Figure 1.2: Measurements for cryogenics: Measurands are classified according to the use of the measurement system for monitoring or control. Among monitoring measurements, the most widely used physical principles are reported and related to the applications [Arpaia, P., De Vito, L., Pezzetti, M., Picariello, F., & Serio, L. (2018)]

In all of the applications discussed above, a prominent role is played by the objectives of the measurement systems ie., to provide accurate measurements for feedback in the process control systems, and to collect information for monitoring the physical properties of materials during the cryogenic process. These measurements are carried out by means of transducers which convert the physical variable

into a human readable format. There are may different types of sensors that have been developed specifically for cryogenic applications.

Some of the main quantities that are measured in cryogenic processes are (i) temperature (ii) flow rate (iii) pressure, (iv) Cryogen liquid level. In addition to these major parameters, many other parameters are also of significant importance like displacement (linear and angular) or separation (in cryogenic environment), electrical currents, magnetic fields, electrical conductivity, thermal conductivity etc.

Conventional temperature sensors like Resistive Temperature Detectors (RTDs) and thermocouples are extensively used in many cryogenic applications. But, for temperature ranges below 10 K, Negative temperature coefficient materials (Germanium RTDs, Cernox, Silicon diodes and Carbon resistors) provide higher sensitivity and finer resolution compared to conventional temperature measurement principles. The main advantage of these kinds of thermometry is the limited instrumentation required to measure the parameter.

Cryogenic flow sensors usually utilize capacitive measurement techniques that involves the sensing element (concentric tubes) that act as the plates of a capacitor and the dielectric medium will be the measured flowing liquid. There have also been sensors that use microwave based measuring techniques (Doppler shift in wavelengths) to accurately gauge the flow. Some sensors also utilize heating elements and its temperature stabilization as a gauge of the flow (hot wire anemometer). Many other techniques including mechanical Coriolis based sensors are also available in market.

Pressure measurements in cryogenic systems are generally carried out by room temperature sensors connected to the measurement point by small capillary tubes. This approach is often preferred because of ease of operating the sensors at ambient temperature and hence, a wider variety of sensors can be chosen and it offers the opportunity of easily replacing the sensor. Common principle of measurements include capacitive, inductive, piezoresistive sensing elements.

Level sensors are critical in cryogen level control. Usually capacitive sensors are preferred over other methods. There are many sensors that use high temperature superconductors as the sensing element, discrete diodes as a way to gauge the liquid gas interface, ultrasonic and laser based sensors etc.

Extensive research has gone into studying the major measured parameters and

many commercial products are available that can operate even down to milli Kelvin (mK) temperatures. A detailed analysis of most of these sensors can be found elsewhere [1].
This thesis will mainly deal with a very specific subclass of sensors which utilize inductive sensing element to measure particular parameters. This is of utmost importance, as there is very little research that has gone into this subclass of sensors.

1.4 Literature review

Insignificant amount of work has been done on designing and developing the eddy current sensors for cryogenic applications. A few that have been used have their own shortcomings and limitations. The main limitation of using inductance based sensors at cryogenic temperatures (eddy current sensors) is the requirement for long cable lengths to connect the sensing element with the signal processing element. This introduces a lot of errors in the measurement as the eddy current measurement technique may require the measurement of change in the real and imaginary components of the impedance of the sensing element. If long cables with varying temperatures along its whole length are used to connect the sensing element with the processing circuit, it will give rise to erroneous measurements. This problem can only be solved by either utilizing smart temperature compensation techniques or by utilizing cold electronics based signal processing elements which are kept as close to the sensing element as possible and designed as a part of the transducer capable of operating at cryogenic temperatures.
Here, a few of the key developments that took place in some of the areas that this dissertation focuses on are discussed in brief:-

1.4.1 Cryogenic proximity and angular position sensors

There are various sensors that are used for measuring linear and angular displacements such as optical encoders that can realize high resolution and accuracy, microwave based sensors that have the advantage of miniaturization and resolution, capacitive sensors that have good sensitivity and accuracy, etc. But very few of them can work effectively and maintain a consistent performance in cryogenic

temperatures. Some of the advancements in cryogenic linear and angular position sensing are detailed here.

- Studies on cryogenic proximity sensors were mainly undertaken by NASA. Main applications were the actuation of cryogenic vent or release valves. They tested the performance of a variable reluctance type cryogenic proximity sensor as and when it was cycled through various temperature transients. It was found that variable reluctance cryogenic position sensors can be a viable alternative to the mechanical switches that were used at that time [Cloyd, R. A. (1982) [2]]

- A detailed analysis for developing an eddy current based position sensor was put forward by S. D. Roach in 1998. He described the step by step procedure involved in design and selection of the sensing coil, the size and shape determination of the target and also the design of signal processing electronic system to obtain the desired parameters for the sensor. [Roach, S. D. (1998) [3]]

- In 1998, Backes K. A. et al, developed an inductive position sensor capable of operating at temperatures down to 4.2 K. The design was basically a modified Linear Variable Differential Transformer (LVDT). The sensor had a full scale reading of 1.4 cm with a sensitivity of 12 μm. The sensitivity could be improved by increasing the operating frequency of the primary coil and the sensor was found to be insensitive to thermal cycling. [Backes, K. A., & Brisson, J. G. (1998) [4]]

- Linear and angular position sensing in the harsh cryo-vacuum of space was a requirement for many space agencies including NASA. A team lead by Krause O. at Max Planck Institute for Astronomy developed a magnetoresistive position sensor that can operate at a temperatures of 2.7 K, with a very low power dissipation of $\sim$150 mW. The sensor design utilized four magnetoresistors biased by the collimated field of moving magnet arranged in a closed magnetic circuit. The magnetoresistors are connected to an electrical bridge circuit [Krause, O., Grözinger, U., Lemke, D., Böhm, A., & Hofferbert, R. (2001, September) [5]]

- A comparative study of two different types of position or displacement sensors in the temperature range of 300 K to 6 K and under strong magnetic fields ranging from 0 to 9T, are discussed in detail in by [Milushev, M., Süßer, M., & Wüchner, F. (2004) [6]]. These sensors were specifically tested for cryogenic environment and were used for the instrumentation of superconducting magnets and their test facility. They discovered that potentiometer based sensors were more suited for very high magnetic field environments and that strain gauges were strongly affected by magnetic fields beyond 3T.

- There have been many attempts to make the output of the displacement sensor independent of the temperature variations. One such work was published by Li, Q., & Ding, F. (2005) [7]. They utilized a non-inductive compensation coil along with the sensing coil, to compensate for the variations in temperature. Using this method, they were able to bring down the drift due to temperature from 12% for the uncompensated, to about 0.7% for the compensated sensor.

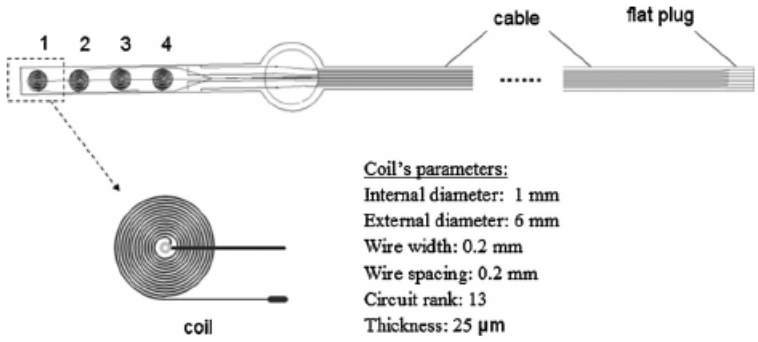

Figure 1.3: Schematic drawing of flat eddy current sensor probe [Wang, P., Fu, Z., & Ding, T. (2010)]

- In 2010, Wang P. et al., developed a frameless eddy current sensor utilizing flexible printed circuit board (FPCB) technology as shown in figure 1.3. They used manganese copper instead of the standard copper to design the inductor pattern. This enabled them to achieve good thermal stability and reduce the thermal drift. The sensor utilized an LC relaxation oscillator to convert the inductance changes into a readable frequency change. The sensor was tested from 20 K to 300 K and achieved a full scale range of 2

mm and a sensitivity of 0.2kHz/μm. [Wang, P., Fu, Z., & Ding, T. (2010)[8]]

- A non-contact inductive displacement sensor utilizing an inductive voltage divider circuit coupled to a floating wiper mechanism which feeds back the output voltage into a self balancing feedback type signal conditioning circuit were discussed by Rana, S. et al. A detailed error analysis and sensor parameters viz. sensitivity, repeatability, resolution, etc, were discussed. Another advantage is that the sensor was designed to be independent of the coupling capacitances that arises due to the air gap between the inductive element and the floating wiper.[Rana, S., George, B., & Kumar, V. J. (2017) [9]].

- Numerous designs for precise angular measurement sensors have been developed depending on the demands of the applications. In 2001 Irle, H and his team invented two separate angular measurement sensors. One utilized a stator element having an exciting coil with application of periodic AC voltage and several receiving coils. It also included a rotor element that affects the strength of inductive coupling between the exciting coil and receiving coils as a function of its angular position relative to the stator element Irle, H., Kost, N., & Schmidt, F. J. (2001). [10]. They also developed a design with a coupled LC oscillator with approximately identical design. By inductively coupling the oscillators, they synchronized themselves with respect to the frequency and phase relationship so that the undesirable mutual interference is prevented [11].

- A capacitive angular position sensor was developed by V. Ferrari et. al in 2003. The design composed of a static capacitive rotor and an electrically floating conductive rotor mechanism. There was a dielectric rotor segmented also with materials having different dielectric constants. A signal conditioning circuit was also developed to convert the capacitance changes into a readable voltage output. [Ferrari, V., Ghisla, A., Marioli, D., Taroni, A., Fasolato, P., Maggi, F., ... & Rossetti, V. (2003) [12]]

- In 2009, Bach G. invented an inductor based sensor which consists of a segmented rotor, a single primary coil and a number of secondary coils arranged in a symmetrical way, with respect to the axis of rotation. When it rotates,

the voltage associated with each of the secondary coil (connected in a differential manner) changes and hence, a readout of the rotor position was possible. [Bach, G., & Dockwiller, B. (2009) [13]]

- A through wall cryogenic angular displacement sensor that works effectively for cryo-vacuum environments was designed and tested by a team lead by Carapelle A. The sensor was designed specifically to operate for Ariane space vehicle and has a target sensitivity of 0.01°. The sensor was tested for temperatures ranging from 4 K to 300 K without any need for recalibration. The principle of operation was the closed magnetic paths for a pair of set of coils with a modified rotor element having a high permeability material embedded in it.[Carapelle, A., Martin, N., & Chantraine, T. (2013) [14]]

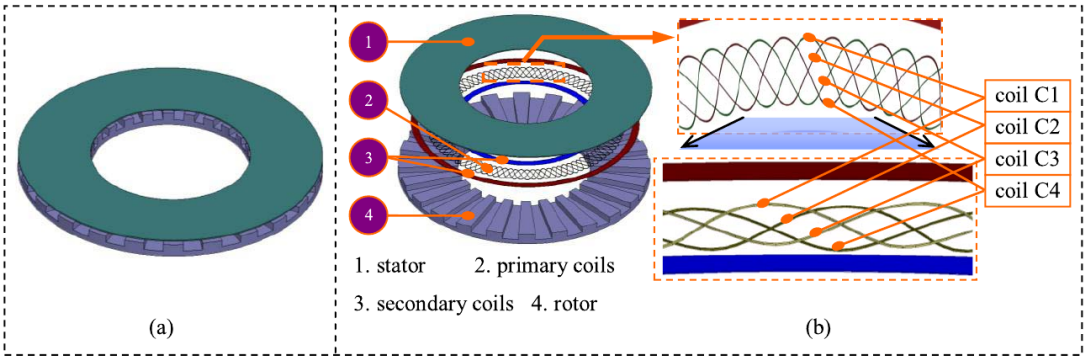

Figure 1.4: Structure diagram of the angular displacement sensor. (a) Overall view. (b) Exploded view. [Tang, Q., Peng, D., Wu, L., & Chen, X. (2015)]

- An inductive rotation sensor based on planar inductors utilizing PCB fabrication techniques was done by Tang Q. et al in 2015. It consists of a stator, a set of primary coils, a set of secondary coils and a slotted rotor design as can be seen in figure 1.4. The primary coils were excited by a 4 kHz signal and the output frequency was converted to voltage via a signal processing electronics. The sensor was shown to have a very high accuracy at ±12 arcsec and the sensor can be fabricated for lower cost due to its PCB based design. [Tang, Q., Peng, D., Wu, L., & Chen, X. (2015) [15]]

- A 3D hall probe angular position sensor was developed by a team lead by L. L. Gong for use in a cryogenic permanent magnet undulator. The calibration

procedure required for the hall probe is discussed in detail in this paper. They concluded that the three-dimensional magnetic fields of a cryogenic permanent magnet undulator can be received accurately by correcting these angle errors and position errors of Hall sensors [Gong, L. L., Chen, W., Kang, W., Sun, S. C., Li, Z. Q., Zhang, L., ... & Zhang, X. Z. (2017). [16]].

A detailed and exhaustive analysis of the literatures available shows that only a small amount of work has gone into characterizing and design of the inductor based sensors for cryogenic application. From the previous section, it can be concluded that only a single planar inductor based proximity sensor has been tested at cryogenic temperature (20 K) even though the requirement for them is ever increasing. There were no developments of angular displacement sensor based on eddy current principle operating at temperatures less than 10 K. Hence, there is need to develop inductive sensors that are capable of working in the cryo-vacuum condition of space and in the harsh cryo-module environment of accelerators.

1.4.2 Cold electronics and Cryogenic signal processing

For the eddy current sensors to become a viable alternative to presently available techniques at cryogenic temperatures, cold electronics has to be a key component of the sensor package. Usually the sensing element is mounted inside the cryostat and the signal conversion element is kept at room temperature, outside the cryostat. As eddy current sensors depend on the changes in both the real and imaginary components of impedance variation, the variations in the resistance of the connecting leads due to the temperature changes affect the sensor performance. This leads to large errors at lower temperatures which in turn resulted in the development of very few sensors for ≤ 10 K operations. Reduced temperature operation offers improvements in performance through improvement of materials-related properties such as electronic carrier mobility and electrical conductivity. Substantial improvements in reliability are also expected since degradation mechanisms are thermally activated. Some of the important literatures dealing with cold electronics is given below.

- A detailed review on the advantages of low temperature on the VLSI system was given by Kirschman in 1985. He described the technologies that can be implemented at cryogenic temperatures to fabricate high speed logic gates and low noise microwave amplifiers. Experimental results involving device parameters like device speed, heat removal, power consumed, noise improvements etc. were discussed in detail in this paper. He concluded that more research has to be done to study the effects of cold temperature on devices when high performance becomes an important parameter [Kirschman, R. K. (1985) [17]]
- A detailed testing of Commercial off the shelf Components (COTS) for Martian environment was conducted by a team from Kansa State University lead by Yogesh Tugnawat et. al., These COTS components include off-chip IF filters, off-chip TCXOs, and on-chip components such as MOSFETS, resistors and capacitors. The on-chip components are from a rad-hard Silicon-on-Sapphire (SOS) IC process. They tested the components from 293 K to 150 K and their use in the Martian environment was analyzed in detail [Tugnawat, Y., & Kuhn, W. (2005, October) [18].
- Most of the measurements in the field of cold electronics have been dedicated to space applications. For deep space missions, the sensors have to be capable of handling the cryo-vacuum existing in that environment. A study specifically dedicated for that was done by a team from NASA lead by R.L. Patterson. Cryogenic electronics could enhance efficiency of space systems, improve reliability, and simplify their design. This work focuses on the research and development of electronics suitable for space exploration missions. They also investigated the effects of cryogenic temperature and thermal cycling for commercial off the shelf components as well as for components specially developed for low temperature operation [Patterson, R. L., Hammoud, A., & Elbuluk, M. (2006). [19]].
- There has also been efforts to characterize the power electronics devices for cryogenic application. These will be helpful in designing future power electronic systems that are used to control the high tempera-

ture superconductor (HTS) power systems. They tested commercially available power diodes, power transistors, IGBTs etc. under cryogenic conditions. They gave details on the performance of such devices under liquid nitrogen temperatures and compared them to their room temperature performances.[Pereira, P., Valtchev, S., Pina, J., Gonçalves, A., Neves, M. V., & Rodrigues, A. L. (2008) [20]]

– Any microprocessor or microcontroller uses a crystal oscillator to generate the stable oscillations required for normal operation. The variation of crystal oscillator frequency at cryogenic temperatures was of great significance for designing robotic systems for deep space applications. Patterson R. et al., from NASA studied the effect of thermal cycling on a PX-570 crystal oscillator circuit. A detailed analysis on the circuit performance was discussed by Patterson, R., Hammoud, A., & Scherer, S. (2011) [21].

1.4.3 Eddy current sensors for conductivity measurements

Eddy current sensors as a non-destructive testing (NDT) method has been rapidly developing in the past decades. Eddy current testing can be done on any materials in which eddy currents (induced currents) can be generated. Eddy current sensors are really versitalile and can be used to measure a number of parameters of the target like cracks, position above the sensor, size, depth, direction, shape and electrical conductivity. This section will look into some of the earlier works that tried to measure the electrical resistivity of the target utizing eddy current principles.

– In 1961, R. G. Chambers showed that the resistivity of a sample can be deduced from the change in mutual inductance between two coils when the sample is inserted. The coils are arranged to form a Hartshorn bridge as shown in the figure 1.5. Through a simple transformer setup, he was able to measure resistivity of the order of 2×10^{-9} Ωcm [Chambers, R. G., & Park, J. G. (1961) [22]].

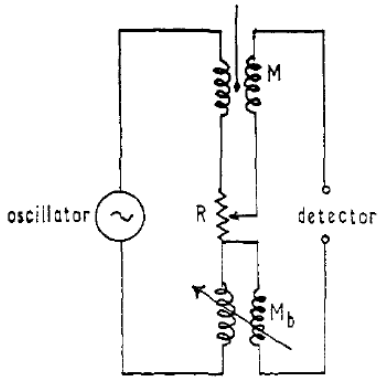

Figure 1.5: The Hartshorn bridge [Chambers, R. G., & Park, J. G. (1961)]

- Work on eddy current based sensing took off once the analytical model for eddy current probes with axial symmetry and different coil configurations was developed by C. V. Dodd and W. E. Deeds in 1968. The solutions are in the form of integrals of first-order Bessel functions giving the vector potential, from which the other electromagnetic quantities of interest were obtained. Truly remarkable aspect of his solutions was that an inverse problem could be generated and studied, which was later utilized to obtain the variations in the other depended terms from the changes to the sensing element [Dodd, C. V., & Deeds, W. E. (1968) [23]].
- Dodd, C. V., & Deeds, W. E. in the 1973 utilized computer simulations to deduce optimum conditions for performing thickness measurements of nonmagnetic metal sheets. They were able to simulate the effect of variations in conductor thickness, lift-off distances etc [Dodd, C. V. (1973) [24]]. A reflection type probe used to measure the effect of thickness of the target is shown in figure 1.6.
- In 1982 Free. G of American Society for Testing and Materials was able to develop the first high accuracy eddy current probe for measuring the conductivity of nonferrous materials [Free, G. (1981) [25]]. They developed an eddy current bridge circuit to evaluate the impedance changes of the sensing element
- In 1983 A.C Lynch and his team were able to measure the conductivities of surface layers of metals utilizing an eddy-current meter. The

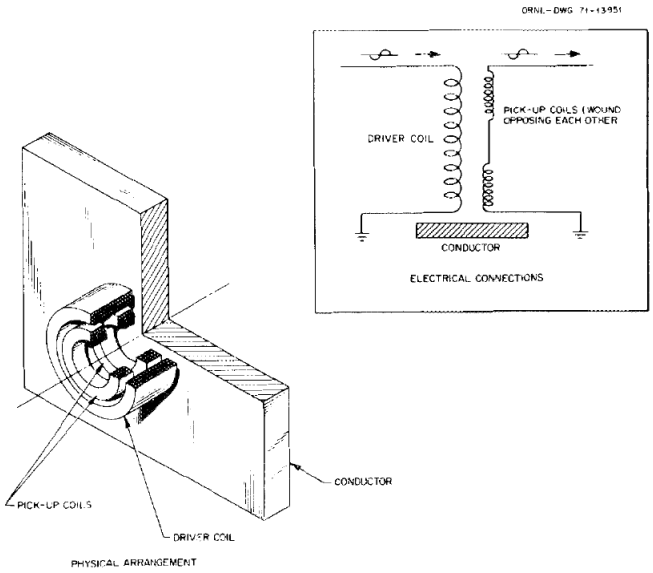

Figure 1.6: A reflection type probe in presence of a conductor [Dodd, C. V. (1973)]

apparatus is based on a Heydweiller bridge which measures the mutual inductance and mutual resistance of two toroidal windings on the annular specimen. They were able to calibrate the sensor with an accuracy of 0.4% with 10kHz exitation. [Lynch, A. C., Drake, A. E., & Dix, C. H. (1983) [26]].

- Detecting the structural integrity of aircraft parts due to rapid heating and cooling by utilizing the eddy current conductivity measurement techniques was investigated by G R Metcalfe in 1989. He concluded that conductivity measurements may be used as a basis for the assessment of integrity of an aluminium alloy following suspected or known heat damage [Metcalfe, G. R. (1990, January) [27]].
- In 1991, Hartwig and his team were able to study the effect of the primary coil dimensions on the eddy current resistivity measurement techniques. He showed that a slight variation in the coil dimension can drastically increase the sensitivity of the sensor by around 4-5% [Hartwig, K. T., Hua, C. Y., & McDonald, L. C. (1991) [28]]. The block diagram for the measurement scheme is shown in figure 1.7.
- In 1991, a non-contact measurement of the electrical resistivity providing a direct digital readout based on the magnetic susceptibility of

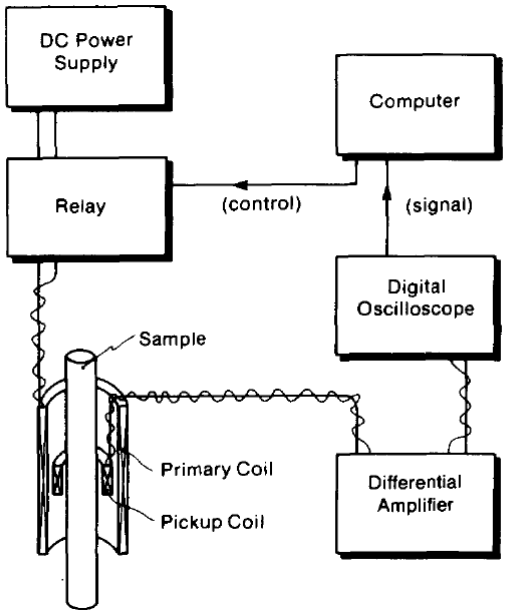

Figure 1.7: Block diagram of apparatus for measuring resistivity by the ECD method [Hartwig, K. T., Hua, C. Y., & McDonald, L. C. (1991)]

cylindrical samples in an axial AC magnetic field was developed by Kraftmakher, Y. A. (1991) [29].

- In 1992, a method that uses eddy current measurements to determine the conductivity and thickness of uniform conductive layers was demonstrated. They were able to test this method by estimating the conductivity and thickness of aluminum and copper layers on various substrate metals and also, the thickness and conductivity of free-standing foils of aluminum.[Moulder, J. C., Uzal, E., & Rose, J. H. (1992) [30]]
- In 1993, a numerical method for calculating the impedance of a cylindrical air-core probe over a layered metallic half-space was reported. This method was utilized to estimate the continuously varying conductivity and permeability of non-magnetic metals.[Uzal, E., & Rose, J. H. (1993) [31]]
- Defect size and shape estimation were carried out using careful measurement of impedance variations on the sensing coil. Non-idealities such as fringing effects of the coil were also tested and effects were studied.[Harrison, D. J., Jones, L. D., & Burke, S. K. (1996)[32]].

- A rapid and low cost method that is suitable for determining the thickness and conductivity of layers of non-magnetic metals on non-magnetic, conductive 4-8 substrates was demonstrated utilizing a pulsed eddy current technique. The pulsed eddy-current instrument records the transient current induced in an absolute, air-cored coil placed next to a layered sample and excited with a step-function change in voltage [Tai, C. C., Rose, J. H., & Moulder, J. C. (1996) [33]].
- Pioneering work on determining the electrical conductivity and resistivity of alloy $Cd_{1-x}Zn_xTe$ was done by H. N. Wadley in 1997. Conventional eddy current principles were utilized in a furnace to study how the alloy conductivity varied while it was melted and slowly cooled [Wadley, H. N., & Choi, B. W. (1997) [34]].
- In 2000, Y. Kraftmakher developed simple technique to demonstrate the effects of eddy currents for students. He was able to show the variation of the inductance of the coil and correlate it to different eddy current parameters like lift-off distances and coil dimensions [Kraftmakher, Y. (2000) [35]].
- Eddy current losses in monolith inductors and transformers were dealt in detail in 2001 by Ali M. N. A closed-form integral representation for the eddy-current losses over a conductive substrate was obtained for a MEMS spiral inductor [Niknejad, A. M., & Meyer, R. G. (2001) [36]].
- The apparent reduction of the near surface electrical conductivity measured by the eddy current method in the presence of surface roughness is studied in detail in 2002 by Peter B. Nagy et. al. Studies include conductivity measurements on pre-stressed and also fully relaxed shot peened copper specimen [Blodgett, M. P., Ukpabi, C. V., & Nagy, P. B. (2003) [37]].
- Advanced signal processing techniques like wavelet transform based multiresolution analysis was effectively used in non-destructive evaluation of the eddy current. The probe impedance data was used as the input to reconstruct the conductivity profile of metal targets [Shao, K. R., Guo, Y., & Lavers, J. D. (2004) [38]].
- A wide band eddy current in the range of 100Hz - 20Hz was utilized to

measure the electrical conductivity of metal sheets with an uncertanity of 3%. An improved model was developed utilizing the impedance variations of the coil along with the theoretical model to deduce the conductivity of the metal sheet (Brass and Stainless Steel)[Bowler, N., & Huang, Y. (2005) [39]].

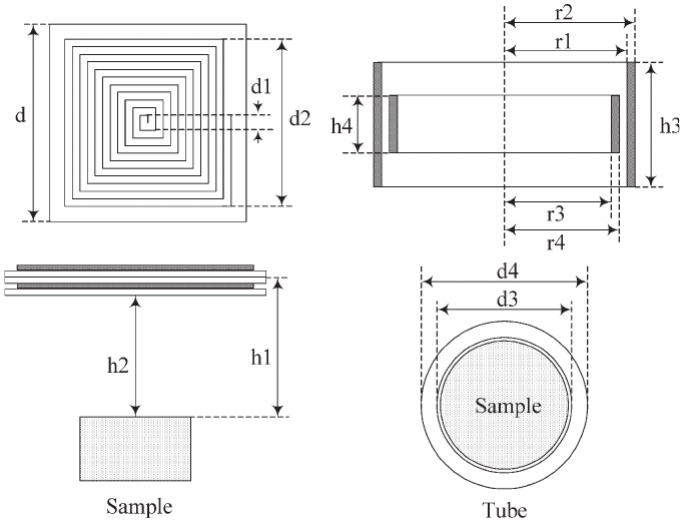

Figure 1.8: Coil sensors used in the applications. (Left) Planar pancake coils. (Right) Solenoidal sensor. [Ma, X., & Peyton, A. J. (2006)]

- Electrical properties of metal foams were characterized utilizing PCB based planar pancake type eddy current sensor. This work also presents a novel method of utilizing phase-frequency response of normalized eddy current sensor to obtain a lift-off insensitive measurement scheme. It also shows that eddy current methods can be utilized to measure the conductivity of porous material like a metal foam [Ma, X., & Peyton, A. J. (2006) [40]]. The sensor geometry that was used for the experiment is shown in figure 1.8.
- A modified interpretation of Dodd, C. V., & Deeds, W. E. (1968) is utilized to develop a more computation friendly model for an eddy current coil in the presence of a target. This model can be used to easily obtain the variable real and imaginary components along with the static real and imaginary components. These functions were solved analytically and the systems response to various parameter changes were

studied [Dziczkowski, L. (2007)] and [Dziczkowski, L., & Dziczkowska, M. (2007) [41, 42]].

– A review of different non-destructive techniques that are used widely in the metal industry to control the quality of materials was presented by García-Martín, J., Gómez-Gil, J., & Vázquez-Sánchez, E. (2011). This paper also includes an overview of the fundamentals and main variables of eddy current testing. It also describes the state of the art sensors and modern techniques such as multi-frequency and pulsed systems. Recent developments in advanced signal processing techniques and research in the area of non-destructive testing are also discussed in this work. [García-Martín, J., Gómez-Gil, J., & Vázquez-Sánchez, E. (2011) [43]].

It can be noted that very little or if at all any effort has gone into studying the utilization of an eddy current sensor for cryogenic applications. Insignificant amount of work has gone into the studies of non-contact conductivity measurement at cryogenic temperatures. This area is vital in development of sensors and sensing systems, especially in the fields related to super conducting radio frequency (SRF) cavities. These techniques are of utmost importance in fabricating and mapping the residual resistivity ratio (RRR) of the RF cavity. RRR of the Nb is the primary parameter that decides the performance of an RF cavity. Thus, a simple sensing system that is capable of working at temperatures below 10 K can go a long way in improving the performance of SRF cavities.

1.4.4 RRR measurement of Nb for superconducting RF cavities

The main component (building block) of a linear particle accelerator is a Superconducting Radio Frequency cavity (SRF). To develop a high performance SRF cavity, a high thermal conductivity of the cavity wall is required to guide the dissppated RF power to the surrounding coolant (liquid He). High purity is essential to avoid hotspots and eventual quenching of SRF

cavity. The most common indicator of the purity level is the residual resistivity ratio (RRR). A good high gradient cavity usually has RRR above 300. A detailed account of RRR will be provided in the next chapter.

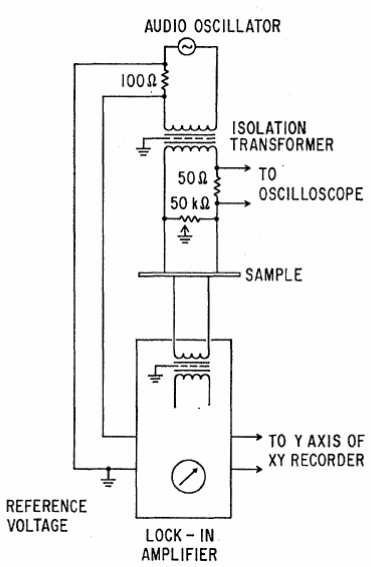

Figure 1.9: Sample resistance measuring circuit [Webb, G. W. (1969]

- The normal state resistivity of bulk Niobium (Nb) and its temperature dependence was first studied by G. W Webb in 1969. He carried out measurements at temperatures ranging from 9.25 K to 300 K with zero magnetic field applied and from temperature 2 K to 22 K with enough magnetic field to quench the superconductivity. An accurate temperature fit for the data was also derived from these experiments. The resistance data was obtained using the conventional four-probe resistance measurement with low frequency (17-230 Hz) sinusoidal current was used as the measurement technique to obtain the resistance data. [Webb, G. W. (1969) [44]]
- A significant amount of work went into modeling the behavior of the residual resistivity of polycrystalline superconductors. In 1990, Attansio et. al. were able to extend the model that considered a superconducting polycrystalline film as a network of superconducting grains coupled via Josephson junctions to include the RF and DC applied

fields and hence, was able to show the surface resistance of low temperature superconducting polycrystalline films [Attanasio, C., Maritato, L., & Vaglio, R. (1991) [45]]

– First attempts at RRR mapping of SRF cavities utilizing induced current based methods was initiated by Bolore M. et. al in 1991. Experiments were carried out using a pair of coils which were placed close to a Nb sample and low frequency currents in the range of 10 Hz to 1000 Hz were applied to the primary coil. This allowed them to obtain local measurements of RRR with a spatial resolution up to 1 cm. Their work correlated the ratio of induced voltage on the secondary coil to the primary coil voltage as a function of frequency and RRR. [Bolore, M., Bonin, B., Boudigou, Y., Heuveline, S., Jacques, E., Jaidane, S., ... & Safa, H. (1996) [46]]

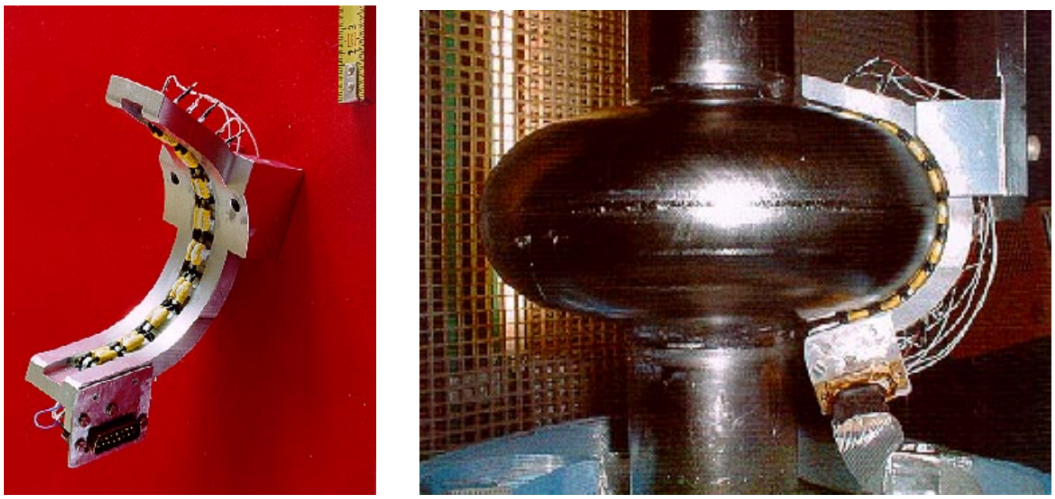

Figure 1.10: (a) Arm with sensor coils (b) Movable arm with the RF cavity [Singer, W., & Proch, D. (1996)]

– In 1996, another eddy current method was developed in DESY laboratory in Hamburg by a team lead by W. Singer. Here, a three coil system with a primary coil feeding the excitation current, a secondary pickup coil and the third compensation coil to cancel the effect of primary on the secondary coil was implemented to measure the RRR of the cavity. The mounting arrangement of the sensor along with the movable arm

is shown in figure 1.10. The jump in the peak induced voltage as the superconductor transitions from normal conducting state to superconducting state was correlated with the RRR of the RF cavity. [Singer, W., & Proch, D. (1996) [47]]

- A non-destructive RRR mapping of an SRF cavity was first achieved by a team from SACLAY laboratory under the leadership of H. Safa. They developed a movable arm consisting of a set of primary and secondary coil which can be used to measure the RRR as suggested by [46]. They were able to completely map fluctuations in RRR on the surface of the SRF cavity by monitoring the variations in the mutual inductances of the coils. [Safa, H., Boudigiu, Y., Jacques, E., Klein, J., Jaidane, S., & Bolore, M. (1997, October) [48]]
- Extensive studies on thin film coated SRF cavities were conducted to combine the advantages of copper RF cavities (High thermal conductivity) with that of SRF cavities (Better RF performance and Q). Some of their earlier efforts to characterize thin film coated SRF cavities started with a team in CERN, Geneva in 1999. [Benvenuti, C., Calatroni, S., Darriulat, P., Peck, M. A., Valente, A. M., & Van't Hof, C. A. (1999, November) [49]]. The same team published [Benvenuti, C., Calatroni, S., Hakovirta, M., Neupert, H., Prada, M., & Valente, A. M. (2001) [50]] in 2001 where their work was improved and further investigation were conducted to understand the sudden increase of residual resistance above 15 MV/m that was discovered earlier.
- By 2003, improved measurement techniques have been developed that could handle multiple samples of Nb at a time from the bulk and were tested by a team lead by Mosyes K. from the Fermilab, USA. The principle of measurement was still four wire resistance measurement scheme using low frequency current source and nano-voltmeter. They implemented dipstick based measurement so that multiple experiments could be carried out within a day compared to the time required with the cooling and heating process in a cryostat based system. [Moyses, K., & Bauer, P. (2003) [51]]
- The RRR measurement setup developed by Moyses, K., & Bauer, P.

(2003) [51] was used to study the effect of different processing steps on the RF cavity. The samples cut after the 1073 K heat treatment process to out-gas the Nb bulk and the samples cut after the E-Beam welding process to merge the two hemispheres of the RF cavity were all studied to determine the effect of different processing steps on the SRF cavity. [Bauer, P., Berenc, T., Boffo, C., Foley, M., Kuchnir, M., Tereshkin, Y., & Wokas, T. (2003, September) [52]]

- The acceptance test associated with Rutherford-type superconducting NbTi cables used in LHC accelerator, requires the testing of RRR of a large number of virgin strands of NbTi. The sample holder based on a fixed fiber glass window frame arrangement, is used to mount 20 samples at a time. The usual dipstick based measurement system along with the four wire resistance measurement at low frequency currents were used to determine the resistance value of each sample. [Russenschuck, S., & Vandoni, G. (2004) [53, 54]].
- A report detailing the fabrication process involved in an SRF cavity as done by Fermilab, USA is discussed by [Charifoulline, Z. (2006) [55]]. This report describes the importance of high RRR while fabricating an SRF cavity. It defines why the phenomenon such as phonon peaking can give an indication on the actual performance of the RF cavity. The relation between RRR and thermal conductivity at 4.2 K makes RRR an important parameter for purity measurement.
- Comparative study of performance of the niobium-coated copper resonators based on films generated by magnetron sputtering and by cathodic arc deposition in ultra high vacuum are discussed in detail by Russo, R. (2007) [56]. This work was done to study the limtations of conventional magnetron sputtering based RF resonators like the degradation of the q-factor with increasing cavity voltage ($\geq$ 30 MV/m).
- In 2010, Singer W. et. al. from DESY, Hamburg described the current techniques that were used by the accelerator community to measure the RRR of Nb. The review separates the measurement techniques into DC measurement and AC measurement. The significance of RRR measurement and the different definitions used by various research lab-

oratories around the world were discussed. It should be noted that AC methods are either based on the variations in the mutual inductance of the coils or on the jump in pick-up voltage when the transition occur from normal to superconducting state. This also included the results from different RRR measurement schemes and their relative accuracies associated with the measurement including the inductive measurement technique shown in figure **??** [Singer, W., Ermakov, A., & Singer, X. (2010) [57]].

– The thermal conductivity, DC magnetization and penetration depth of large-grain niobium hollow cylindrical rods, fabricated from ingots after subjecting them to chemical and heat treatment were measured. The results from the experiment confirmed that the impurity concentration of the original ingots were insignificant and the chemical and heat treatment processes influenced the superconducting properties [Dhakal, P., Ciovati, G., Kneisel, P., & Myneni, G. R. (2012) [58]].

1.5 Conclusions from literature survey

From the significant literature survey that has been presented in the previous section, some conclusions can be made as follows

1. Eddy current sensors have not been investigated in a significant way at cryogenic temperatures. The versatility of eddy current sensors like higher sensitivity, rugged design, local measurement etc., have not been explored to their fullest capacity for lower temperatures.
2. Very little work has been initiated in developing a complete eddy current transducer (sensing element + transduction electronics) that is capable of reliably working at temperatures down to 4.2 K.
3. There are no eddy current proximity sensors which have been shown to be capable of working at temperatures below 10 K. The lowest temperature that have been published in 20 K. There is demand for such sensors in cryo-vacuum conditions for space applications as well as for large superconductor facilities like CERN.

4. There are no through wall eddy current based angular displacement sensors that can work in cryo-vacuum environment. It has been reported that such sensors are required in deep space missions for robotic arms and rovers.
5. All the sensors that have been designed to operate at cryogenic temperatures as per the literature, had their signal processing element (variable conversion element) usually kept at room temperatures and not inside the cryostat (at cryogenic temperatures).
6. The non-contact, non-destructive characterization and RRR measurement for superconductors utilize calibration based measurement methods. This implies that no theoretical correlation exists between the measured parameters and the required variable. This may either be due to its complexity or due to their complete non-existence.

1.6 Objectives and outcomes

The main objective of this dissertation is to explore the possibility of using planar inductor eddy current sensors at cryogenic temperatures. In view of this, a set of applications have been chosen, that requires the use of specialized sensors operated at temperatures below 10 K.

1. A non-contact type eddy current based proximity sensor capable of operating at 4.2 K with high sensitivity and robust design is reported.
   - A detailed study of thermal effects on PCB based multilayer planar inductors and a novel experimental technique to measure the same are also presented.
   - Design, development and testing of a cryogenically operated unbuffered inverter based LC oscillator capable of converting the displacement changes to frequency changes is also presented.
2. A non-contact type through wall and robust eddy current based angular position sensor capable of operating in cryo-vacuum at temperatures down to 4.2 K, utilizing a planar multilayer inductor array and cryogenic switched inductor oscillator circuit is also presented.

3. A non-contact and non-destructive method for local measurement of Nb using planar inductor based measurement techniques has been developed. Three methodologies for RRR measurement using different measuring principles have been undertaken.
   - Implementing eddy current principles of impedance variations in an inductor in the presence of a non-magnetic conductor and extending it for cryogenic conditions ($\simeq$ 10 K to 290 K).
   - Using the inductance variation of the primary sensing element, in conjugation with a cold-electronics based oscillator circuit that can convert the inductance variations into frequency change. These frequency changes are used as a measure of the conductivity of the sample, which leads to RRR values.
   - Utilizing the correlation between the eddy current penetration depth with the variation in inductance of the sensor and using that to calibrate the sensor for RRR measurement.
4. These methodologies for RRR measurement are further extended to measure the electrical conductivity of non-magnetic conductors at cryogenic temperatures. Here, a novel technique for measuring the impedance changes in the sensing element using a cryogenic dual switched oscillator has been developed .

1.7 Organization of dissertation

This thesis is organized into chapters each dealing with a different eddy current sensor or a different set of sensors. The first chapter dictates the general introduction and literature review associated with the entire thesis. This section also includes the objectives and expected outcomes from the thesis. The second chapter details the design, development and testing of planar inductor based proximity sensor and its associated cold electronics that is capable of operating at 4.2 K. The third chapter details the process involved in developing an angular position sensor using cryogenically multiplexed LC oscillator circuit and inductor array sensing element. The fourth

chapter describes different methods for measuring RRR and electrical conductivity of Nb sample using planar inductor sensors. Here three different approaches are described in detail as well as the shortcomings of each one of them. The final section in the thesis discusses the results associated with each one of the chapters, the implications each of the developments and the future recommendations associated with this work. Finally the relevant references and appendices are provided at the very end of the thesis.

Chapter 2

Planar inductor based position sensor operating in cryogenic environment

2.1 Introduction

The proximity and position measurement is a critical requirement in many areas of low temperature physics, space applications, cryo engines and superconducting magnetic suspensions etc. [59–62]. In general, most of the position sensors are based on either potentiomenter or LVDT for low temperature applications[63, 64]. But the eddy current sensors operating on the principle of electromagnetic induction can precisely measure the position of a metallic target even in the presence of a non metallic barrier in between. Usually sensors operating at sub 20 K temperatures are based either on potentiomenter or LVDT principle even though eddy current based sensors have higher sensitivity and large frequency responses [8]. The main reason for this is that the electronics associated with the sensor fabricated using flat coils and operating at sub 20 K region has to be kept at stable room temperature [65]. It necessitates long connecting cables from room temperature electronics to the sensor at cryogenic temperatures. As the cable is subjected to different temperatures throughout its length, it introduces significant errors in the measurement. Hence, sensors of these types working at temperatures below 10 K are yet to be developed. An elaborate literature survey

on the topic is presented in chapter 1.

This chapter deals with the design, development and testing of a planar inductor based proximity/displacement sensor with integrated electronic circuit for Frequency Modulation (FM) of signal on a carrier wave. In the initial part of the thesis, the principle of operation of an eddy current proximity sensor was described. Once the principle has been established, the next step is to design the sensing element. Here, the optimization of the coil was performed using maxwell software. Thermal structural analysis of the multi-layered coil was done using ANSYS software and the structural warping was studied by cooling the sensor down to 4.2 K while measuring the change in the inter-layer capacitance. The next section deals with the design of cold electronics based LC oscillator. Selection of components were done through careful screening. Once the sensor was fabricated, the performance was tested for 4.2 K and the LC oscillator was characterized. After testing the electronics, the sensor was mounted along with the target at different lift-offs and the output frequencies were acquired using a custom program written in LabVIEW software. The sensor was then characterized and all its parameters were established using the experimental data.

2.2 Design and fabrication

2.2.1 Principle of operation

The mathematical modeling of the inductors in the presence of a metal target has been extensively studied in ref [23, 66]. Consider a coil having n turns concentrated into a radius r_0 at a height h above the conductor of thickness d which is greater than the skin depth at the operating frequency and the target conductivity is given by σ, as shown in Figure 2.1.
The change in impedance of the coil is given by,

$$\triangle Z = n^2 \omega \pi \mu_0 r_0 \phi(\alpha, \beta, \rho) \tag{2.1}$$

where,

$$\alpha = \frac{2h}{r_0} \tag{2.2}$$

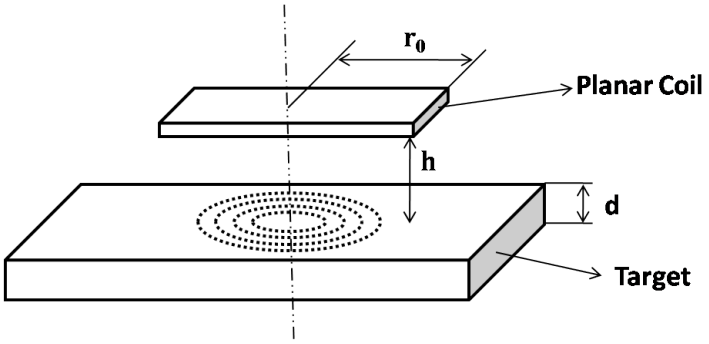

Figure 2.1: Principle of operation

$$\beta = r_0\sqrt{\omega\mu_0\sigma} \tag{2.3}$$

$$\rho = \frac{2d}{r_0} \tag{2.4}$$

are the generalized parameters and,

$$\phi(\alpha,\beta,\rho) = \int_0^\infty J_1^2(y)e^{(-\alpha y)}\frac{\beta^2(1-e^{-\rho\sqrt{y^2+i\beta^2}})}{\sqrt{(y^2+i\beta^2}-y)^2e^{-\rho\sqrt{y^2+i\beta^2}}-(\sqrt{(y^2+i\beta^2}+y)^2}d\alpha \tag{2.5}$$

here, J_1 is the first order Bessel function. The impedance term $\phi(\alpha,\beta,\rho)$ is a function of h as can be seen from the equations 2.1,2.2 and 2.5. Hence, $\triangle Z$ is a function of h when all other parameters are kept constant. This can be calibrated in terms of displacment (h).

2.2.2 Design of the multilayer planar inductor

The design of a multilayer planar inductor is presented in detail elsewhere [67]. The initial considerations for the prototype are the dimensions of the sensor. As the sensor has to be inserted in the sample chamber of the cryostat, the dimensions have to be limited. The other considerations were the operating frequency and the Q-factor of the coil. The operating frequency of the sensor is a function of the inductance of the coil. The Q-factor decides the sensitivity of the transducer. For a high enough Q-factor of above 10 and for a PCB based sensor, the inductance needs to be above 10 μH. Initial step was to design a single layer inductor.

Table 2.1: Inductor Parameters

Parameter	Value		Parameter	Value
D_{in}	4.114 mm		Conductor Spacing (s)	0.254 mm
D_{out}	26.97 mm		Turns (n)	23
Conductor Thickness (w)	0.254 mm		Fill factor (Θ)	0.7353

Using the inductor parameters given in Table 2.1, the inductance of a single layer can be calculated using the "Greenhouse formula" given by

$$L_1 = \frac{1.27\mu_0 n^2 d_{avg}}{2}[ln(\frac{2.07}{\Theta}) + 0.18\Theta + 0.13\Theta^2] \tag{2.6}$$

Where, Θ (fill factor) is given by,

$$\Theta = \frac{D_{out} - D_{in}}{D_{in} + D_{out}} \tag{2.7}$$

From the equations 2.6 and 2.7 and from Table 2.1, L_1 can be computed and it was 8018.9 nH. The inductance measurement at room temperature using an LCR meter at 1 kHz also gave the inductance value of 7800 nH, fairly agreeing with the calculation. The measured series resistance of this single layer was R_1 = 2.8 Ω

Using the dimensions given in Table 2.1, Ansoft Maxwell software was used to model a single layer coil. This was done to optimize the different coil parameters and to understand various parameter interactions. Simulations were carried out using magnetostatic analysis (solution type) to study the variation of each parameter on the inductance on the coil. Another set of experiments were carried out under the eddy current simulation method to understand the eddy current interaction on the target.

It can be seen from figure 2.2 (a) that the trace gap has a significant effect on the inductance, similar to the number of turns. Smaller gap between the traces give higher values of inductance for the coil, but fabrication becomes more and more difficult. The optimum when it comes to fabrication is 5 mil (0.254 mm) which corresponds to an inductance of around 7.5μH that is also in agreement with the calculated and measured values of inductances for a single layer coil. It was found that the trace thickness variation has no significant effect on the sensor. The coil

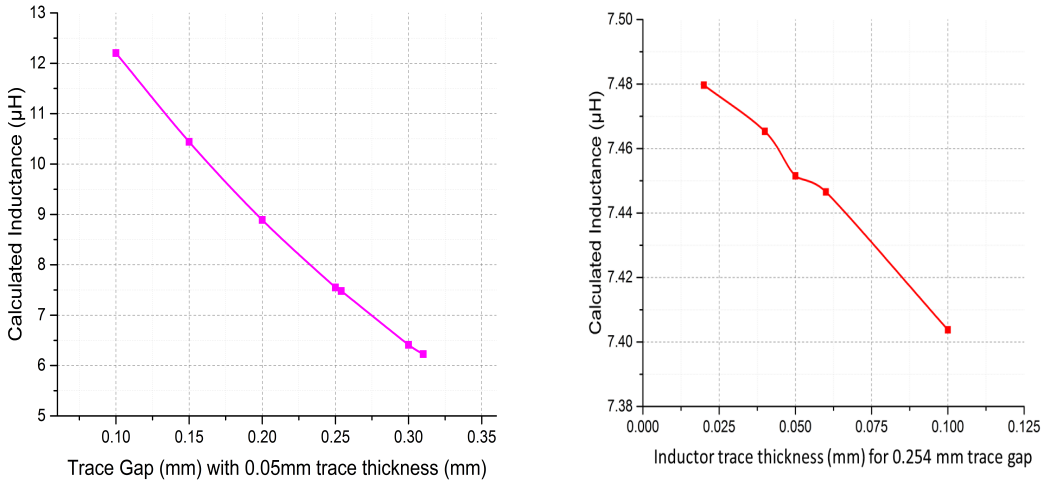

(a) (b)

Figure 2.2: Simulation results from Ansoft Maxwell showing (a) The variation of inductance with trace gap keeping all other parameters constant (b) Variation of inductance with trace thickness keeping all other parameters constant

inductance only reduces marginally with increase in the trace thickness as shown in figure 2.2 (b). This is of importance because, the trace thickness decides the series resistance as well as the Q-factor of the coil. The break in the curve in figure 2.2 (b) is attributed to a run-time memory overflow error that occurred during the execution of the program. A larger thickness would result in lower resistance and hence an overall improvement of Q-factor for the coil.

Once the optimum parameters were fixed, eddy current simulations were done to study the effect of a target near the coil. Figures 2.3 (a) and (b) shows the difference in the current densities on the surface of the copper target. It can be seen that the current densities rapidly reduce as the distance between the sensor and the target increases which is also shown in the equation 2.1. Hence the inductance associated with the coil also reduces as the target is brought closer to the sensor which is shown in figure 2.3 (d).

To further improve the Q-factor and series inductance of the sensor, a three layer sensing coil was chosen for fabrication. It had already been reported in [67] that the series arrangement of coil in specific orientation would result in inductance value higher than just the sum of the three layers. Table 2.2 shows the modified

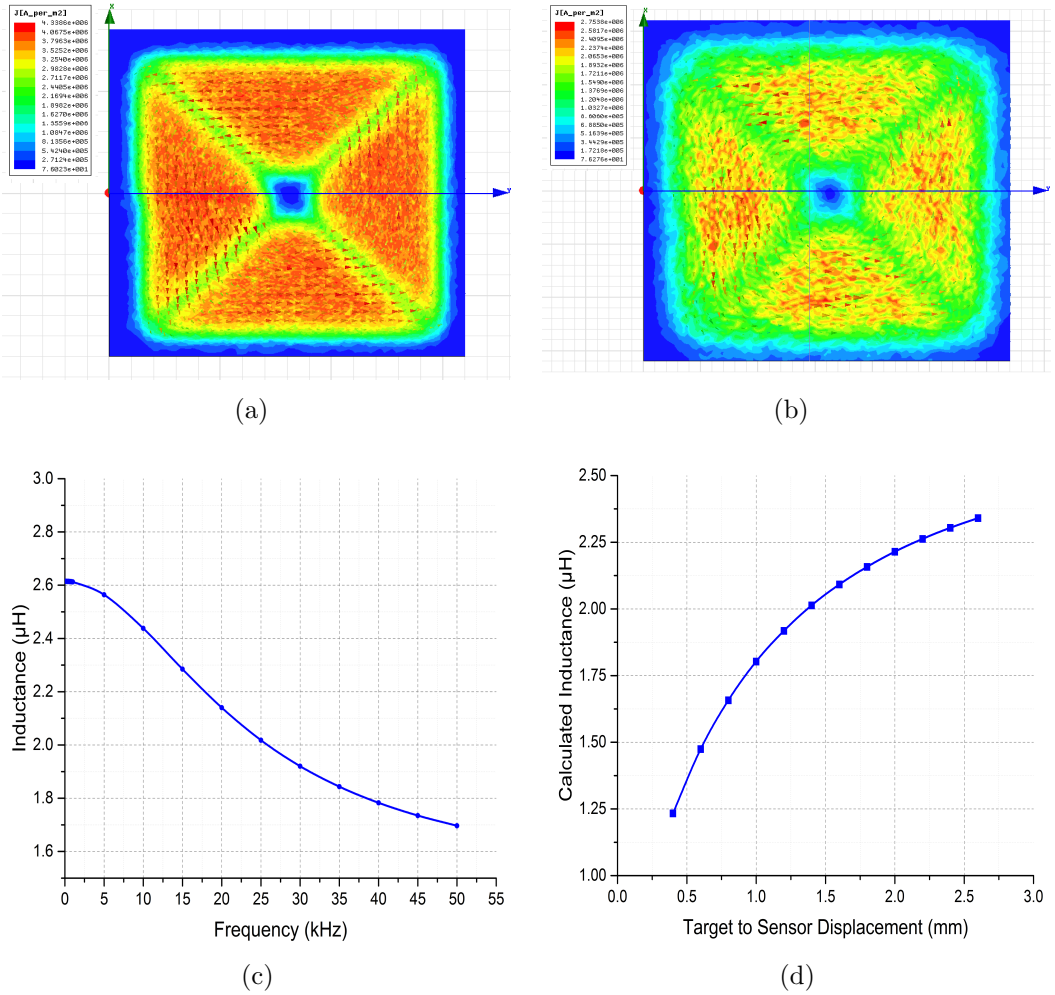

Figure 2.3: Eddy current simulation showing (a) The current intensity (J) on the surface of the copper target at 1 mm separation (b) The current intensity on the surface of the copper target at 2 mm separation (c) Variation of inductance with excitation frequency with a lead target (d) Variation of inductance when sensor to target displacement was changed (copper target)

parameters for a three layer coil along with the measured value of inductance. Here, R_1 is the series resistance of single layer; K_1 and K_2 are coupling coefficients. For a multilayer inductor, magnetic coupling exists between different layers of the coils. Hence, the total inductance will be more than an arithmetic sum of the individual inductance values of three layers.

Once the three layer sensor was designed, analysis had to be done to study the effect of temperature on the sensor. As the sensor is very sensitive to lift-off

Table 2.2: Modified parameters for 3 layer inductor

Parameter	Equation	Experimental values
L_{total}	$L_1[3+4K_1+2K_2]$	59.8μH
R_s	$3R_1$	8.4Ω

distances, lower temperatures should not warp the sensor and modify the lift-off. Simulations were done using ANSYS static thermal structural analysis. Here, the sensor dimensions were kept exactly same as that of the fabricated sensor.

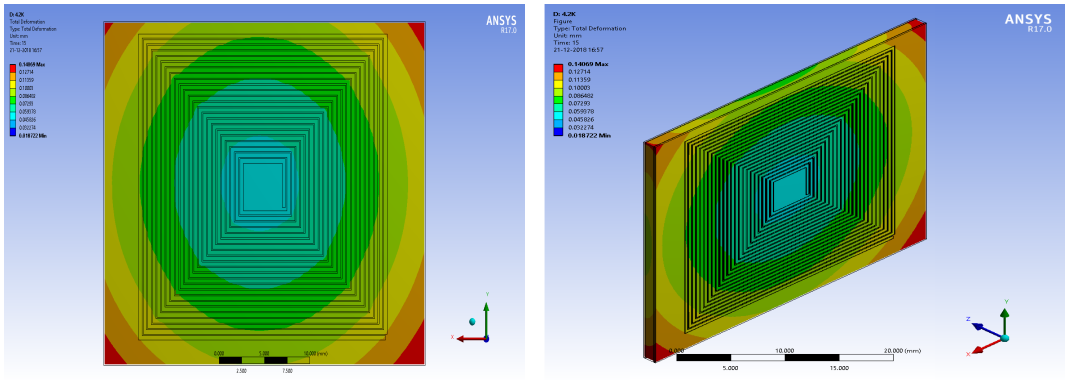

(a) (b)

Figure 2.4: (a) Top view of the deformed sensor cooled down to 4.2 K without any support (total deformation) (b) Isometric view of the deformed senor (total deformation)

From figure 2.4, it can be seen that a three layer PCB based sensor has some warping effects when the sensor is cooled and no rigid supports are provided. It should be noted that the maximum total deformation (sum of squares of deformation on all three directions) occurs on the edges of the sensor which do not have the coil. The average total deformation for the coils is 97.5μm at 4.2 K as shown in figure 2.5 (a). This warping will be reduced when there is a rigid support on the sides along with added structural support provided by the components. There are also many through hole component pads that are provided with copper trace and solder for providing the series connection that adds additional support to the structure.

To physically understand the deformation of the inductor, the interlayer capacitance was measured (layer 1 and 2). This method was chosen because it can be

easily measured by using a capacitance bridge and the sensor can be cooled down to 4.2 K. The change in the capacitance would give an indication of the extent to which it was warped with temperature.

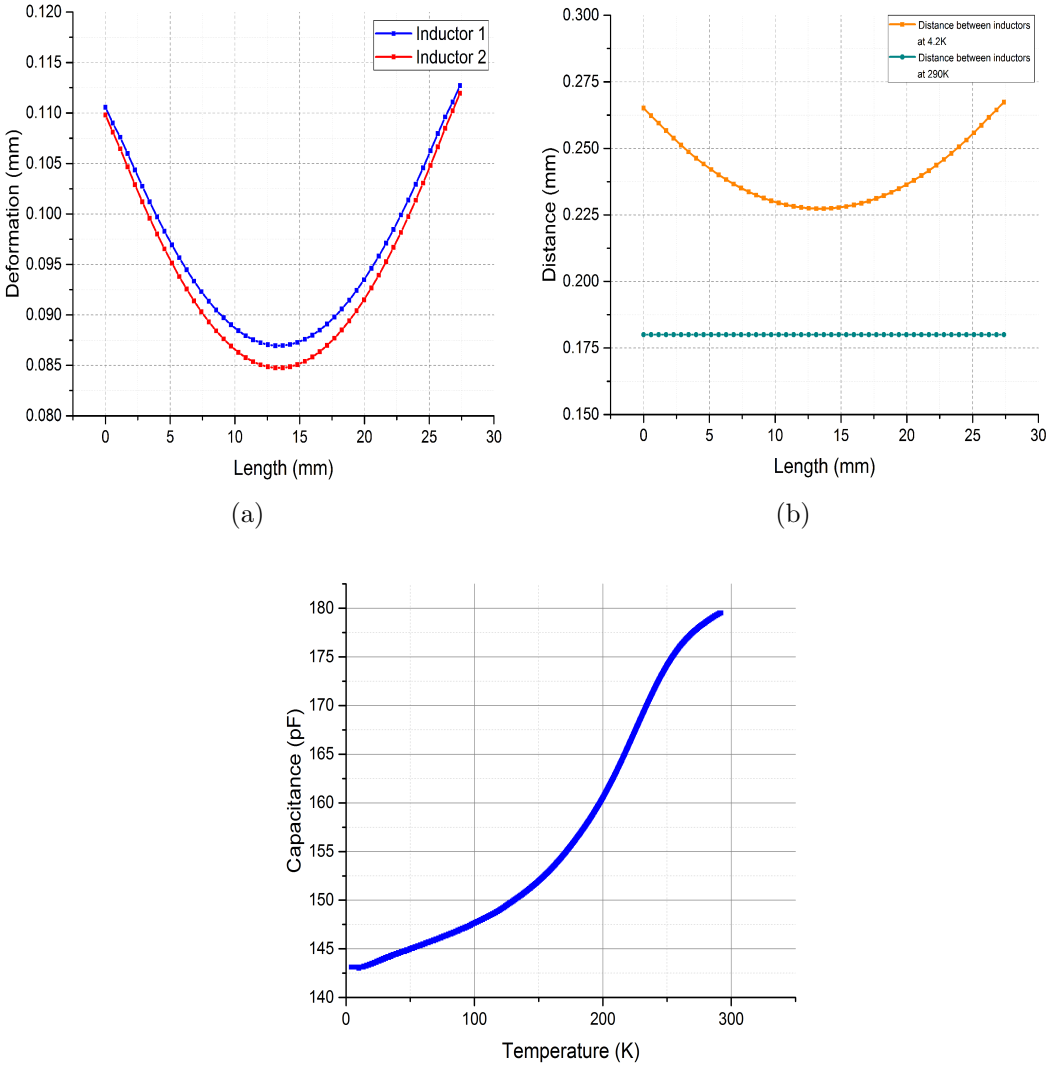

Figure 2.5: (a) Deformation along Z-axis for a diagonal element for layers 1 and 2 (b) Effective deformation of the capacitor along Z axis showing increase in distance between the plates (c) Experimental results showing capacitance variation with temperature

It can be seen from figure 2.5, that the effective z direction deformation increases the distance between the layers resulting in a decrease in capacitance as was

observed from experimental results shown in figure 2.5 (c). Another conclusion from simulation and experiments are that the deformation alone could not account for the magnitude of change in capacitance that was measured by experiments. This would mean that the assumption of keeping the permitivity a constant may not be valid and it may be a function of temperature. Experimental data is not available on the variation of electrical permitivity with temperature (cryogenic conditions) for FR4 material.

Once the structural analysis was done, the impedance analysis of the 3 layer inductor was done using E4990A Impedance Analyzer to determine its electrical characteristics and the results are shown in figure 2.6.

The inductance of the multilayer coil at the operating frequency of 150 kHz is 59.8 μH and the resistance is 15 Ω as can be seen from Figure 2.6 (a) and (b). The Self Resonant Frequency (SRF) of the coils were also determined using the impedance analyzer. The SRF of the 3 layer inductor was found to be 4.078 MHz. The Q of the at operating frequency (150 kHz) is around 4 as can be seen from Figure 2.6 (c). This Q-factor is sufficiently high enough to provide good sensitivity for the sensor.

Fabrication of a 3 layer inductor was taken up as per standard FRP PCB fabrication process. The inductor alignment and current directions in coils were designed to give additive mutual inductance to the overall inductance value as discussed by Islam et al., [67]. The sensor and its associated electronics are shown in Figure 2.7.

2.2.3 Design of cryogenic LC oscillator

A low cost digital inverter based LC oscillator circuit incorporating sensing inductor coils is shown in Figure 2.8. A major challenge in the design of electronics for the sensor at 4.2 K is the component selection. Most of the commercially available ICs fail at cryogenic temperatures. Detailed study of performance of individual components needs to be carried out in order to get the required performance and temperature stability of frequency.

Selection of components was a tedious process. Active components were chosen using the thumb rule that the internal circuit should comprise only of MOSFETs. There should also be no inherent MOS capacitors or resistors integrated into the

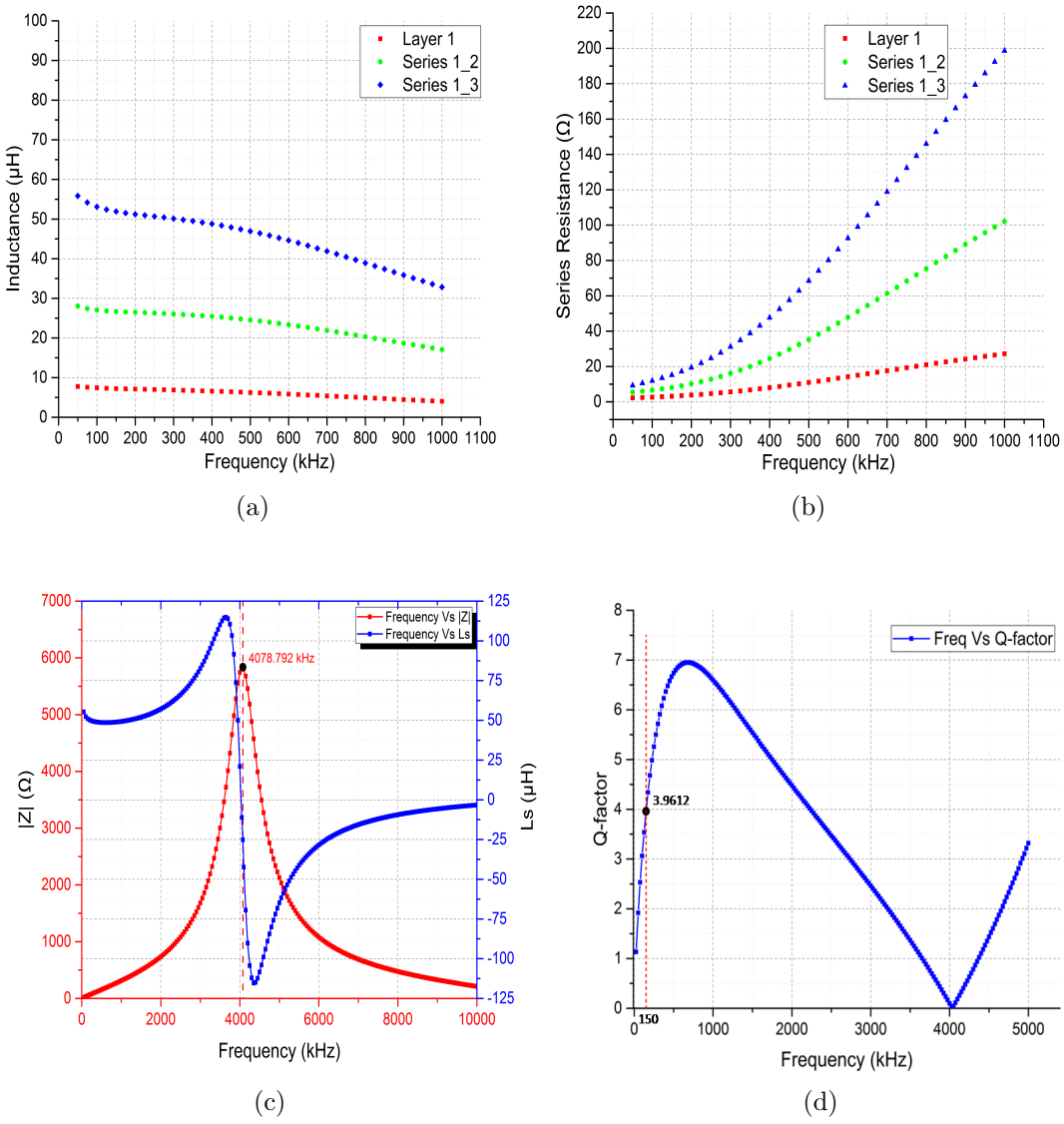

Figure 2.6: Frequency response showing (a) Series inductance variation for 1, 1-2 and 1-2-3 layer inductor(b) Series resistance variation for 1, 1-2 and 1-2-3 layer inductor (c) Modulus of Impedance and series inductance (3 layers) with SRF at 4078.8 kHz (d) Q-factor for the 3 layer sensor coil

circuit. Based on these general criterion, a set of components were short-listed and tested under cryogenic conditions. Selection of passive components were even more difficult as different literatures have shown some components to work, that have been shown in other experiments to be unsuitable for the cryogenic temperature

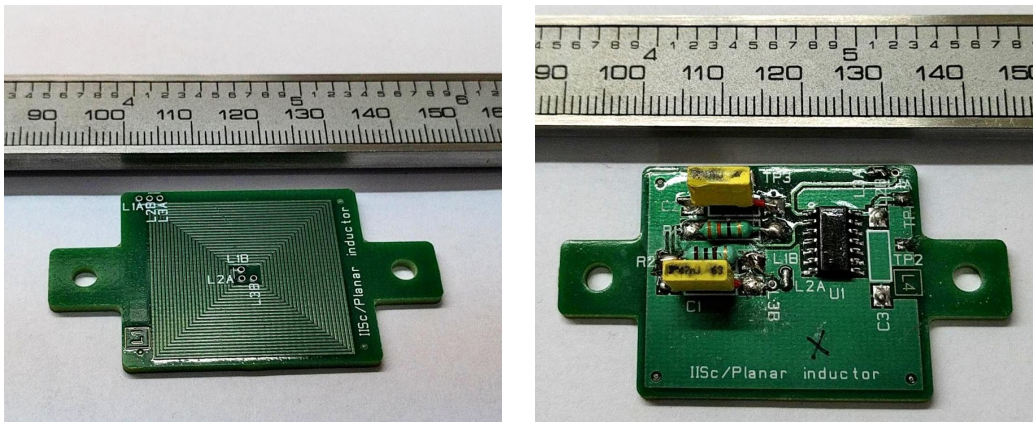

(a) (b)

Figure 2.7: Sensor showing a) top face sensing inductor b) bottom face electronics

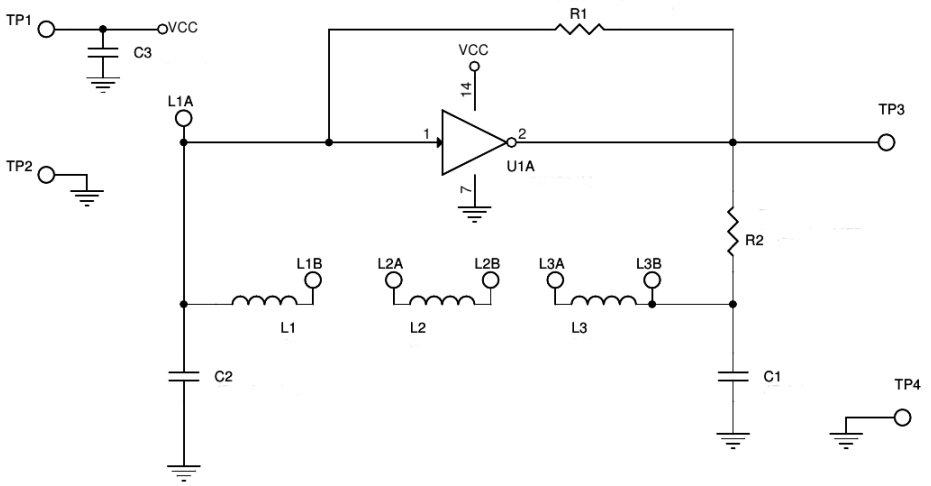

Figure 2.8: Digital inverter based LC Oscillator Circuit

range. To circumvent this issue, several commonly available passive components were purchased and cooled to 77 K and their characteristics were studied as shown in figure 2.9.

It can be seen from figure 2.9 that the best suited capacitor for cryogenic application is the SMD type, NP0 (ceramic) capacitors which has almost negligible temperature effect when they were cooled down to 77 K. Similarly, the most suited resistor was found to be Metal Film Type (MFR) leaded resistors. Based on these experiments, the list of components used in the final circuit and their temperature coefficients and tolerances are listed in Table 2.3. Here thermal cycling implies 10 minutes soak in LN_2 followed by 5 minutes thaw at room temperature. Soak

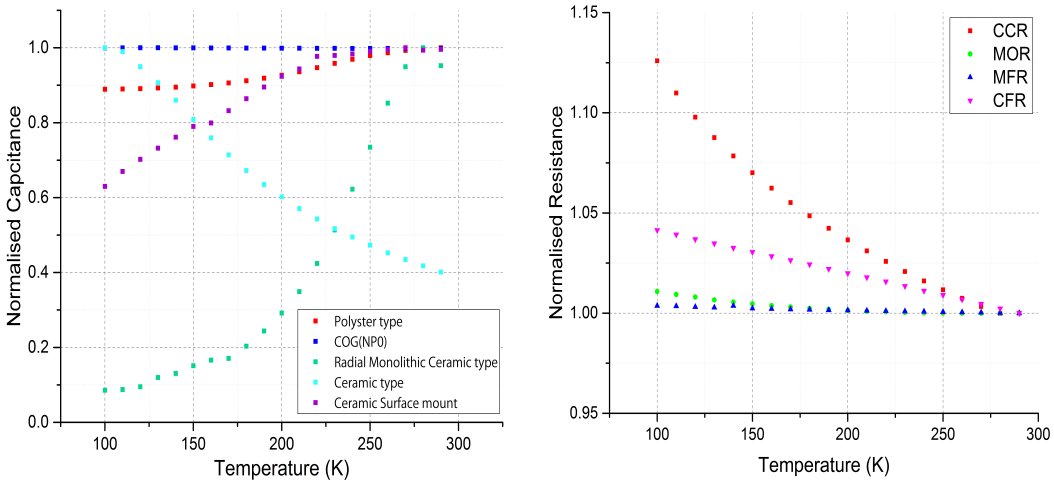

(a) (b)

Figure 2.9: Testing for passive components for cryogenic applications (a) Normalized capacitance values for several types of capacitors (b) Normalized resistance values for several types of resistors

tests are conducted to study the structural integrity of each of the components. The Cold start experiments are usually carried out for active components like Op-Amps. Here the same test was conducted on inverter IC to check if any carrier freeze-out was occurring at 4.2 K.

Table 2.3: List of components, test parameters and results

Components	**Features**	**Tests**
Inverter	CMOS LSTTL hex inverter	Thermal Cycling (30 times), Cold Start at 4.2 K
Capacitors	1% tolerance, ±30 ppm/K	Thermal Cycling (30 times)
Resistors	0.1% tolerance, ±5 ppm/K	Thermal Cycling (30 times)

Once the components were chosen, the operating frequency had to be decided. The thumb rule used in the selection of the operating frequency is,

$$f_{operating} \leq \frac{SRF}{10} \tag{2.8}$$

This $f_{operating}$ was chosen so that the inductance would be very stable even when the frequency of the oscillator changes due to change in the measured parameter. If the sensor is operated close to SRF, due to the effect of parasitic capacitance, the L_s would vary rapidly with change in the oscillator frequency (insted of other

way around), and would spiral into an unstable condition. The penetration depth (δ) at the operating frequency is given by,

$$\delta = \sqrt{\frac{1}{\pi \mu \sigma f}} \tag{2.9}$$

where, μ is the permeability and σ is the conductivity of the material. The penetration depth should be much less than the thickness of the material. The first condition (equation 2.9) allows for stable oscillations even when the inductances change between its minimum and maximum values and the second condition allows the sensor to be depended only on the displacement and conductivity of the material above the sensor. This also eliminates the cable and interconnecting inductance effect to a minimum. From figure 2.6, the SRF of the 3 layer inductor can be found to be 3.71 MHz. Hence, the operating frequency should be less than 371 kHz and it was chosen to be 150 kHz. Also, at the current frequency of operation, for a copper target, the skin depth is less than 0.2 mm. Hence, the target with 1 mm or above thickness was chosen for the experiment. The frequency of oscillation for an LC oscillator is given by,

$$f_{operating} = \frac{1}{2\pi\sqrt{L_{total}C}} \tag{2.10}$$

the corresponding value for C was desired and used in the circuit.

2.2.4 Performance analysis of the designed oscillator at various temperatures

The effect of low temperature on the circuit characteristics were analyzed by subjecting the sensor to temperatures from 300 K to 4.2 K. The temperature response of the circuit at 4 different temperatures are shown in Figure 2.10.
The harmonic noise level in the oscillator increases as the temperature decreases. These are the oscillations that occur at both the top and bottom stable voltages for a digital oscillator as shown in the figures 2.10. The temperature dependence of this harmonics is shown in Figure 2.11(a).
Even though there is an increase in the harmonics at lower temperatures, since the sensor output depends only on the basic frequency information, these peak noise

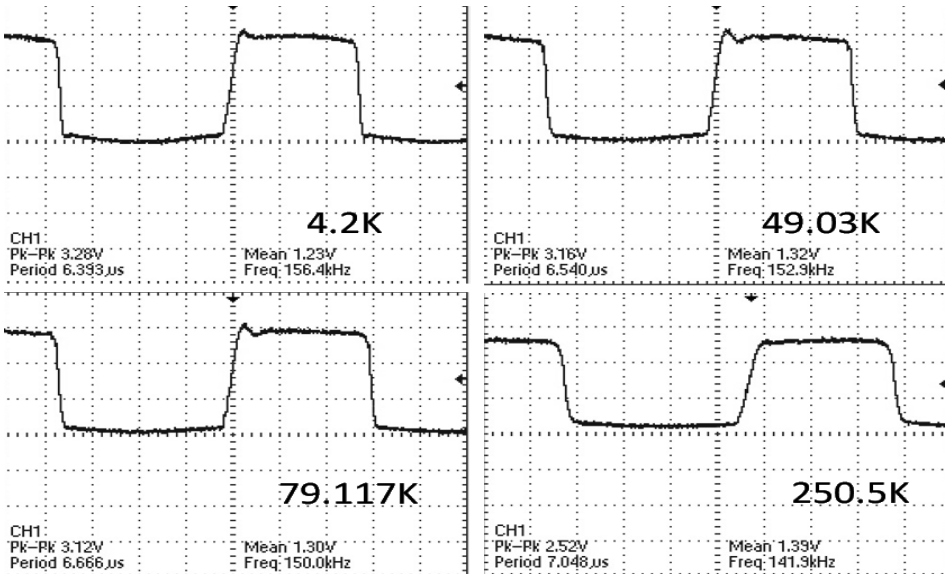

Figure 2.10: LC Oscillator output at various temperatures

harmonics do not have any effect on the performance. But they are interesting to analyze as the components that are selected have very stable, negligible temperature dependence. The only component that is introducing these harmonics is the CMOS inverter IC itself. The effects can be mitigated to certain extent by adjusting the feedback resistor.The frequency dependence on temperature for the sensor can be attributed to the varying internal parameters of the CMOS active components in the inverter IC. This in turn changes the output and input impedance of the logic IC and results in harmonics in the output waveforms. The sensor output as a function of temperatures is shown in Figure 2.11(b). The circuit seems to exhibit higher nonlinear response as the temperature is reduced below 30 K. This distortion in response can be reduced by adjusting the supply voltage for the circuit. The average coefficient of temperature dependence was found to be 55.317 Hz/K .

The trends for the rise and fall times of the oscillator circuit are shown in figure 2.12 (a). It can be seen that there is a trend for reduction in the rise and fall times of the circuits with decreasing temperature. It is also interesting to note that both rise and fall time have almost the same slope. The slope for rise time trend line is 0.323 ns/K were as that for the fall time is 0.338 ns/K. This reduction in the rise and fall times may be associated with the increase in electrical parameters of the IC with decrease in temperature and the change in the internal capacitances

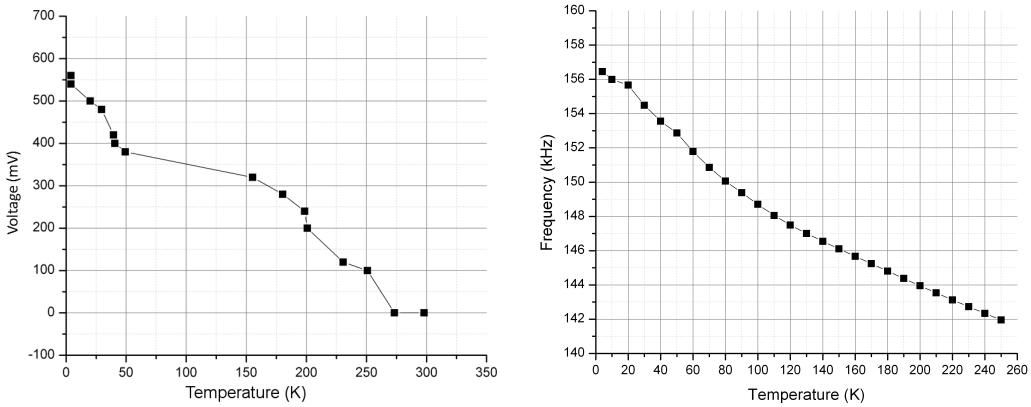

(a) (b)

Figure 2.11: Temperature effect on (a) peak to peak harmonics (b) oscillator frequency

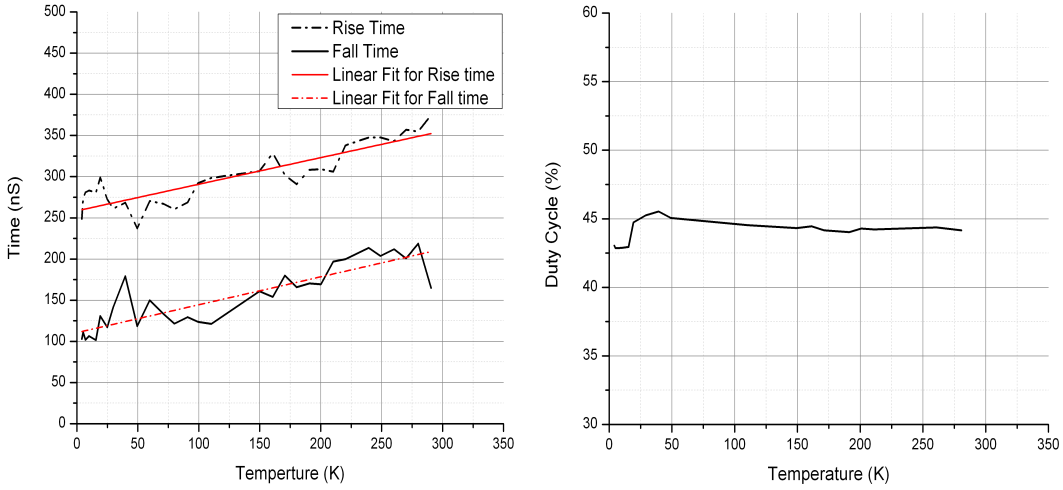

(a) (b)

Figure 2.12: Variation of (a) Rise time and fall time against temperature (b) Duty cycle plotted against temperature

of the MOS gates used in the inverter IC.

Duty cycle has almost a flat profile for the entire range of temperature as can be seen from figure 2.12 (b). It was found that there was a sudden change in the duty cycle when temperature goes below 25 K. But overall, the duty cycle stays within 3% of it's the value in the temperature range of 300 K to 4.2 K.

2.3 Experimental setup and DAQ

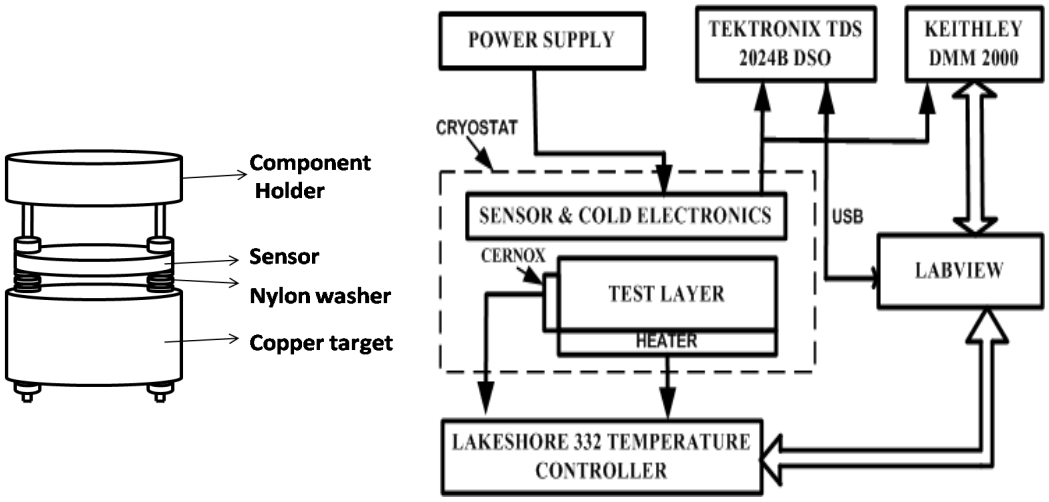

(a) (b)

Figure 2.13: Schematic of a) mounting of the sensor on the dipstick b) DAQ system

A commercially available cryostat from Janis is used for this experiment. The description of the cryostat is available elsewhere [68]. In the current experiment, the sensor is mounted at the tip of the dipstick along with a target copper sample at a specified distance from the sensor using nylon washers on the sample rod as shown in Figure 2.13(a). The target used for the experiment was an electrolytic grade copper sample of 35 mm×30 mm×6 mm dimensions. 6 mm thickness was chosen such that the penetration depth $\delta <<$ thickness. The distance between the copper sample and the sensor is changed in subsequent experiment by changing the number of nylon washers between the sensor and the sample, thus a 1 mm resolution on the displacement was possible using this arrangement.

The output signal that is obtained from the sensor is fed to a Keithley 2000 DMM and a Tektronix TDS 2024B Digital Storage Oscilloscope (DSO). The signal is acquired and logged using LabVIEW software through GPIB interface. Phase information and signal quality including noise parameters were captured using a DSO and logged using LabVIEW software through USB interface. Accurate temperature information was obtained by using a pre-calibrated Cernox sensor with a Keithley 332 temperature controller. Stable temperature was obtained and controlled through a PID controller with the help of temperature data and heater

coil. The schematic for DAQ is shown in Figure 2.13(b)

2.4 Experimental results and discussions

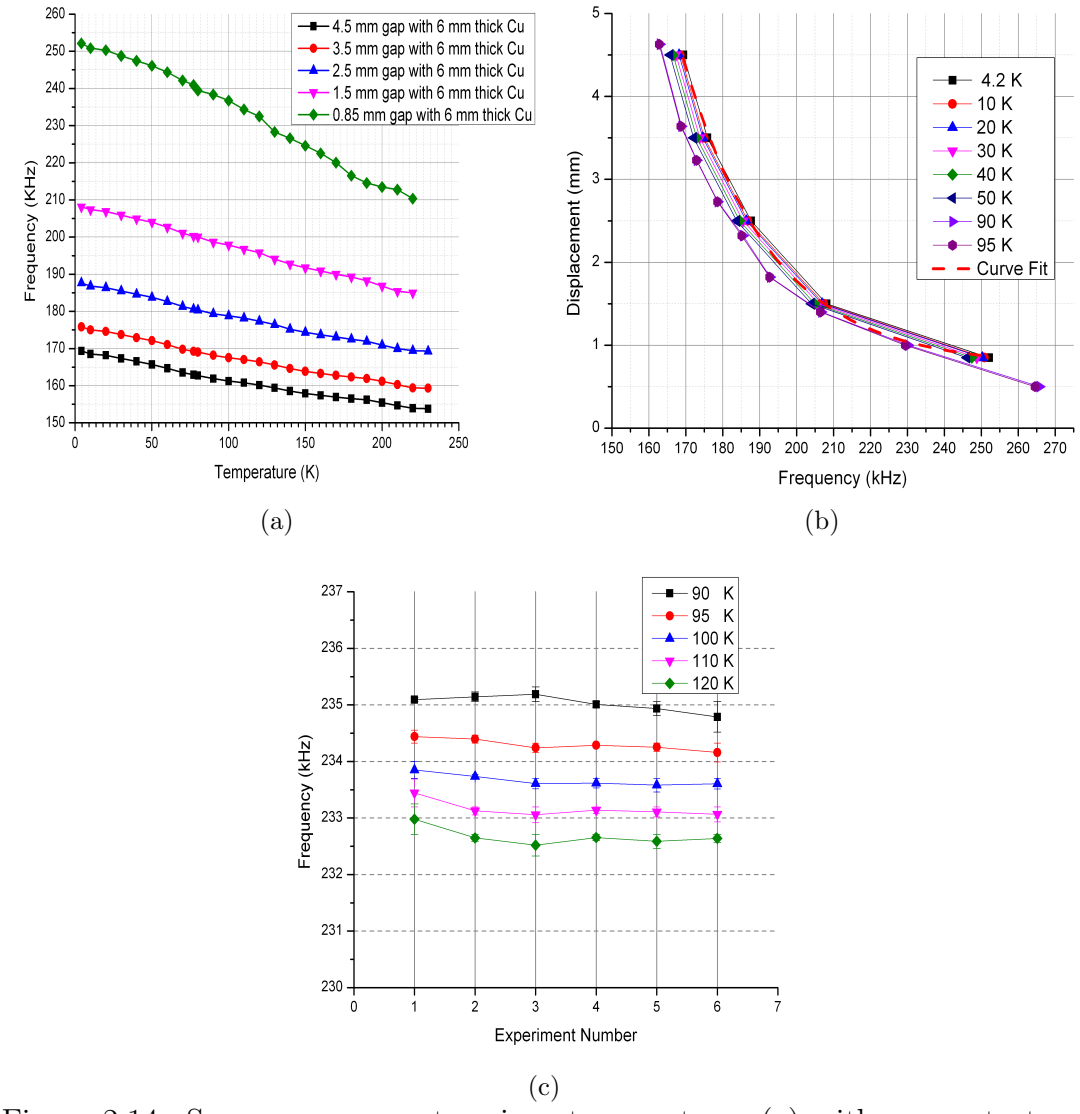

Figure 2.14: Sensor response at various temperatures (a) with sensor to target displacement varied (b) at various displacement and an asymptotic curve fit for 4.2 K (c) Repeatability of the sensor with error bars at 5 different temperature

Sensor to target distance was changed from 0.85 mm to 4.5 mm and the sensor was cooled to 4.2 K from room temperature and the frequency outputs were recorded. A plot of variation of frequency for each separation when the sensor was cooled

to 4.2 K was also recorded. A piece wise linearized sensitivity of the sensor at different ranges are calculated and are shown in Table 4. From the repeatability measurements a statistical analysis of the data was done to determine the sensor accuracy which shown in Table 4. Resolution of the sensor in different ranges for 5% accuracy was calculated and is given in Table 4.
Repeatability of the sensor was determined by keeping the sensor to target distance constant, cooling down to 90 K and repeating the experiments 6 times. A plot of sensor output at 5 different temperatures along with the error for each measurement is shown in Figure 2.14(c). A statistical data analysis was done using the repeatability data to determine the accuracy of the sensor in each of the linearized region.

Table 2.4: Sensor Parameters

Sl. No	**Linearity Range**	**Average Sensitivity**	**Accuracy**	**Resolution**
1	0.85 mm - 1.5 mm	14.77 μm/kHz	$\pm$ 1.84 μm	40μm
2	1.5 mm - 2.5 mm	48.91 μm/kHz	$\pm$ 7.6 μm	150μm
3	2.5 mm - 3.5 mm	84.52 μm/kHz	$\pm$ 33.6 μm	670μm

Figure 2.14(a) shows the frequency response curves of the sensor when it is cooled from room temperature to 4.2 K at different separations. It can be seen that as the sensor gets closer and closer to target, the sensitivity increases exponentially. In fact, the sensitivity of the sensor follows an asymptotic curve given by the expression,

$$y = a + b.c^x \tag{2.11}$$

were the values of a,b and c are 0.75, 4521.7 and 0.96 respectively as shown in Figure 2.14(b).

2.5 Conclusion

A multilayer planar inductor based eddy current proximity/displacement transducer for measurement of displacement of a metallic surface was successfully designed and tested to work satisfactorily at 4.2 K. The sensor was designed considering the thermal structural analysis as well as Maxwell Ansoft eddy current simulations. The sensor was found to exhibit warping, but was found

to be within the designed margin of error. The deformation was confirmed by observing the inter-layer capacitance of the multi-layered sensor.

A cold electronics based LC oscillator circuit which converts the inductance change of the sensing element into a frequency change was also designed and tested. Careful selection of components was done by cooling and testing a large number of components down to 77 K and selecting the ones that showed the minimum deviation. Active components were also tested down to 4.2 K . Once the sensor was fabricated, The cold electronics was characterized by cooling the circuit down to 4.2 K and by studying the changes associated with the output waveforms. The designed multilayer planar inductor was analyzed using E4990A impedance analyzer and its parameters were compared with the theoretical values. The noise performance of the transducer at cryogenic temperatures was also studied. A piecewise sensitivity, accuracy, average temperature coefficient and resolution for the sensor were determined and tabulated.

Chapter 3

Design, development and testing of cryogenic angular displacement sensor

3.1 Introduction

For many applications involving cryogenics, viz. low temperature physics, space applications etc., the measurements of accurate angular displacement are critical [14]. Usually, potentiometers, Hall Effect sensors and Fiber Brag grating based sensors are commonly used for such applications [6, 10, 11, 15]. Few of these have been shown to work at cryogenic temperatures [14, 69]. Carapelle et.al.[14] had shown that most common Angular Position Sensors (APS) working in cryogenic environment utilize large sets of coils and the closing of a magnetic reluctance path to accurately measure the position of the rotor. This also requires a series of half tori's to be embedded into a rotor mechanism which acts as a lower reluctance path between the excitation and the sensing coils. Kejik et.al [70] developed transducers which employ a ring of Hall Effect sensors and a rotor with permanent magnets . These sensors are not only expensive but also require carefully constructed rotor systems and sensing mechanisms to sense the angular position with the given amount of accuracy. These are also not shown to work at cryogenic temperatures. All these shortfalls are addressed in the present design; which employs a multilayer planar inductor array fabricated on an fiberglass reinforced epoxy laminates (FR4)

based printed circuit board (PCB), as the sensing element and a rotor with a simple etched copper sector. As the circuit to convert the impedance change to frequency change is also a part of the sensor, the errors associated with the large lead impedances are also eliminated. The entire sensor and electronics have been designed to operate at cryogenic temperatures down to 4.2 K.
The chapter consists of a) A description of the principle of operation, b) the design and development of a multilayer planar inductor array and the multiplexed inductor based LC oscillator which is used as the signal conditioning element of the sensor c) the design and development of rotor segment with zero dead zone d) the experimental setup consisting the instrumentation used to calibrate the developed sensor and finally the experimental results and conclusions.

3.2 Design and fabrication

3.2.1 Principle of operation

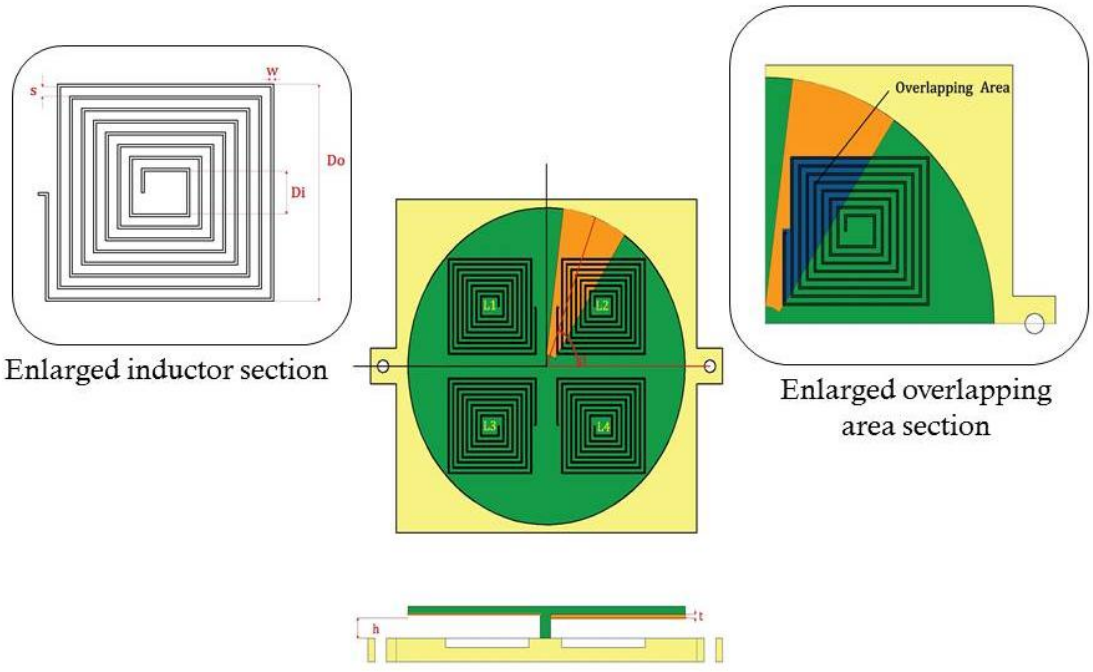

Figure 3.1: Pick-up coil schematic

Consider a coil having n turns concentrated into a radius r_0 at a height h above the conductor. A target whose thickness t which is greater than the skin depth at the operating frequency is kept below, as shown in figure 3.1. The mathematical model for this configuration can be extrapolated from the models given by [31, 40, 71, 72]. For a non-magnetic material, the target and the sensor coil can be regarded as a weakly coupled air-core transformer [73–75], as shown in figure 3.2. The primary of the transformer represents the sensing coil, which has a series resistor R_c and an inductance L_c. The target can be assumed to be the secondary of the transformer (shorted) with inductance L_t and resistance R_t.

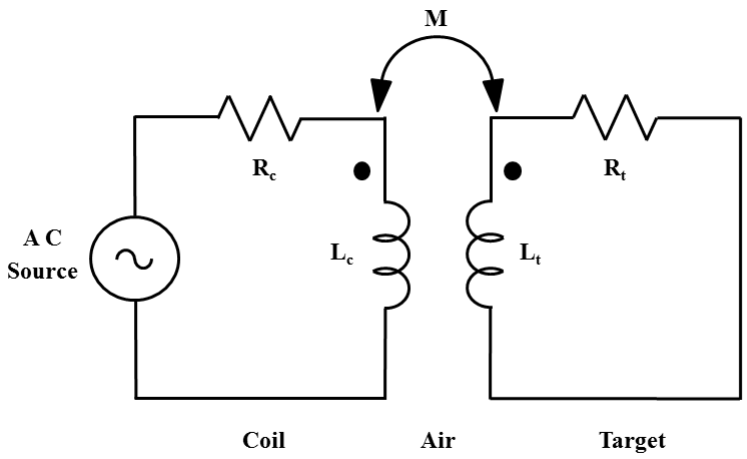

Figure 3.2: Transformer model for eddy current sensor

The change in impedance of the coil is given by,

$$L_c - L_t = L = L_c - \frac{\omega^2 M^2}{R_t^2 + (\omega L_t)^2} L_c \tag{3.1}$$

and

$$R_c + R_t = R = R_c + \frac{\omega^2 M^2}{R_t^2 + (\omega L_t)^2} R_c \tag{3.2}$$

where, $\omega = 2\pi$f and M is the mutual inductance between the two loops. It can be seen that the effective value of inductance in the presence of the conductor decreases and the effective value of the series resistance of the coil increases.
An Ansoft Maxwell simulation of a planar single layer inductor with a copper target (2 mm thickness and 2 mm sensor to target separation) using eddy current

physics settings was carried out. It can be seen from figure 3.3(a) that the current density is highest under the coil and it decreases rapidly away from the coil. Now, assuming that the area of the target linked with the coil is varied, keeping thickness and gap between the sensor and the target a constant as shown in figure. 3.1, it will result in a change in the impedance of the coil depending on the overlapping area. The overlapping area of the copper target was varied and the results of the simulation are shown in figure 3.3(b). It can be seen that, as the overlapping area increases, the inductance value will decrease as predicted by equation (3.1).

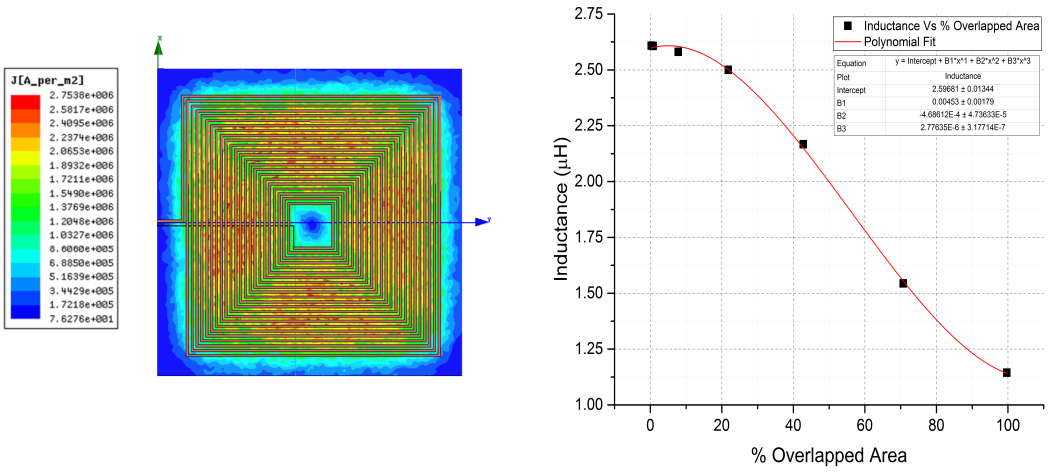

(a) (b)

Figure 3.3: FEM Simulation done using Ansoft Maxwell (a) A single layer planar inductor with a copper target excited at 10 kHz (b) Calculated inductance when overlap area was varied

When a rotor having a segment of small conductor is rotating in the vicinity of the coil, the area of the segment coupled to the magnetic field of the coil also varies. This results in change of the inductance of the coil as predicted by equation (3.1). When the inductor forms a part of the tank circuit of an unbuffered inverter based LC oscillator which is tuned to be sensitive only to the inductance L_c, the frequency change of the oscillator will be a function of the overlapping area; i.e. angular displacement. When angular position is a time varying function, the output would be a frequency modulated (FM) wave; wherein, the modulated wave corresponds to the angular position of the metal target with respect to the inductor (pickup coil).

3.2.2 Design of multilayer planar inductor

Typical values of a single layer planar inductor are listed in Table 3.1. It is needed to keep the dimensions of the coil as small as possible due to various considerations viz localized measurement, cryostat bore diameter etc. The frequency of operation calls for a sensor with inductance as large as possible to keep the frequency low.

Table 3.1: Inductor Parameters

Parameter	Value
D_{in}	2.29 mm
D_{out}	15.00 mm
Conductor Thickness (w)	0.25 mm
Conductor Spacing (s)	0.25 mm
Turns (n)	13
Fill factor (Θ)	0.7353

While the operating frequency is a function of the inductance of the coil, the Q-factor determines the sensitivity. For a value of 2 and above for Q-factor, the inductance needs to be $\geq 10\mu$H, for a specific minimum track size and trace gap. The inductance value can be computed using the values given in table with the help of "Greenhouse formula" given by equation (2.6).

$$L_1 = \frac{1.27\mu_0 n^2 d_{avg}}{2}[ln(\frac{2.07}{\Theta}) + 0.18\Theta + 0.13\Theta^2] \tag{3.3}$$

Here, Θ is called the fill factor given by,

$$\Theta = \frac{D_{in} - D_{out}}{D_{in} + D_{out}} \tag{3.4}$$

The computed value of L_1= 2135.3 nH agrees fairly with the measured value of 2100 nH measured using an LCR meter at room temperature and at 1 kHz excitation. Again this agrees with the Ansys Maxwell model for the same single layer inductor.

Table 3.2: Modified Equations for 5 layer inductor

Parameter	Equation	Experimenal values
L_{total}	$L_1[5+8K_1+6K_2+4K_3+2K_4]$	40.6 μH
R_s	$5R_1$	8.4 Ω

The inductance value of a five layer planar inductor is given in Table 3.2 and the modified equations is given in the same. From Table 3.2, it can be deduced that the total inductance of five layers connected in series is not an arithmetic sum of the individual values but due to magnetic coupling, the coefficients K_1, K_2, K_3 and K_4 increase the total inductance (effectively equivalent to more than twenty layers). Using an impedance analyzer, the coupling coefficients can be calculated. The detailed analysis of design of a multilayer planar inductor for eddy current sensor is given by A. B Islam et. al and P. Sagar et. al [1, 67].
Fabrication of five layer inductor was done as per standard FRP PCB process. The inductor alignment and current direction in the coils were designed to give maximum additive mutual inductance value in line with A. B. Islam et.al [59]. The photographs of the pickup coil and the associated electronics are shown in figures. 3.4 (a) & (b). The sensor PCB has 5 layers of inductors connected in series and the bottom face has the cold electronic circuits incorporated into it.

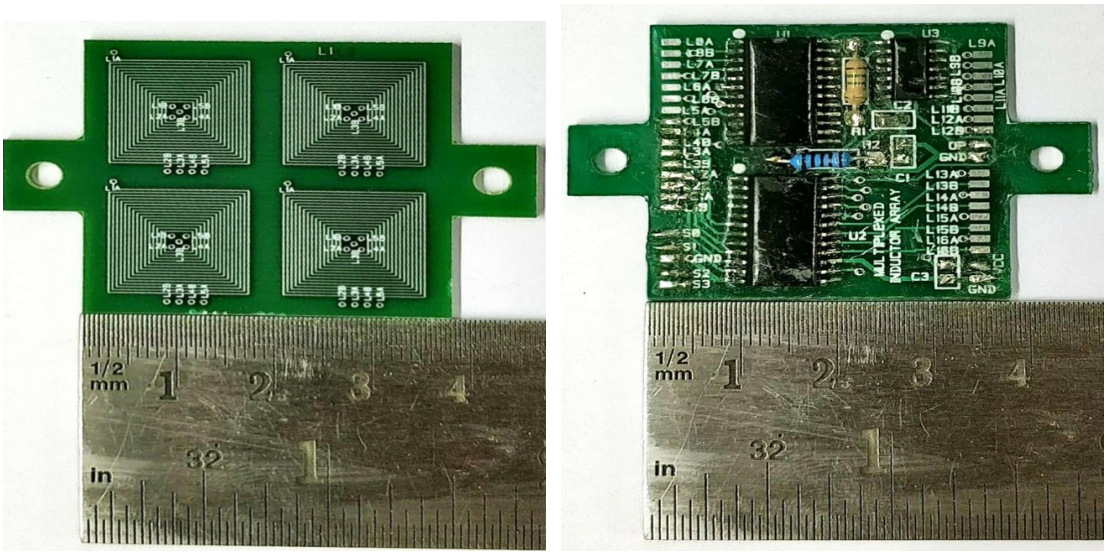

(a) (b)

Figure 3.4: (a) Multi-layer inductor array pickup coil (b) Multiplexed Inductor LC oscillator

3.2.3 Design of Cryogenic LC oscillator

A Multiplexed inductor cold electronic LC oscillator was realized making use of commercially available inverter ICs, multiplexer ICs and other components, for getting a frequency modulated angular position data corresponding to the output from the selected pickup coil. The schematic circuit diagram is shown in figure 3.5. Two multiplexers are used to switch between the four different inductors depending on the control signal given to them. Thus the output from the LC oscillator will be from the inductor to which it is switched. The required performance and temperature stability of frequency were achieved with meticulous screening of the individual components and ICs and by subjecting them to thermal cycling down to 77 K.

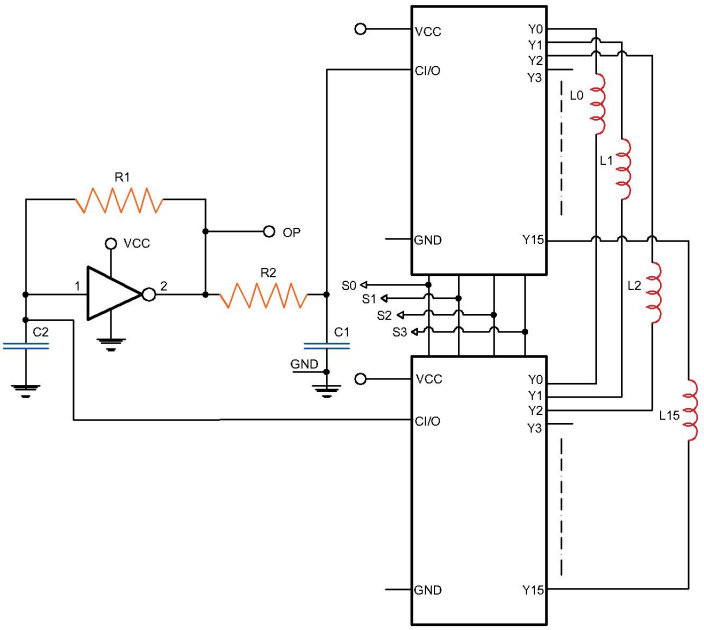

Figure 3.5: Multiplexed inductor Digital Inverter based LC Oscillator Circuit

The operating frequency can be derived from equation (3.5),

$$f_{operating} \leq \frac{SRF}{10} \tag{3.5}$$

where, SRF is self-resonant frequency. For the five layer inductor, SRF was found out to be 1.71 MHz using an impedance analyzer. Hence, the operating frequency

has to be less than 171 kHz. Based on these details, an operating frequency of 120 kHz was chosen. Since the frequency of the LC oscillator is

$$f_{operating} = \frac{1}{2\pi\sqrt{L_{total}C}} \tag{3.6}$$

A suitable 'C' value can be selected to have the frequency around 120 kHz. The temperature effect on the frequency of the oscillator, which is 73 Hz/K is shown in figure 3.6.

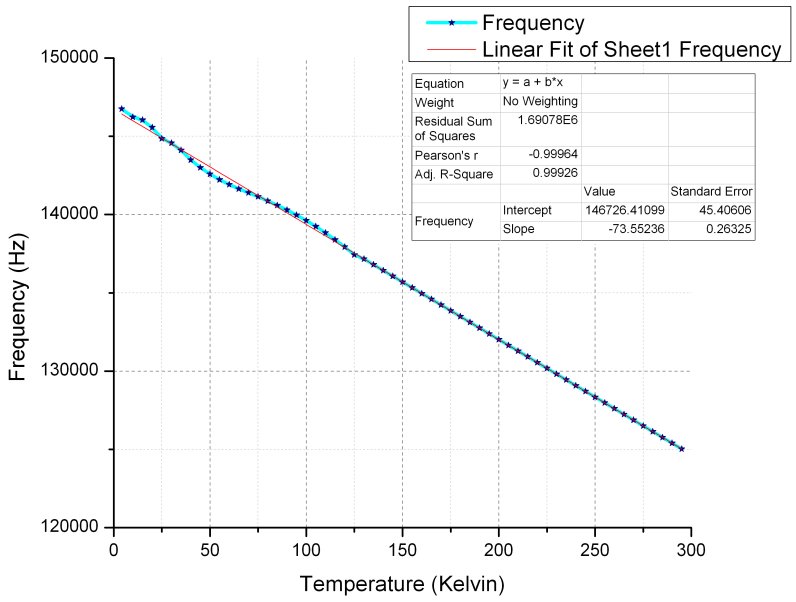

Figure 3.6: Frequency variation at different temperatures

The angle is determined from 2 parameters (a) The frequency data corresponding to all the 4 inductors and (b) The difference in frequency between previous and current positions ($\triangle$f). The second parameter is needed because, when the segment is entering the proximity of one inductor, an increase in frequency associated with that inductor is observed. Similarly, when the segment leaves the proximity of the inductor a reduction in frequency is observed. To distinguish between these values, $\triangle$f is utilized. $\triangle$f can also be used to determine the direction of rotation.

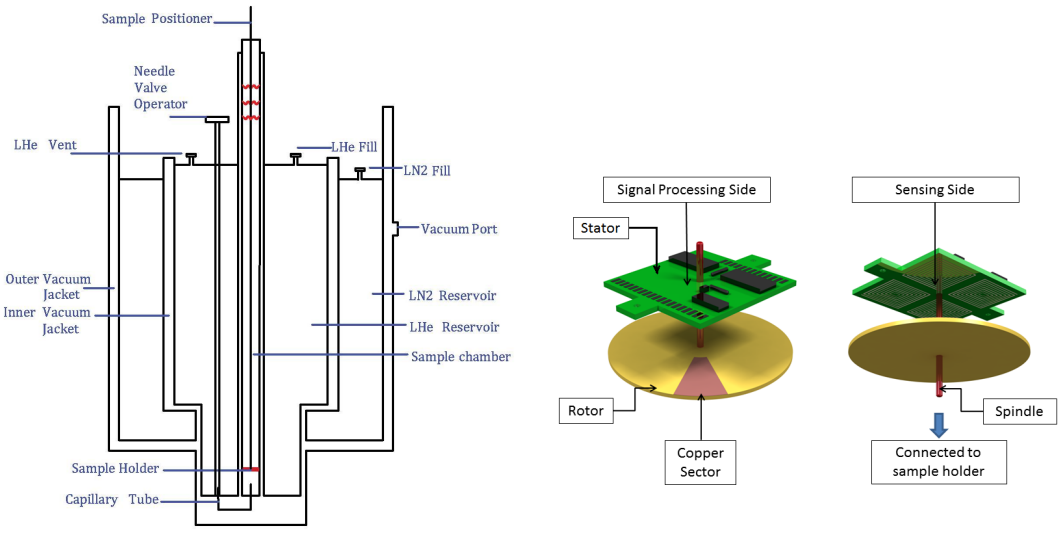

(a) (b)

Figure 3.7: Experimental setup used for testing the sensor (a) Schematic of liquid He cryostat used for the experiment (b) Schematic of the multiplexed array sensor along with the rotating target with a copper sector rotating on a central shaft

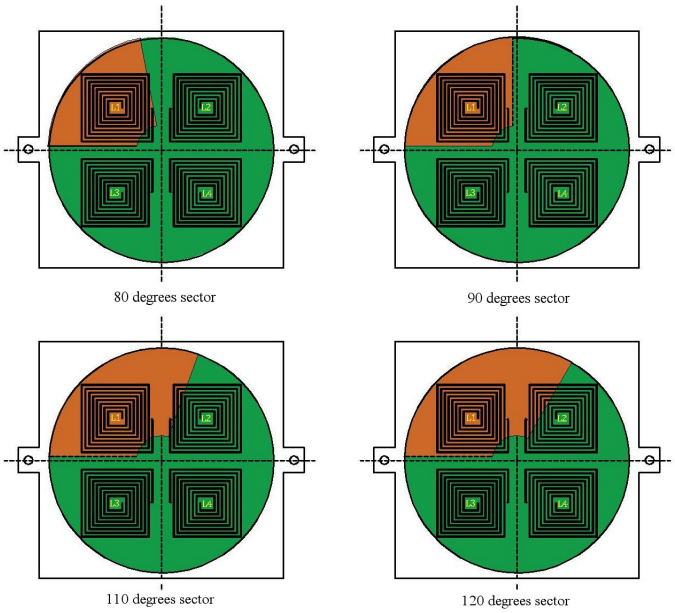

Figure 3.8: Rotor segment sizes varied from 80°to 120°(top view)

3.2.4 Rotor optimization

The sensor consists of two parts 1) A stator section which contains the sensing coils and the cold electronics and 2) A rotor section which is separated from the stator

with nylon washers kept at a height (h) above the stator as shown in figure 3.7 (b). The stator has a small non-magnetic metallic segment which acts as the target for the eddy current sensor. The sensitivity of the sensor is a strong function of three different parameters of the rotor section a) The sector size (expressed in angle) b) The material that makes up the rotor sector element and c) The thickness of the conductor material of the rotor segment. Sector size optimization is purely a geometrical problem. From the point of view of the sensor, the stator (each sensing coil) covers an area of 80°. If the rotor segment is designed with an area less than 80°, then the output frequency associated with each coil will have distinct peaks and there will be an angle at which the sensitivity is zero (at the peak frequency) as shown in figure 3.9.

As the segment area increases from 80°to 120°, in increments of 10°as shown in figure 3.8, the output frequency from the inductors begins to merge together as observed in figure 3.9. When the frequency of one inductor is about to peak (120°), the second inductor starts to increase as seen in figure 3.9. Hence the optimum size of the sector area without zero sensitivity will be 120°. If the segments are too big, then the peaks will be very close to each other and the sensor will loose the span of 360°.

Another important point to note is the material that is selected to make the rotor segment. In the current work, a copper segment is selected due to its ease of fabricating accurate segments by etching the copper out from the FR4 based PCB. It should be noted that any material can be chosen to fabricate the rotor segment depending on the application. If the application requires the use of Al or a Nb segment, then a separate calibration process has to be done with that specific rotor element. The limiting criteria are that the fabrication process available and the material has to be a non-magnetic conductor. In fact, copper may be the most inefficient material as the rotor segment because of it's large conductivity variation with temperature (Residual Resistivity Ratio (RRR = $\frac{\sigma_{4K}}{\sigma_{273K}}$) usually from 10 to 2000). In the case of an eddy current sensor, other than the sensor dimensions and arrangement of the target, the inductance variation of the sensing coil is also a strong function of the conductivity of the material (σ). If the rotor segment chosen has a large conductivity variation with temperature, then the sensor will also have large frequency variation with temperature. The optimum material is the one with very low RRR.

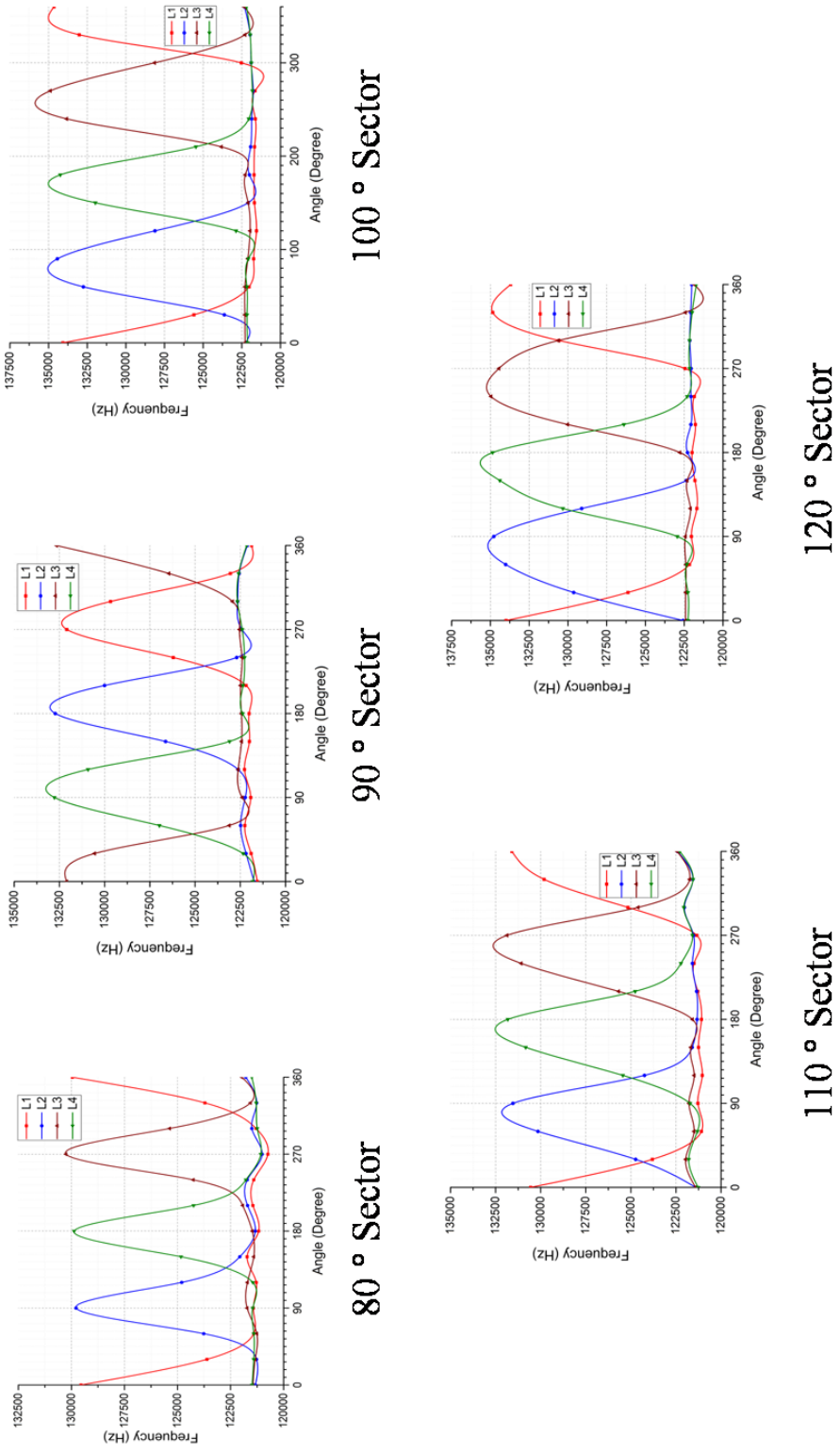

Figure 3.9: Frequency output from the sensor with different sector angles for the rotor segment (290 K)

Thickness of the conducting material becomes relevant when the frequency of operation is low at 290 K. If the thickness is selected to be greater than the skin depth at 290 K, then this condition will always be satisfied throughout the entire temperature range (290 K - 4 K). This is due to two supporting factors. The conductivity of the material increases with reduction of temperature and frequency of the senor increases with temperature. The skin depth is an inverse function of these factors. Therefore, If the thickness is greater than that skin depth at 290 K, it will always be greater than that at any temperature less than 290 K. Once the skin depth becomes less than the thickness, the inductance variation of the eddy current sensor will be independent of the thickness as shown in [76].

3.3 Experimental setup and DAQ

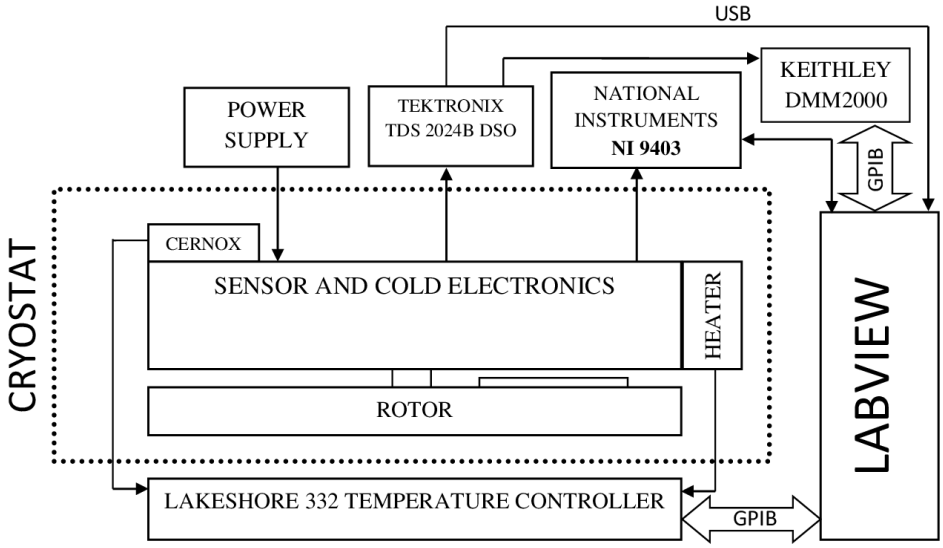

Figure 3.10: Schematic of DAQ

The schematic of the cryostat used for the experiment is shown in figure 3.7 (a). It has a liquid nitrogen jacket surrounding a liquid helium (LHe) reservoir with common vacuum space. A capillary tube with needle valve couples the middle test chamber with the liquid helium reservoir. The flow of LHe to the test chamber is controlled by needle valve. A heater at the bottom of the test chamber is used to maintain different cryogenic temperatures for the Device Under Test (DUT).

The sensor along with the target with a copper sector set at a particular angle as shown figure 3.7 (b) was mounted at the end of the sample position rod.

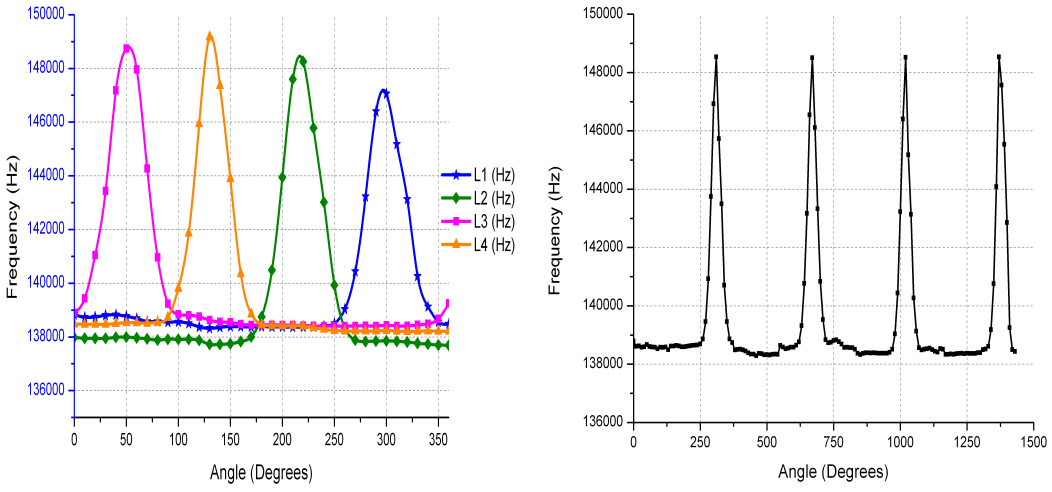

Figure 3.11: Experimental results at 77 K (a) Output frequency for 360°rotation (b) Output frequency of single inductor for four cycles (c) Piecewise linearized sensitivity for single inductor output

An FRP based PCB rotor with an etched copper sector of dimension 20 mm× 10 mm×250 μm was used for the experiment. The distance between the sensor and rotor was kept at 0.5 mm using a nylon washer as spacer. In the current

experiment, each angle is set before cooling, once angle is set, the whole system is cooled to required temperatures. The schematic of the measurement system is shown in figure 3.10. The LabVIEW software to interface the digital storage oscilloscope, Keithley 2000 DMM and Lakeshore 332 temperature controller were used for data acquisition from the sensor and cold electronics kept in the cryogenic environment. NI 9403 is used to generate the switching signal for the MUX ICs for switching between the inductors. The MUX ICs are switched in sequence from L1-L2-L3-L4 with the help of the switching signals generated using LabVIEW program. The time delay between the individual signals is set at 250 ms for the current experiment. This delay was required because a standalone DMM was used to acquire the frequency data.

3.4 Experimental results and discussion

Table 3.3: Piecewise linearized sensitivity of the sensor

Sl.no.	**Parameter**	**Value**
1	Accuracy (angle in °)	±2°(at 77 K)
2	Span	360°
3	Maximum Sensitivity	407 Hz/°(at 77 K)
4	Average coefficient of temperature	73 Hz/K

Figure 3.11 (b) shows the response curves of a single inductor (L_1) when the sensor is operated at 77 K. To determine the statistical accuracy and repeatability, the sensor was rotated through 10 cycles of 360°of which four cycles (360°×4) of a single inductor is shown in figure 3.11 (b). It can be seen that the sensor has identical response in all four cycles. The accuracy of the sensor was determined by the standard statistical procedure which involved the calculation of the mean output frequency at a particular angle. From the mean output frequency, the standard deviation for that particular angle was determined. From this standard deviation, the mean standard deviation was determined. This procedure was repeated for the entire 360°and the maximum value for the mean standard deviation was determined to be (±2°). Figure 3.11 (a) shows all four inductor responses when the copper sector moves through 360°. The difference in the peak frequency values of different inductors is attributed to the slight variation in the inductance between

each of the four coils. There can also be slight difference in height (h) that might have occurred due to repeated mounting of the sensor. Figure 3.11 (c) shows the output from a single inductor and piecewise linearized to determine the maximum sensitivity. The results are summarized in Table 3.3. The sensitivity of the angular sensor can be further improved by increasing the excitation frequency, which can easily be done by adjusting the capacitance of the oscillator circuit. The size of the copper sector used as the rotor element also has an effect on the overall span of the sensor. If the sector is too small, there will be a large dead space between the frequency bands of consecutive coils. So, an appropriate size is chosen for the experiment.

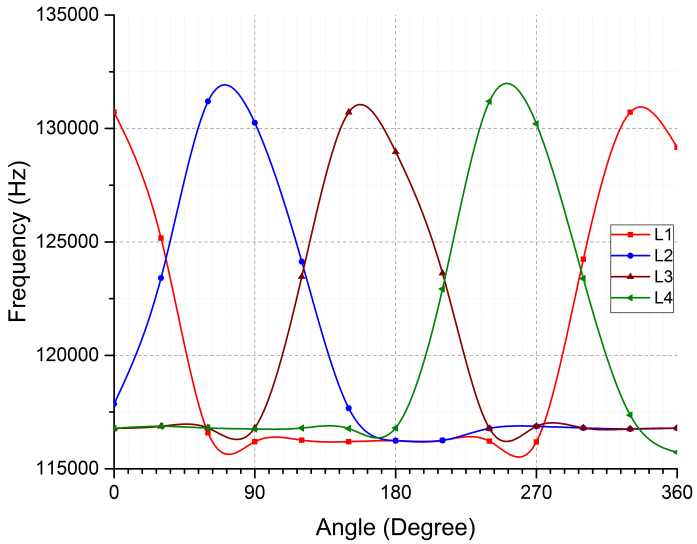

Figure 3.12: Frequency output from the sensor with 120°an at 4.1 K

The sensor was also tested at 4.2 K and the output from the sensor is shown in figure 3.12. The circuit parameters (feedback resistance) was slightly adjusted from the 77 K experiment to achieve better frequency stability as well as reduced distortion in the output waveform observed at lower temperatures. This resulted in a reduction of base frequency (80 kHz at 290 K) and also reduced the peak frequency at 4.2 K to 135 kHz from 160 kHz. Accuracy and repeatability of the sensor at 4.2 K is not reported as this would require at least a minimum of 10 full 360°cycles with each cycle having 16 experiments. This limitation was mainly because there was no mechanism to rotate the rotor once the sensor was cooled and this would require a large amount of LHe.

3.5 Conclusion

A novel concept of angular displacement measurement using the multilayer planar inductor based eddy current transducer for a metallic surface was designed and tested to work satisfactorily at 4.2 K. A cold electronics based LC oscillator circuit which converts the inductance change of the sensing element into a frequency change was also designed and tested. The designed multilayer planar inductor was analyzed using E4990A impedance analyzer and its parameters were compared with the theoretical values. The noise performance of the transducer at cryogenic temperatures was also studied. A piecewise sensitivity chart for the sensor at 77 K for various angular displacement range was also obtained. A 24 point calibration of the sensor was done at 4.2 K and the sensor parameters were determined.

Chapter 4

RRR measurement using planar inductors

4.1 Introduction

Among all the pure metals, niobium (Nb) with its high critical temperature and critical magnetic field is the favorite material for the fabrication of superconducting RF cavities. Nb is chemically inert (at room temperature the surface is covered by a protecting oxide layer), it can be machined, deep drawn, welded and is available as bulk and sheet material of any size.

Superconducting RF cavity requires high thermal conductivity to dissipate the RF power into the surrounding liquid Helium (He) as shown by Wasserbäh, W. (1978) and Singer, W et al. (2010) [57, 77, 78]. This requires Nb of high purity. Residual Resistivity Ratio (RRR) gives a direct indication of the purity of the Nb. RRR is defined as $\frac{R_{290K}}{R_{10K}}$. There are numerous other definitions depending on the method of measurement technique used. Here, R_{290K} is the resistance of the material at 290 K and R_{10K} is the resistance at 10 K. It has also been shown that there exists a direct relation connecting RRR with the thermal conductivity (λ). Hence, facilities which work on particle accelerators use RRR as the first indicator for the absolute performance of the cavity. The conventional method of RRR measurement involves the 4-probe technique to measure the electrical resistance. There are two major limitations in this method- (1) It is a destructive process in which a piece of a specified length is cut from the bulk material and

is used for RRR measurement. (2) It is non-local in nature i.e., the measured resistance is an average over the entire length. During cavity fabrication, Nb is subjected to multiple stages of treatments (annealing, chemical & electrochemical polishing, electron beam welding, centrifugal barrel polishing etc.). At each stage, the purity of the Nb can be significantly diminished. After the SRF cavities are fabricated, the RRR values cannot be measured. This limitation can be overcome by adopting AC measurement techniques. Few AC RRR measurement techniques have been proposed by Safa, H., et. Al. (1997) and also Singer, W., & Proch, D. (1996) etc [47, 48]. But, the main drawback with the aforementioned methods is the absence of theoretical relation between RRR and the measured parameter. A detailed account of the literature review on RRR measurement techniques for Nb is presented in chapter 1.

The non-contact RRR measurement methods using eddy current principle and the boundary conditions for interpretations are described in this chapter. Three different approaches to measure the RRR of Nb were explored. The first method utilized existing eddy current principles for measurement of conductivity extended to the cryogenic temperatures. The existing theoretical equations connecting the conductivity and impedance change of the sensor were modified and appropriate corrections were applied to accurately measure the conductivity and RRR for Nb. The second approach used the change of slope of frequency response of series inductance curve that occurs (inflection point) when the skin depth becomes equal to the thickness of the sample. From the plot of the above curve, the inflection points at both the temperatures were determined and from that the RRR was calculated. The final approach used multiplexed LC oscillator circuit to convert the inductance change into corresponding frequency change. The thermal effects on the circuit were canceled by taking a reference coil in the same conditions and using the δf the RRR was estimated.

4.2 Principle of eddy current sensors

An analytical model to describe the interaction between the sensor and the target can be achieved by considering the sensor target interaction as a transformer, with the primary coil (sensing coil) having an impedance given by $Z_0 = R_0 + j\omega L_0$. The secondary coil of the transformer has an inductance L_m provided by two different

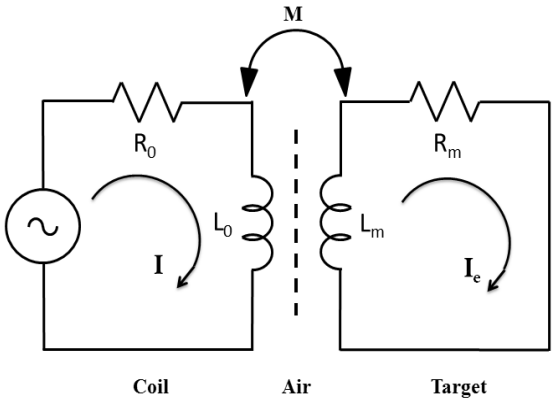

Figure 4.1: Transformer model of eddy current sensor

terms. The first being the inductance due to the current loops circulating on the surface of the conductor and the second being the leakage inductance of the target. The real part of the secondary coil is the component associated with the dissipated power by the eddy currents on the conductive target. Hence, the secondary impedance can be written as $Z_t = R_m + j\omega L_m$ as shown in figure 4.1. Assuming that a current I flows in the primary circuit of the coil and a current I_e flows on the secondary loop (eddy current), and on applying Kirchoff's voltage law (KVL) on loops (1) and (2) we get,

$$IR_0 + j\omega M_1 I_e = V \tag{4.1}$$

$$j\omega I_e L_m + I_e R_m - j\omega M_2 I = 0 \tag{4.2}$$

Here, $M_1 = k\ L_m$ and $M_2 = k\ L_0$, where k is the coupling coefficient.
From equation 4.2,

$$I_e = \frac{j\omega M_2 I}{j\omega L_m + R_m} \tag{4.3}$$

Substituting equation 4.3 in 4.1 and defining the effective impedance as seen by the excitation source as $Z_c = \frac{V}{I}$, we get,

$$Z_c = \frac{V}{I} = [R_0 + \frac{k^2\omega^2 L_0 L_m R_m}{R_m^2 + \omega^2 L_m^2}] + j\omega L_0[1 - \frac{k^2\omega^2 L_m^2}{R_m^2 + \omega^2 L_m^2}] \tag{4.4}$$

Here, the modified resistive component R_c is given by,

$$R_c = R_0 + \frac{k^2\omega^2 L_0 L_m R_m}{R_m^2 + \omega^2 L_m^2} \tag{4.5}$$

and the modified reactance X_c is given by,

$$X_c = \omega L_0[1 - \frac{k^2\omega^2 L_m^2}{R_m^2 + \omega^2 L_m^2}] \tag{4.6}$$

In the absence of a target, the sensor impedance becomes Z_0. When a conductor approaches the sensor, the reactance term $X_c < X_0$ is given by equation 4.6. This can be physically understood by knowing that the effective magnetic field of the coil is reduced by the field generated by the eddy currents. This results in the source seeing a lower reactance as the conducting target approaches. Similarly, the eddy currents induced on the surface of the conductor will heat the conductor. These losses are compensated by the source to the primary. Therefore the source experience an increase in resistance of the coil. Hence, $R_c > R_0$ when the conductor is in the vicinity of the coil.

The useful sensor data is generally the normalized impedances given by,

$$R_{cn} = \frac{R_c - R_0}{X_0} \tag{4.7}$$

$$X_{cn} = \frac{X_c}{X_0} \tag{4.8}$$

Substituting equations 4.5 and 4.6 in equations 4.7 and 4.8 respectively, we get

$$R_{cn} = \frac{k^2\omega L_m R_m}{R_m^2 + (\omega L_m)^2} \tag{4.9}$$

$$X_{cn} = 1 - \frac{k^2\omega^2 L_m^2}{R_m^2 + (\omega L_m)^2} \tag{4.10}$$

From equations 4.9 and 4.10, it can be shown that,

$$\boxed{X_{cn} = 1 - \frac{\omega L_m}{R_m} R_{cn}} \tag{4.11}$$

Equation 4.11 means that the slope of the R_{cn} - X_{cn} plot (Normalized impedance graph) will be inversely proportional to R_m or the conductivity of the target. This

is the principle that is used for measuring the conductivity of a specific target.

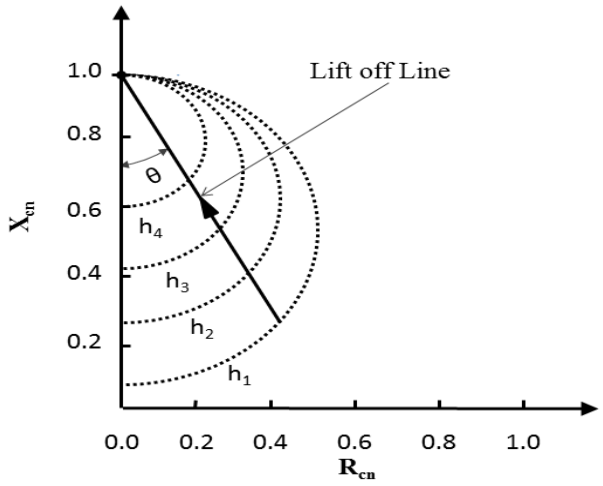

Figure 4.2: Normalized impedance plane

It can also be shown that the locii of points (R_{cn},X_{cn}) for different values of frequency for the same target, placed at the same distance from the sensor, will be a circle. In reality, this curve follows a tear drop shape with smaller radii for a larger sensor to target separation (lift-off) as seen from figure 4.2.
The relation between the slope of the lift-off line and the electrical conductivity for a specific geometry the of sensor has been well established [40, 79]. The linear relationship of the slope of lift-off line is a reference number given by $(\frac{r}{\delta})$, where r is the mean coil radius for a planar inductor and δ is the skin-depth given by,

$$\delta = \frac{1}{\sqrt{(\mu_0 \pi \sigma f)}} \tag{4.12}$$

where σ is the electrical conductivity of the target, f is the frequency of operation and μ is the permitivity. They showed that for a planar inductor, the relation between the slope and the reference number is given by,

$$cot\theta = b + a\frac{r}{\delta} \tag{4.13}$$

From equation 4.12 and 4.13, the electrical conductivity of the target δ is obtained as,

$$\boxed{\sigma = \frac{(cot\theta - b)^2}{\mu \pi a^2 r^2 f}} \tag{4.14}$$

Here, a and b are application dependent, mainly on the coil geometry and the temperature of operation. If a single sensor is operated at two different sets of temperatures, it will correspond to two different values for a and b, assuming that coil geometry does not have any significant change.

4.3 RRR measurement using 4-probe electrical resistance method

The standard used for calibration and testing of the of RRR measurement methods were obtained by conducting RRR measurements on standard samples for which the values are known precisely. In view of this, an experimental setup was developed to measure the electrical resistivity of the samples down to 4.2 K using the 4-probe electrical resistivity measurement method. The resistance measurements were performed using the above method where the current inputs are at the ends of the sample and the voltage terminals are in between the current terminals so as to minimize the effect of non-uniform current distributions. The 4-probe resistance measurements were typically performed with a precision of 100nV after low-pass filtering. Thermo-voltages were eliminated by averaging over voltage readings obtained with reversing the current polarities. The typical measurement current is 100 mA. Samples used were typically of lengths 15-20 mm and widths 1-2 mm.

4.3.1 Experimental setup and DAQ for the 4-probe electrical resistance method

The RRR measurements were conducted using Janis LHe SuperVariTemp(SVT) cryostat to sustain a stable temperature environment. Samples of specified lengths were mounted on the sample holder made out of FR4 material. The samples were thoroughly cleaned in dilute acid bath followed with acetone cleaning. In order to ensure proper contacts, 52 gauge copper wire was wrapped on the sample at each contact point and solder was applied on top to provide a really hard and stable contact with the Nb surface. The sample was mounted in its place without any movements by tightly holding it in place using cable tags through the FR-4 sample

holder. Cernox temperature sensor was placed as close to the sample as possible to obtain stable temperature readings. Additional thermal contacts were ensured by wrapping the sample along with temperature sensor using non-adhesive Kapton tape.

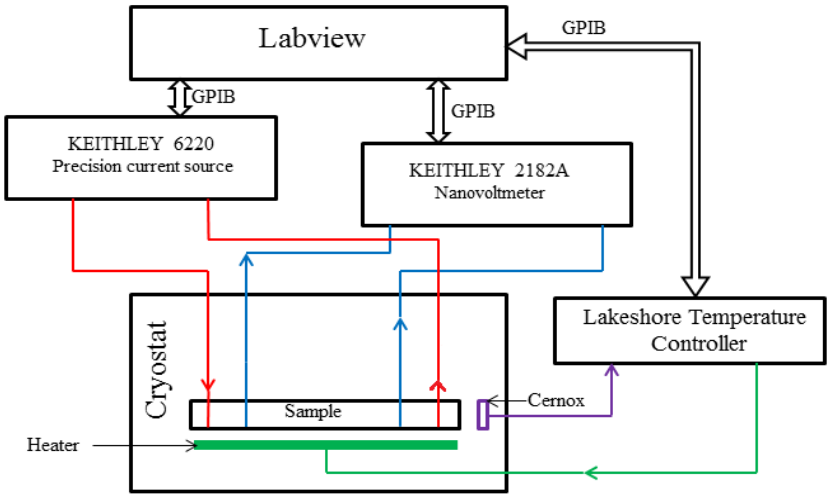

Figure 4.3: A Schematic of the RRR measurement system using the 4-probe electrical resistance method

The measurement setup used a combination of Keithley 6220 precision current source and Keithley 2182A nanovoltmeter in a delta configuration (specific configuration settings for measuring low resistance) as shown in figure 4.3. The current direction was switched at a low frequency (2Hz) through the LabView program. An average of two cycles was taken to cancel the effects of thermo EMF effects. The LabView program was used to acquire the measured voltage after low pass filtering and logged along with the temperature values acquired from the Lakeshore temperature controller. The voltage values acquired were with a precision of 100 nV and was limited by the capability of the current source.

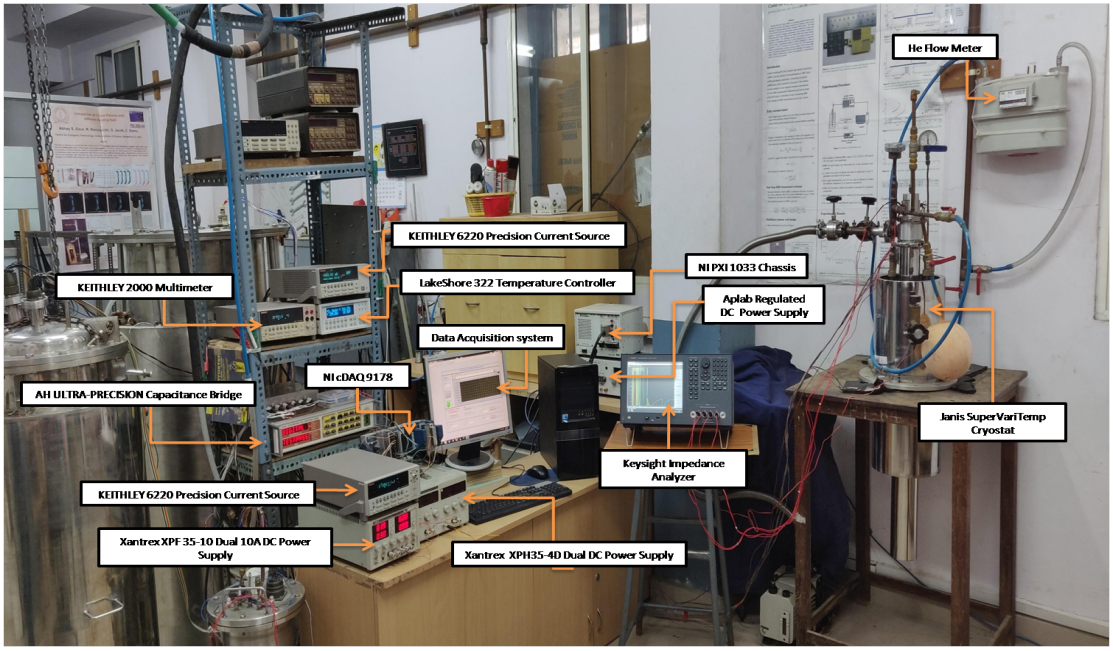

Figure 4.4: A photograph of the experimental setup along with the cryostat used for the experiment

A photograph showing the experimental setup along with the Janis cryostat that was used for the experiment is shown in figure 4.4. The electrical wiring inside the cryostat was with 52 gauge enameled copper wires to reduce the heat load into the sample chamber of the cryostat. A stable temperature for measurement (at ∼10K) was maintained by a combination of heater, helium reservoir valve opening and Cernox temperature sensor. The voltage outputs were taken out through dedicated feedthrough available on the sample positioner rod of the cryostat.

4.3.2 Experimental results

Experimental results for the resistivity measurement using the 4-probe electrical resistance method is shown in figure 4.5. It can be seen that the resistivity of sample with RRR = 3.21 is higher at room temperature as well at cryogenic temperature compared to the other three samples. This maybe due to the lower purity of the material. The rated purity of the sample with RRR value of 3.21 was 99.95% whereas that for the other three samples were 99.995% which are normally selected for RF cavity fabrication. The transition from normal conducting to superconducting at zero magnetic field cannot be seen from the plot of all the

four Nb samples because of different scales associated with each sample.

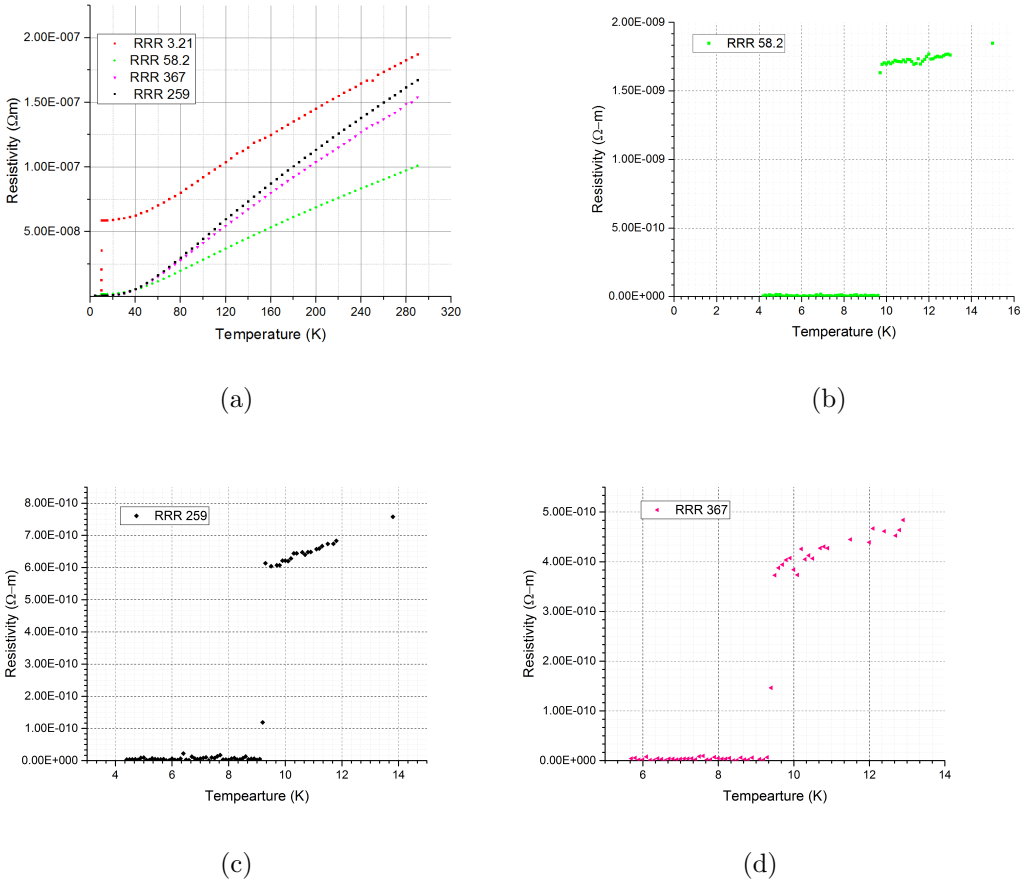

Figure 4.5: (a) Experimental results showing resistivity variation for 4 samples (b) Expanded section around the superconducting transition region for RRR = 58.2 and at Zero magnetic field (c) Expanded section around the superconducting transition region for RRR = 259 and at Zero magnetic field (d) Expanded section around the superconducting transition region for RRR = 367 and at Zero magnetic field

The four samples with four different RRR were used as the reference for measuring and calibration of different non-contact based measuring techniques which will be described in subsequent sections.

4.4 Method 1: Dual slope RRR measurement technique

Residual Resistivity Ratio (RRR) is defined as the ratio of resistivity of the conductor (here Nb) at room temperature (ρ_{290K}), to the resistivity just above the critical temperature (ρ_{10K}). Here, from equation 4.14, the modified equation for RRR is obtained as,

$$\boxed{\frac{\rho_{290K}}{\rho_{10K}} = \frac{(cot\theta_{10K} - b_{10K})^2}{(cot\theta_{290K} - b_{290K})^2} \frac{a_{290K}^2}{a_{10K}^2} \frac{f_{290K}}{f_{10K}}} \tag{4.15}$$

Here, the two slopes $\cot\theta_{290K}$ and $\cot\theta_{10K}$ are slopes of the lift-off lines at selected frequencies f_{290K} and $f_{\sim 10K}$. A set of values for a and b at two different temperatures have to be determined in order to use equation 4.15. These were determined by using three of the four samples to calibrate the sensor. The fourth sample is used as the unknown sample and the calculated a and b values were used to determine the RRR and the electrical conductivity using equations 4.15 and 4.14.

4.4.1 Multilayer planar coil design

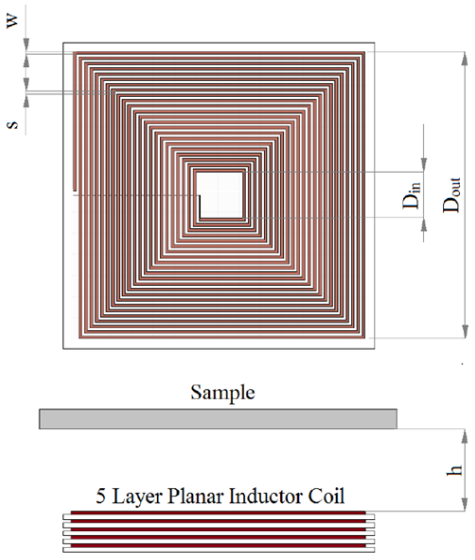

Inductor parameters	
Parameter	Value
Din	1.9 mm
Dout	14 mm
Conductor thickness (w)	0.127 mm
Conductor spacing (s)	0.254 mm
Number of turns (N)	15
Fill Factor	0.7610

Figure 4.6: PCB based Multilayer planar inductor

Two coils of same dimensions were used as the sensing elements for the experiment.

One was used to provide the reference impedance Z_0 and the other, was kept in the presence of the target which provided the modified impedance Z_c. A multilayer planar inductor PCB based coil design was chosen as this technique can be scaled down and used to produce an elaborate array of coils for a complete surface RRR mapping. It was necessary to keep the dimensions of the coil as small as possible due to various considerations viz. localized measurement, cryostat bore diameter etc. The other constrains are the frequency of operation and the Q factor of the coil. Typical parameters of a single layer planar inductor are listed in figure 4.6.

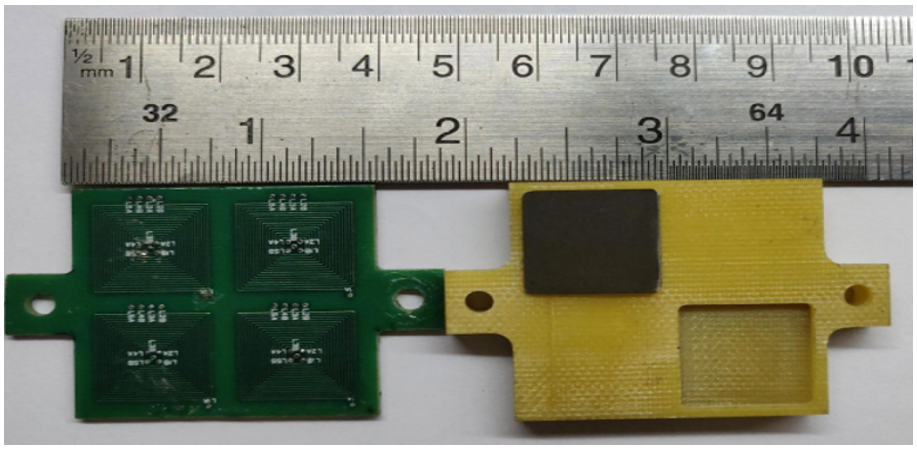

Figure 4.7: A multilayer planar inductor sensing array

Figure 4.7 shows the actual sensing element along with the Hylam (Bakelite) sample holder. Here, one coil was used to measure the reference impedance Z_0 at every temperature and the other three coils can be used as the sensing elements under the influence of the Nb target.

4.4.2 Experimental setup and measurement procedure

Four different samples of different RRR values (1) 3.21 (2) 58.2 (3) 259 and (4) 367) - which were measured accurately by 4-probe measurement technique, were used in this experiment. Here, the samples 1, 2 and 4 were used as the calibration standards to obtain the a and b sensor parameters defined in equation 4.15. The third one was used as an unknown sample and the conductivity as well as the RRR were measured using equation 4.15. Two measurements were done at every temperature, one to measure the reference impedance Z_0 and the other, to measure

the modified impedance Z_c. The sample was mounted in a custom made sample holder made of Hylam sheet . Initially, the sensor to target distance was kept at 0.5 mm. The impedance of the coil was acquired from 290 K to 4.1 K. This procedure was repeated for the same sample, kept at various lift-off distances by varying it from 0.5 mm to 3 mm. Similarly, all the other samples were tested.

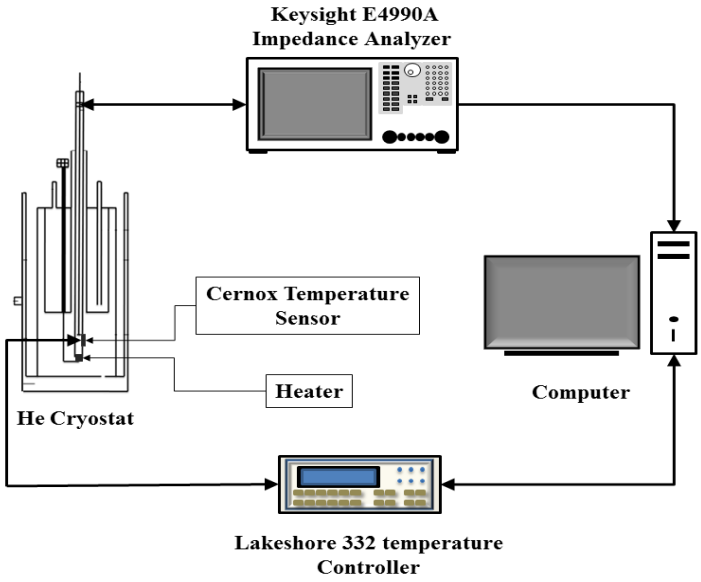

Figure 4.8: Schematic of measurement setup for dual slope RRR measurement

Figure 4.8. shows the schematic for the measurement of the impedance of the planar coil in the presence of the target. An impedance analyzer was used to measure the real and imaginary parts of the coil impedance at specific frequencies. The range of frequency to sweep was carefully determined based on the thickness of the target as well as the operating temperature. A cryostat with a temperature sensor (Cernox) and a heater combination was used to maintain a stable temperature. The data was continuously acquired using DAQ system with the help of the LabView software.

4.4.3 Experimental results

Determining a and b at 290 K and 10 K

To determine the a and b values described by equation 4.15, three different samples with RRRs of 3.21, 58.2 and 367 were used along with their measured conductivity

values (4-probe method) to obtain a combined cotθ vs. $\frac{r}{\delta}$. A best linear fit for the data was obtained by regression fit algorithm and the coefficients of this linear fit was used as the a and b parameters. The a and b values at two different temperatures (290 K and 10 K) were then used to determine the electrical conductivity of the target at the required temperatures.

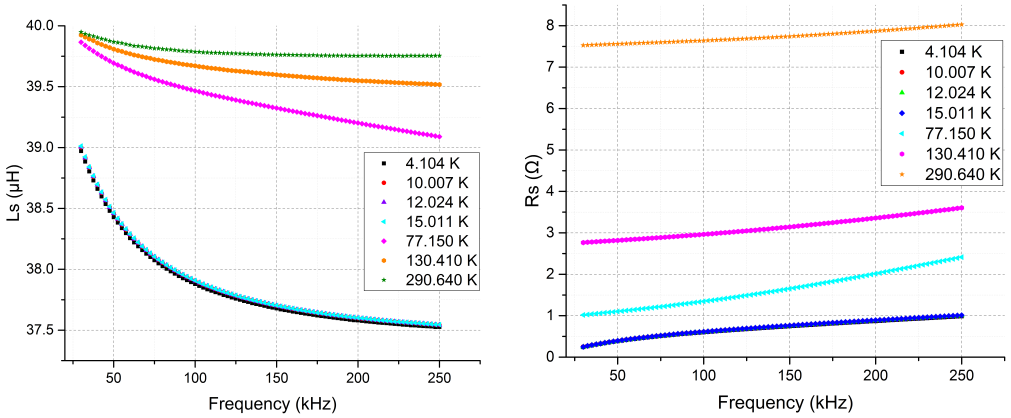

(a) (b)

Figure 4.9: (a) Frequency response (L_s) of the sensing element at different temperatures (b) Frequency response (R_s) of the sensing element at different temperatures

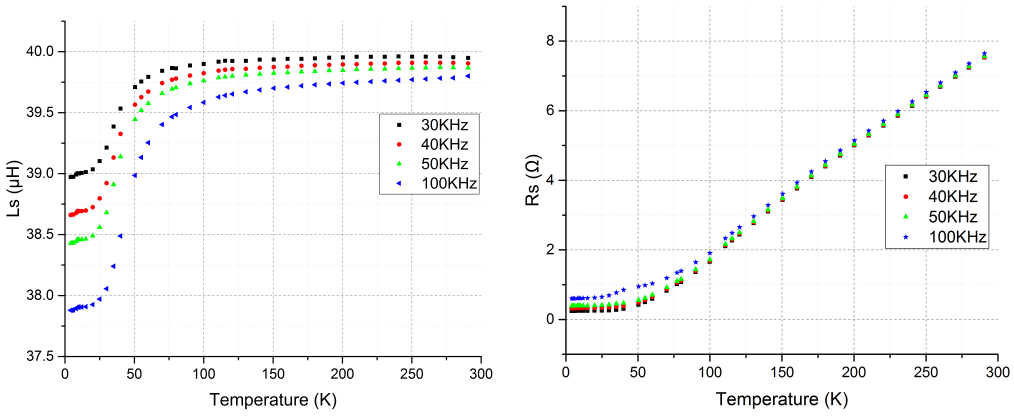

(a) (b)

Figure 4.10: (a) Temperature response (L_s) of the sensor without a target (b) Temperature response (R_s) of the sensor without a target

The reference impedance Z_0 (R_0 + j2πL_0f) measured at different temperatures is

shown in figure 4.9. It should be noted that the inductance value of the sensor decreases by a small value with decrease in temperature, but the decrease in the series resistance component of the impedance is substantial when compared to its base resistance at 290 K. This is understandable as the coil is made of copper and there will be reduction in resistance with the temperature. This also means that the sensing coil becomes more and more ideal as the sensor is cooled down to cryogenic temperatures.

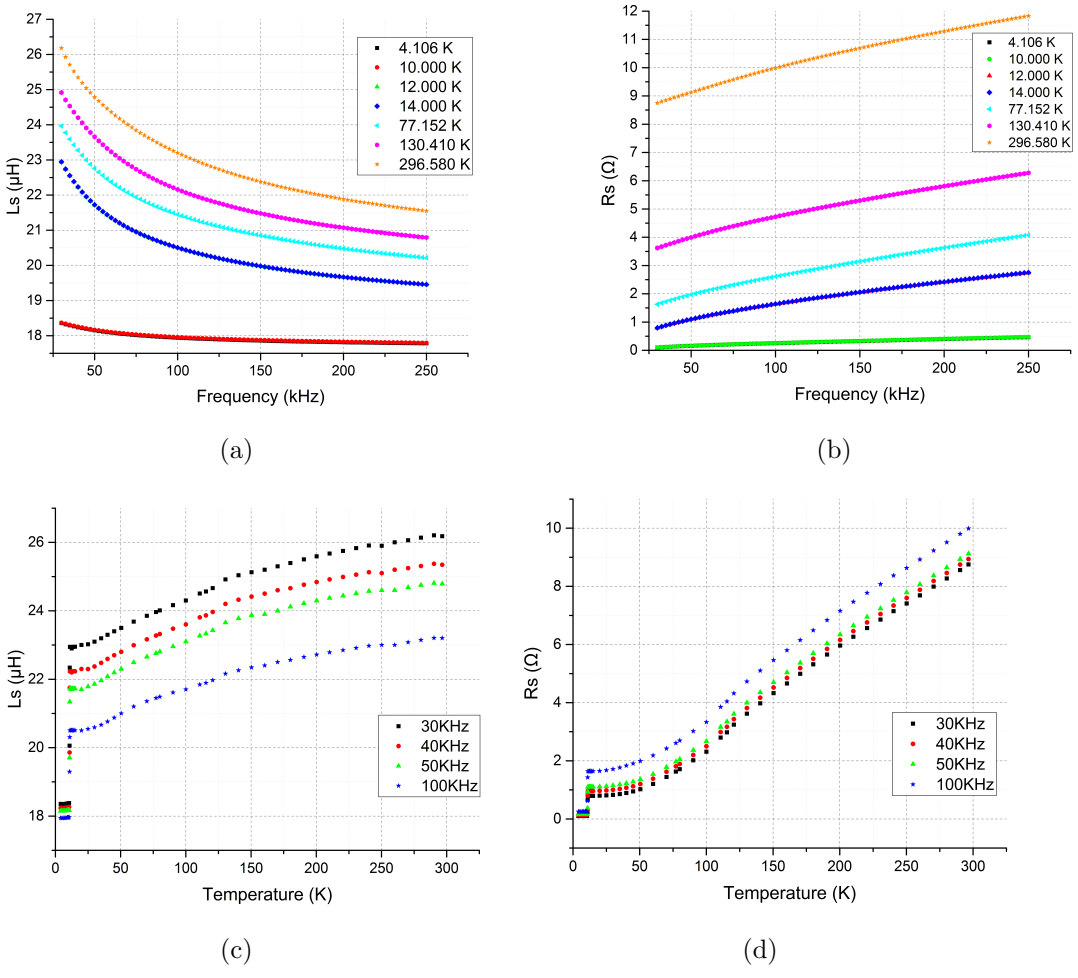

Figure 4.11: Frequency response and temperature response of for the impedance componets of the sensor for a RRR of 3.21 and a lift-off of 1 mm

From the figure 4.10 (a), it can be seen that the sensor has almost negligible change in inductance up to 50 K. Then there is a sudden change in inductance value till around 25 K and then it saturates to a stable value. The response

of the sensor makes it unsuitable as a sensing element in that small margin of temperature between 50 K and 25 K. R_s behaves exactly like the resistance profile of copper with very low resistance at 4.2 K and a linear resistance profile with temperature. After the reference impedances were established, the impedance under the influence of the Nb sample was measured using the schematic described in the previous section.

Figure 4.11 (a) and (b) shows the frequency response of L_s and R_s with a lift-off of 1 mm at a few different constant temperatures for a RRR of 3.21. Figure 4.11 (c) and (d) shows the temperature responses of the impedance components at some specific constant specific exitation frequency for RRR of 3.21. Similarly with reference to figure 4.11, the response of the sensor was taken for at least 2 different lift-offs for the entire set of samples. From the values of the reference impedances Z_0 and Z_s, the normalized impedance plots were generated using equations 4.7 and 4.8. The normalized impedance plots for the three samples at two different temperatures and two different lift-offs shown in figure 4.12.

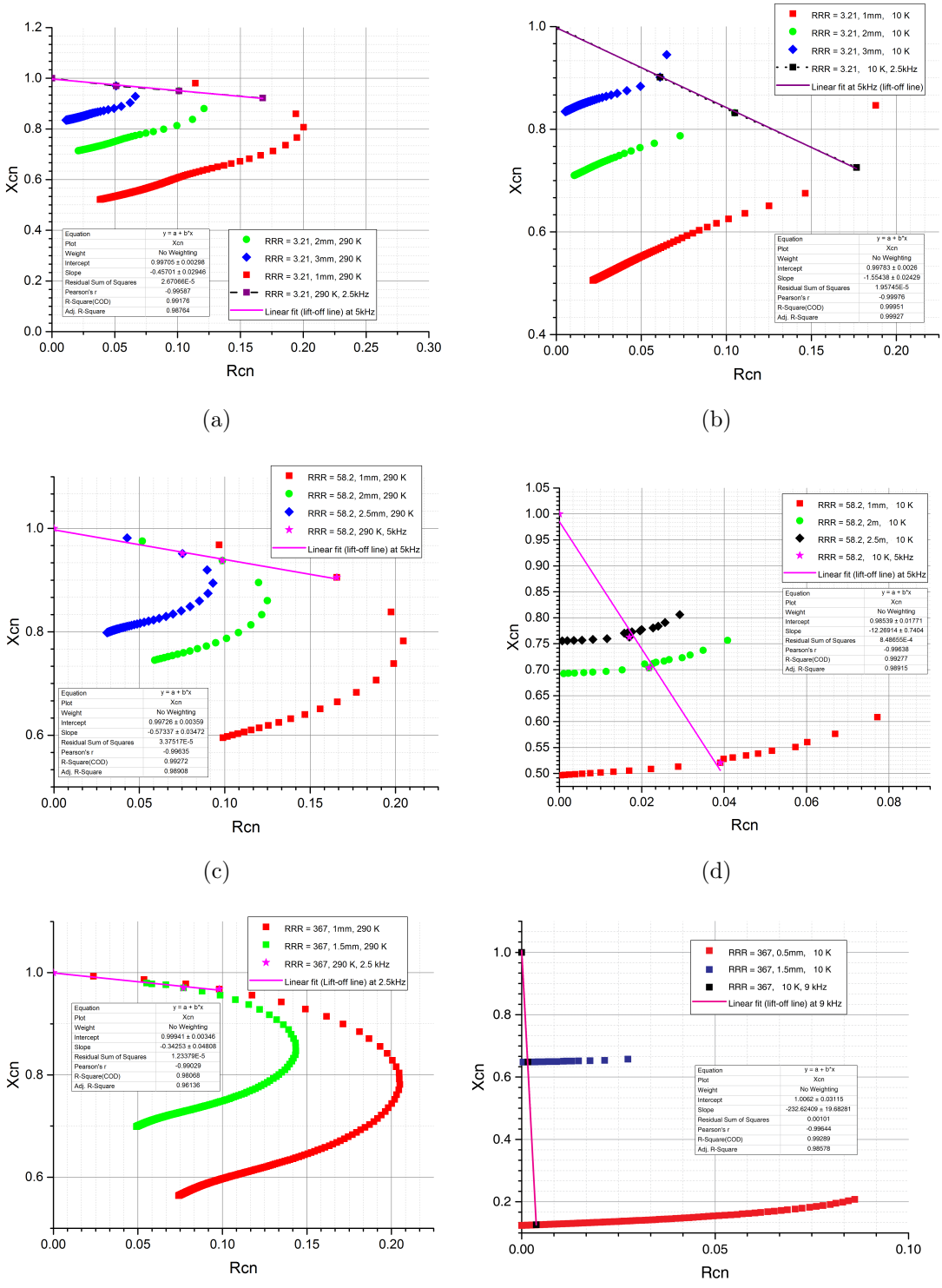

(a) (b)

(c) (d)

(e) (f)

Figure 4.12: Normalized impedance plots for different RRR samples at different temperatures along with lift-off lines at specific frequency.

Figure 4.12 (a) & (b) shows the Normalized impedance plots for RRR = 3.21 with lift-off line plotted at 2.5 kHz for 290 K and 10 K respectively. Similarly figure 4.12 (c) & (d) shows the Normalized impedance plots for RRR = 58.2 with lift-off line plotted at 5 kHz for 290 K and 10 K respectively and figure 4.12 (e) & (f) shows the Normalized impedance plots for RRR = 367 with lift-off line plotted for 2.5 kHz at 290 K and 10 K respectively. It can also be seen from the normalized impedance plots that the slopes of the lift-off line for a specific frequency increases as the conductivity increases as seen from the experimental data shown in figure 4.12. Once the normalized impedance plots for all the samples were obtained, a plot of cotθ vs. $\frac{r}{\delta}$ was generated. This requires the generation of cotθ values at different frequencies. Two representative plot showing the different lift-off lines for the same sample (here RRR = 3.21) at two different temperatures are shown in figure 4.13

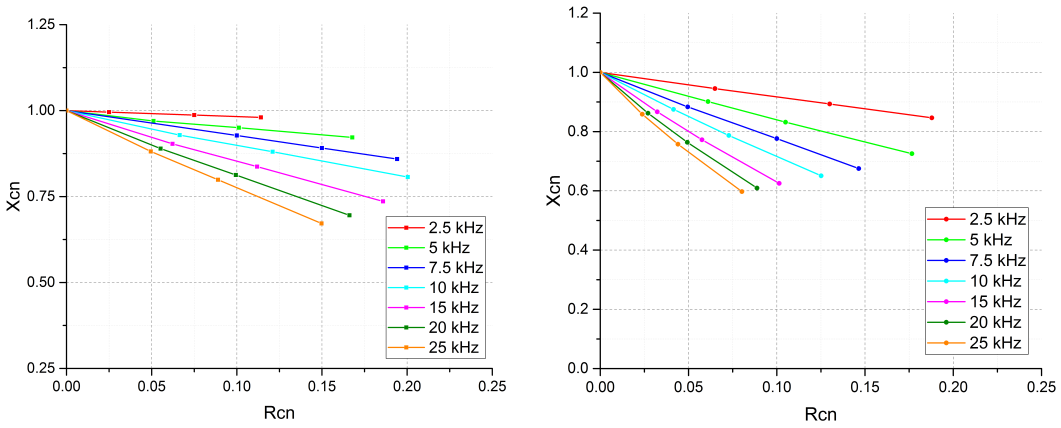

Figure 4.13: Normalized impedance plot showing (a) different lift-off lines at different frequencies for RRR = 3.21 for 290 K (b) different lift-off lines at different frequencies for RRR = 3.21 for 10 K

From the slopes of each of the lift-off lines for all the three reference samples, the cotθ vs. $\frac{r}{\delta}$ were plotted and as shown in figure 4.14 for two different temperature. A least square regression linear fit was done on the data for both 290 K and 10 K as can be seen from figure 4.14. The coefficients of the linear fit are the a and

b parameters for the respective temperatures. It should be noted that materials with very high RRR require measurements using very low frequencies. Otherwise the entire magnetic field gets reflected and the eddy currents do not penetrate into the sample at all. This also means that the plot for cotθ vs. $\frac{r}{\delta}$ at 10 K will be linear only for a limited range of low frequency values. Hence, may not be able to select the slopes of the lift-off lines at same frequency for both the temperatures. Since the equation 4.15 has frequency terms at both the temperatures, effort should be made to select the appropriate frequencies to avoid errors in measurement at lower temperatures.

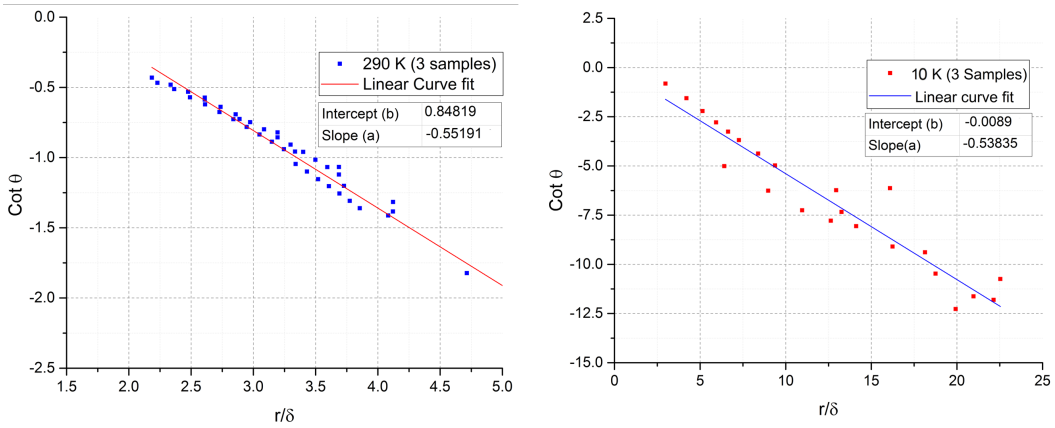

(a) (b)

Figure 4.14: Linear fit for (a) Cotθ vs r/δ curves for 3 sample with different RRR at 290 K (b) Cotθ vs r/δ curves for 3 sample with different RRR at 10 K

Determining the unknown RRR value

A similar procedure to the one used for determining the a and b parameter is used to measure the RRR and electrical conductivity. The normalized impedance plots for the sample at two temperatures are determined and are given in figure 4.15. An appropriate low frequency was selected and the slopes of the lift-off line (cotθ) at that frequency was determined. The cotθ values along with the a and b values determined from the previous step were fed back into the equations 4.14 and 4.15

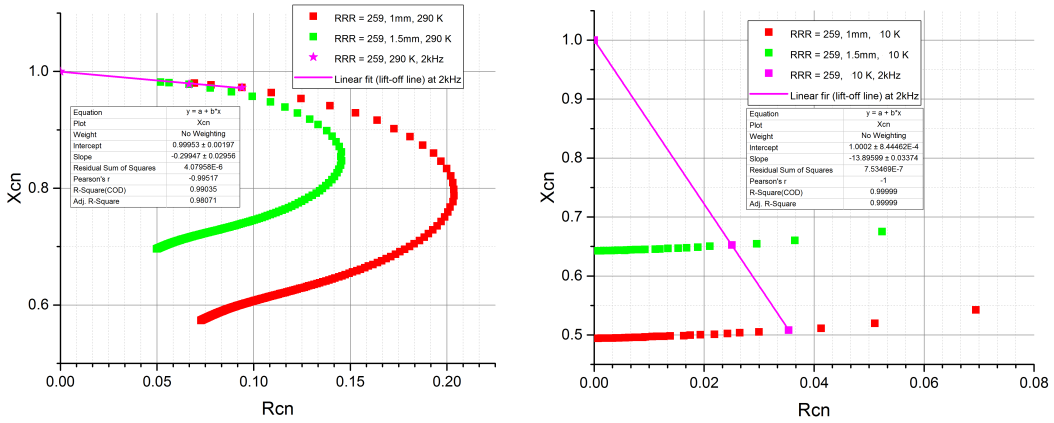

(a) (b)

Figure 4.15: Normalized impedance plot for (a) unknown sample at 290 K and lift-off at 2 kHz (b) unknown sample at ∼10 K and lift-off at 2 kHz

to determine the RRR and electrical conductivity of the unknown sample at both the temperatures. Table 4.1 shows the calculated value for the unknown sample along with the errors with respect to the 4-probe method.

Table 4.1: RRR value and conductivity calculated for unknown sample

T (K)	f (kHz)	a	b	cotθ	σ (S/m)	Measured σ (S/m)	% error in σ	RRR calculated	RRR measured	% error
10	1.5	-0.5383	-0.0089	-11.805	1.52E+09	1.55E+09	1.75	255.3	259	1.42
290	7.5	-0.5519	0.8482	-0.8354	5.95E+06	5.96E+06	0.146			

Here, three samples having RRR 3.21, 58.2 and 367 were used to determine the a and b parameters for the sensor. These parameters are mainly dependent on the coil geometry and temperature. This means that a single sample can be used to calibrate the sensor, but the accuracy of measurement will be reduced. The $\frac{r}{\delta}$ was intentionally limited to a certain range for all the samples, to reduce the non-linearities due to the surface defects and fringing effects of the sensor. Cotθ follows a fairly linear trend at 290 K and at 10 K as seen from figure 4.14. The values of a = -0.5519 and b = 0.8482 at 290 K and a = -0.5383 and b = -0.0089 at 10 K, were then used to determine the conductivity and RRR of the unknown sample.

It should be noted that RRR values $\gg$ 400 can also be measured using the same technique by reducing the operating frequency below 1 kHz so as to limit the skin effect and therefore, allowing for much deeper penetration of the currents. More

samples will be tested and nonlinear effects will be studied in detail at a later point of time. The increase in errors at 10 K and lower temperatures could be associated with the lead compensations, that was employed in the measurement techniques. Since the fixture impedance varies drastically with temperature and the fixture compensations were only done at room temperature, the errors associated with the measurement also increases at lower temperatures.

4.4.4 Conclusion from method 1 for RRR measurement

A technique for measuring RRR and conductivity of Nb using planar multilayer inductor was tested for a sample of unknown RRR. The method was verified with existing RRR measurement technique. Sensor parameters (a and b) were determined using samples of known RRR. Percentage errors of less than 1.5% at 10 K and less than 0.5% at 290 K were achieved for the electrical conductivity measurement. Higher errors at lower temperature maybe due to the fixture compensation not being done at all temperatures. It was also noted that the $\cot\theta$ vs. $\frac{r}{\delta}$ has linear relationship for lower values of $\frac{r}{\delta}$. For very large $\frac{r}{\delta}$ values, a linear approximation is not applicable. The same principles can be used to measure the electrical conductivity of other metals also as shown in appendix A.

4.5 Method 2: RRR measurement using inflection point

The method discussed in the previous section is highly data intensive. The process to calculate the electrical conductivity and RRR involves many steps with a large number of data sets at many different frequencies and lift-offs. A less data intensive method was therefore required for quick estimation of RRR of Nb, which would be more suited for a production line environment in SRF cavity fabrication. One such method would be to use the relationship between eddy current penetration depth (δ), the electrical conductivity (σ) the frequency of excitation (f) and the series inductance term (L_s) of the impedance of the sensing coil.

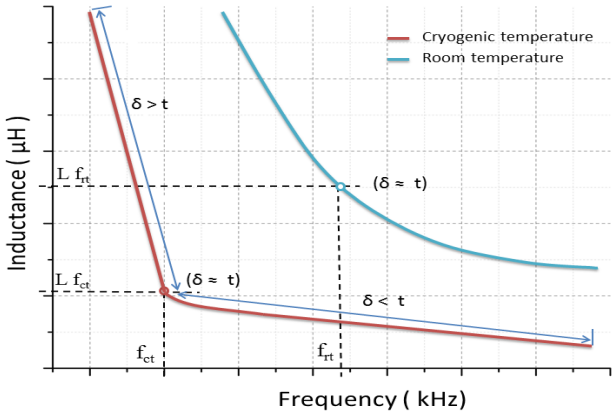

Figure 4.16: Operating principle for inflection point method of sensing

4.5.1 Principle of sensing

It has been well established [48, 80] that the series inductance part of the impedance is a function of the frequency of operation. When electromagnetic waves fall on a metal, the amplitudes of electric and magnetic fields decrease exponentially with depth from the surface as seen from the solution of Maxwell's equations for conducting medium. The skin depth δ depends upon the conductivity of metal and frequency of the electromagnetic wave and also on magnetic permeability of the metal as can be seen from equation 4.12. If thickness of the metal is much less than the skin depth at the operating frequency of electromagnetic waves, the waves will pass through the metal. Also, the penetration depth (δ) to which the eddy currents induced in the sample penetrates decides to what extent the inductance of the excitation coil gets modified.

$$\delta = \frac{1}{\sqrt{(\mu_0 \pi \sigma f)}}$$

This would mean that under the influence of a conductor, L_s becomes a function of δ, keeping everything else constant. Consider a sample of specific thickness t which is kept under the sensing coil. Assume that the coil inductance is measured from a very low frequency to very high frequency using an impedance analyzer. Three regions of operations will be there as the frequency is swept from a very low frequency to a very high frequency as shown in figure 4.16.

Region 1 ($\delta \gg$ t): In this region, the coil impedance is completely insensitive

to the material properties of the target and the frequency is so low that the electromagnetic waves are completely transparent to the metal target. Whenever a sensor is designed to probe a target, care should be taken to select the frequency such that the skin depth should be within the thickness of the target. Here, L_s will be a function of frequency but is independent of the material properties of the target.

Region 2 (δ = t): At this point, there will be a change of slope on the L_s(f) plot. This means that there should be an inflection point that depends only on the thickness and the conductivity of the target. Below this point, the L_s(f) plot becomes a function of the material properties of the target (σ).

Region 3 ($\delta \ll$ t): At this point, L_s(f) plot saturates to a constant value. Here, the frequency is so high that the electromagnetic waves are getting reflected from the surface. Further increase in the frequency will not change the series inductance by any appreciable value.

Assuming that the thickness of the target remains constant (this assumption is an approximation), the series inductance (L_s) will have an inflection point when $\delta \simeq$ t.

$$\delta_{290K}(\simeq t) = \frac{1}{\sqrt{(\pi \mu \sigma_{RT} f_{RT})}} \tag{4.16}$$

$$\delta_{10K}(\simeq t) = \frac{1}{\sqrt{(\pi \mu \sigma_{CT} f_{CT})}} \tag{4.17}$$

Here, f_{RT} and f_{CT} are the inflection frequencies at room temperature and cryogenic temperature (10 K). Assuming change in t is negligible, we can deduce from equations 4.16 and 4.17 that,

$$\frac{f_{RT}}{f_{CT}} = \frac{\sigma_{CT}}{\sigma_{RT}} = RRR \tag{4.18}$$

From equation 4.18, it becomes clear that we only need to find the inflection point at 290 K and 10 K from the plot of L_s vs. frequency. This can be easily done by making a MATLAB script that looks for a changing slope along the L_s vs. frequency curve.

4.5.2 Experimental results

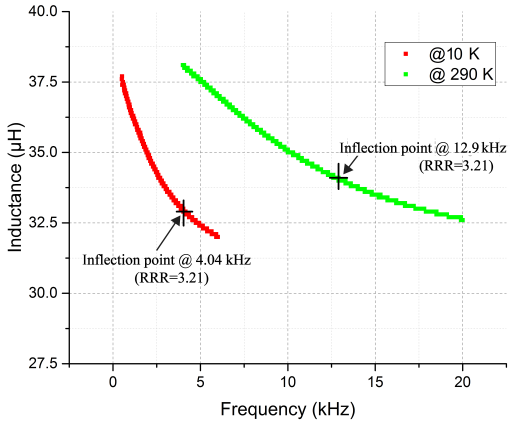

(a)

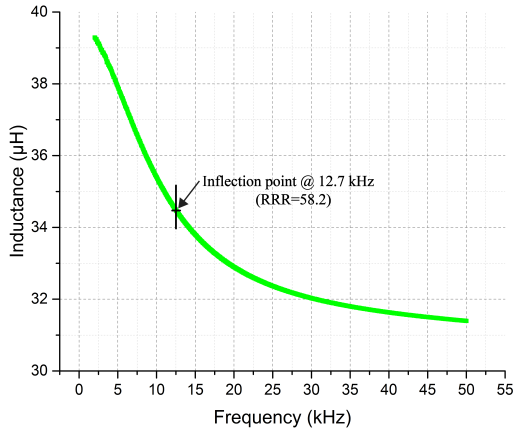

(b)

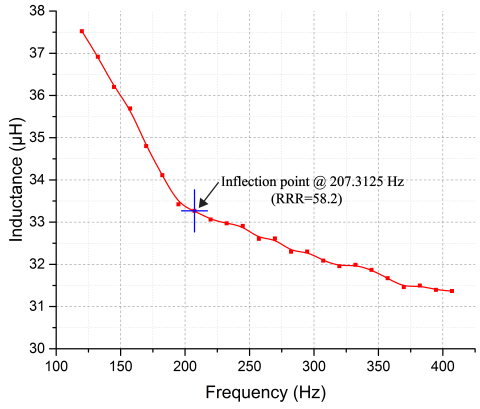

(c)

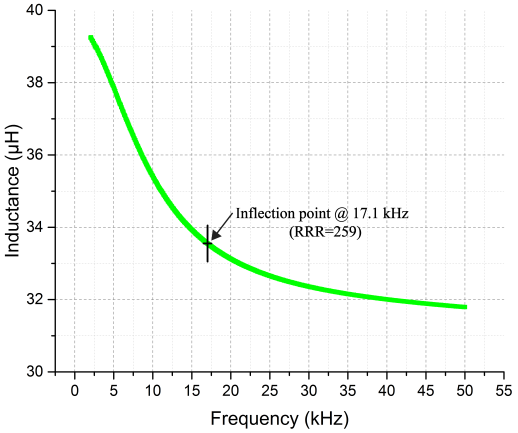

(d)

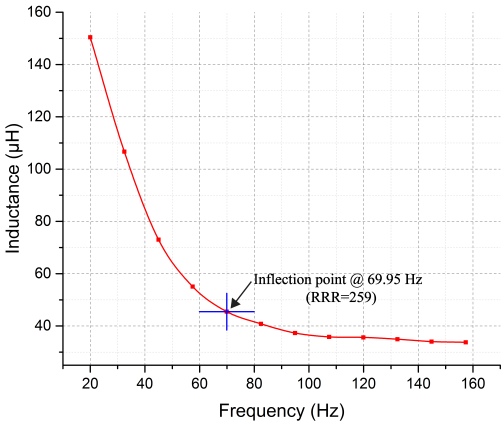

(e)

Figure 4.17: Inductance plot (L_s) of (a) RRR = 3.21 sample with inflection point at 12.9 kHz at 290 K and 4.04 kHz at 10 K (b)&(c) RRR = 58.2 sample with inflection point at 12.7 kHz at 290 K and 201.31 Hz at 10 K (d)&(e) RRR = 259 sample with inflection point at 17.1 kHz at 290 K and 69.95 Hz at 10 K

Table 4.2: Summary of experimental result

Measured RRR	Thickness (mm)	Temperature (K)	Inflection point frequency	Calculated RRR	Percentage error
3.21	1.92	10	12.9 kHz	3.19	0.623 %
		290	4.04 kHz		
58.2	1.42	10	207.31 Hz	61.26	5.32 %
		290	12.7 kHz		
259	1.51	10	69.95 kHz	244.46	5.61 %
		290	17.1 kHz		

Experimental setup and DAQ are exactly the same as described in the previous section (figure 4.8). The sensor along with the target in the sample holder was mounted at a specified distance (1 mm for the current set of experiments) and the impedance plots (L_s and R_s) were logged at 290 K and at 10 K. The L_s plot was then fed to a MATLAB program that outputs the frequency value corresponding to the inflection points in the graph.

It should be noted that there were multiple inflection points when the measurement was made at room temperature as the cure is very smooth and continuous with many points of change of slope. A better guess of the inflection point at room temperature; can be obtained by taking into account the thickness and conductivity values of the sample, which can be measured accurately. The inflection point at 10 K was much easier to determine as there was a clear change of slope when the electromagnetic waves were confined completely in the high electrically conducting sample.

If all the samples had the same thickness and same conductivity at room temperature, all the inflection points would coincide. This was not the case as all the samples had different thickness (1.96 mm for RRR = 3.21, 1.42 mm for RRR = 58.2 and 1.50 mm for RRR = 259). From the figure 4.17 (a), it can be noted that the electrical conductivities at 290 K are also different for each of them. The calculated values of RRR using equation 4.18 are summarized in the table 4.2.

The errors associated with the measurement can mainly arise due to two reasons- (1) The basic assumption that thickness remains constant is not valid especially when the target is cooled to 10 K and (2) The resolution in frequency sweeping. This becomes important when sensing very high RRR values. As the RRR increases, the conductivity at 10 K also becomes very high. This means that a large number of data points at the lower frequency have to be obtained to accurately generate the inflection point and to obtained the RRR values. This might not be possible as the impedance analyzer has difficulty in resolving closer frequencies

than when points are spread over a larger frequency range.
Extending the point 2 of the limitations, it becomes very difficult to measure the RRR using this technique for samples of thickness higher than 1.5 mm and RRR > 300 because the inflection point would lie in frequency region less than 20 Hz. This would be impossible to measure using an impedance analyzer. The only way to overcome this is to have samples of small thickness (less than 100 μm) to effectively obtain the inflection point at 10 K. Hence this method can be very effective for thin films.

4.5.3 Conclusion from method 2 for RRR measurement

Inflection point method to determine the RRR was tested with 3 different samples of RRR values 3.21, 58.2 and 259. A MATLAB program was also developed which determined the inflection points from the L_s vs. frequency curves data. The method is less data intensive than the the previous method as it requires lesser data processing steps (No need for normalized impedance plots and lift-off plots). The method was unable to measure the sample with RRR value of 367 due to its thickness (1.5 mm) and very high electrical conductivity at 10 K. This resulted in the inflection point being below 20 Hz which is beyond the range the impedance analyzer. The method also has the limitation that the shrinking of the sample due to lowering of temperature was assumed to be negligible and this might add additional errors at 10 K measurements. Correction factors can be added incorporating the coefficient of thermal expansion of the Nb samples.

4.6 Method 3: RRR measurement using cold electronic LC oscillator

The previous two methods had the limitation that the measurement of RRR required the use of an expensive impedance analyzer operating at room temperature and the errors as a result of long lead wires over the entire temperature range. An on-chip solution for determining the RRR with relatively good accuracy was needed, especially for a production line testing of SRF cavities. A method that used a calibration technique was developed which utilizes a multiplexed inductor array based cold electronics LC oscillator to convert the series inductance change

to frequency change to address the above requirement.

4.6.1 Principle of operation

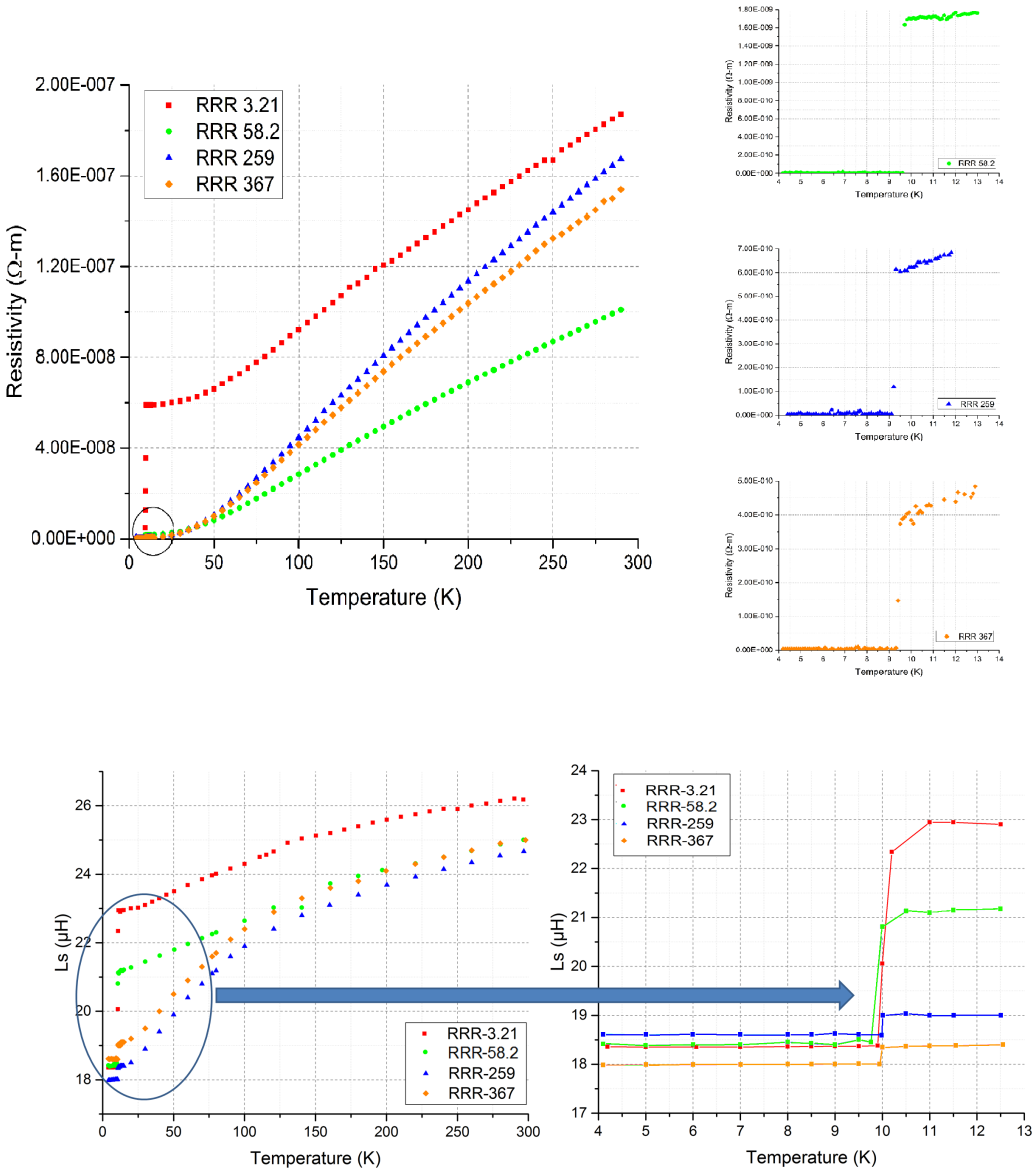

Figure 4.18: Correlation between series inductance variation and electrical conductivity (a) Resistivity variation with temperature for all 4 samples (b) Inductance variation with temperature for all 4 samples

A direct correlation is observed between the inductance and correspond resistance variations with temperature for different values of RRR as shown in figure 4.18. The inductance also have similar variation in electrical conductivity but, there are other non-linearities arising due to the structural deformations that may be affecting the sensor.

It should also be noted that the values of inductances at 10 K behave in a very similar way to the conductivity of the Nb sample at 10 K.

This means that (L_s(RRR = 3.21 at 10 K) > L_s(RRR = 58.2 at 10 K) > L_s(RRR = 259 at 10 K) > L_s(RRR = 367 at 10 K) in a similar way to ρ_s(RRR = 3.21 at 10 K) > ρ_s(RRR = 58.2 at 10 K) > ρ_s(RRR = 259 at 10 K) > ρ_s(RRR = 367 at 10 K). If a method could be developed that may convert the changes in series inductance to corresponding frequency changes at cryogenic temperatures, then the RRR can be calibrated from the ratio of the frequencies.

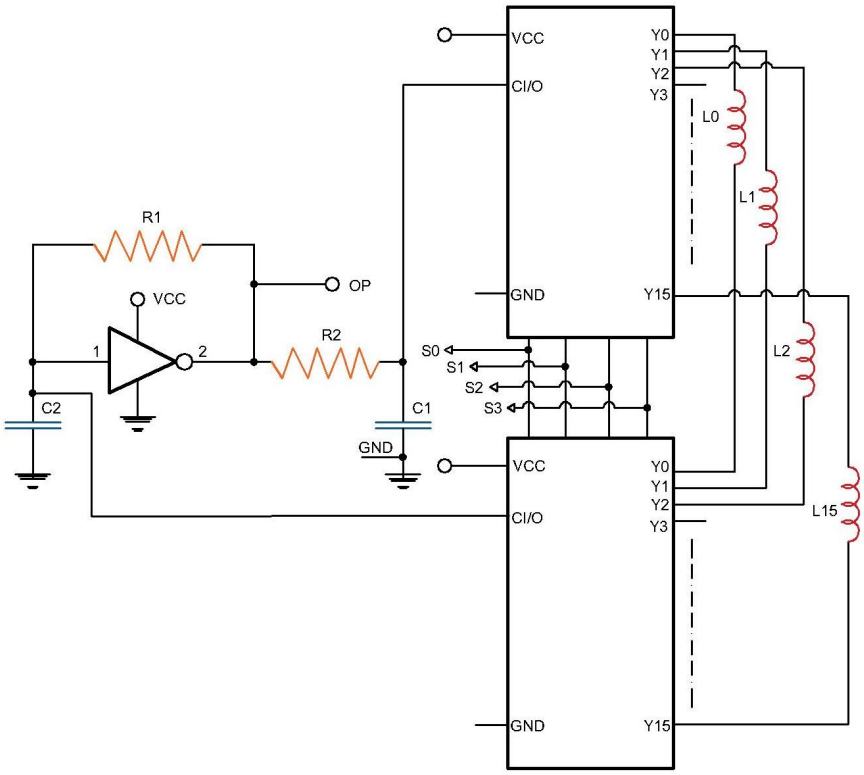

Figure 4.19: Multiplexed Inductor based LC oscillator circuit capable of operating at 4.2 K

4.6.2 Experimental setup and measurement procedure

Cold electronics based LC oscillator circuit

A detailed description of the signal conversion circuit shown in figure 4.19, is provided in chapter 3. Here also, the same four inductor array was used as the sensing element. Three of them can be used for sampling the targets and the fourth one works as the reference sensor to compensate the effects of temperature on the sensing elements. Another advantage of using a multiplexing circuit to switch between the different sensing inductor is use of a single inverter based oscillator circuit. This eliminates the component based errors associated with each circuit that may generate added complexity in measurement. This would require also restrict the use of multiple output pins (limited resource for a cryostat) to take out the frequency output from cryogenic environment to the ambiance.

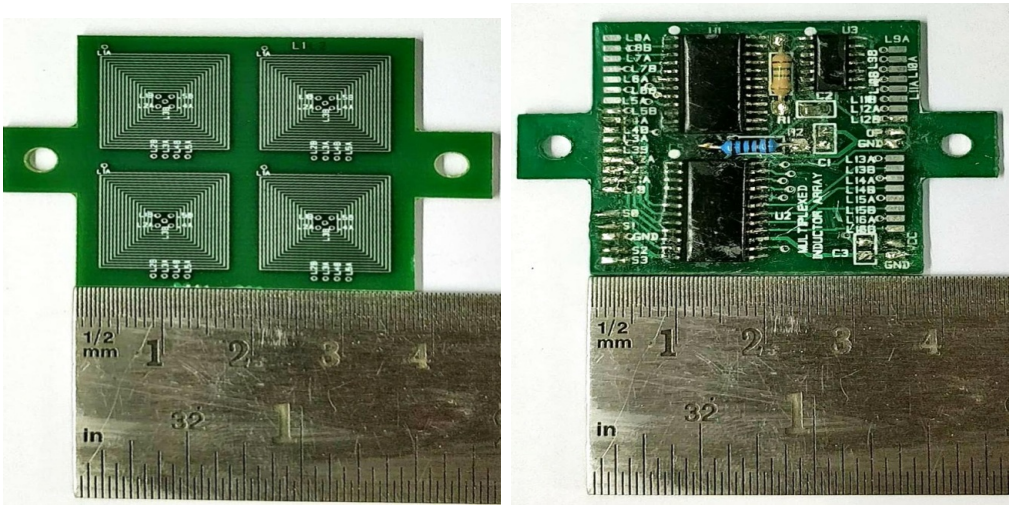

Figure 4.20: Photograph showing (a) Sensing element having four-inductor array each having five layers (b) Cold electronics based Multiplexed inductor LC oscillator signal conditioning element

The detailed methods involved in designing the inductor array for the sensing elements have also been described in chapter 3. The photograph of the senor along with the cold electronics is shown in figure 4.20.

DAQ developed for multiplexed inductor sensing element

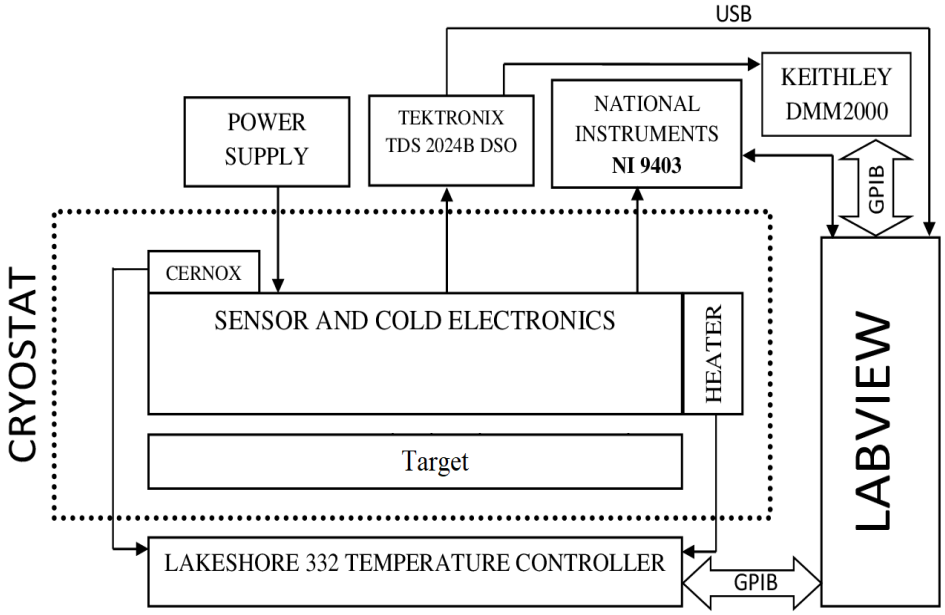

Figure 4.21: Schematic of DAQ developed for acquiring the frequency values from all the four inductors.

The DAQ system that was used for the experiment, was also very similar to the one used for angular displacement measurement described in chapter 3. Here, a switching signal was generated by the LABVIEW program and interfaced through the NI 9403 digital output module. The frequency from each of the inductor was measured using Keithley 2000 Digital Multi Meter (DMM). The temperature data was acquired using Lakeshore 332 temperature controller along with Cernox temperature sensor. The temperature in the cryostat was maintained at a desired value by a 25Ω heater in conjugation with the temperature controller and the Cernox data. The entire data was stored in an excel file. The schematic of the measurement setup is shown in figure 4.21

4.6.3 Experimental results

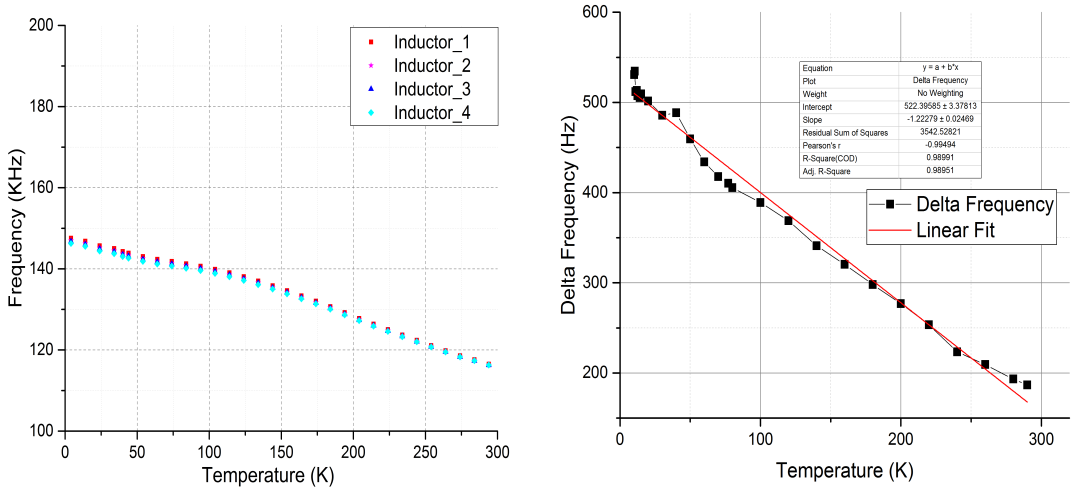

(a) (b)

Figure 4.22: (a) Variation of output frequency from a single inductor with temperature (b) variation of delta frequency (δf) = f(L_x)- f(L_r)

Initial experiments were carried out to determine how the sensor would behave for temperature reduction from 300 K to 4.2 K. This was required to validate the reliable operation of the circuit down to 4.2 K and also to ascertain the output from the four inductors as shown in figure 4.22 (a). It can also be seen that all the four coils produce outputs (frequencies) that are identical with minor deviations that were associated with the individual sensing coils. Figure 4.22 (b) shows the change of delta frequency (δf) as a function of temperature when the sensor was cooled to 4.2 K. It can be seen that even though the sensor output changes from 115 kHz to 145 kHz, the δf only changes by 320 Hz. This means that the term δf was able to cancel out most of temperature effects that were common to all the sensors. This also indicate that δf should be a good sensor parameter to measure the change in electrical conductivity of the target.

Once the sensor parameters had been established without the presence of the target, experiments were done by keeping targets (3 at a time if needed in the current setup).

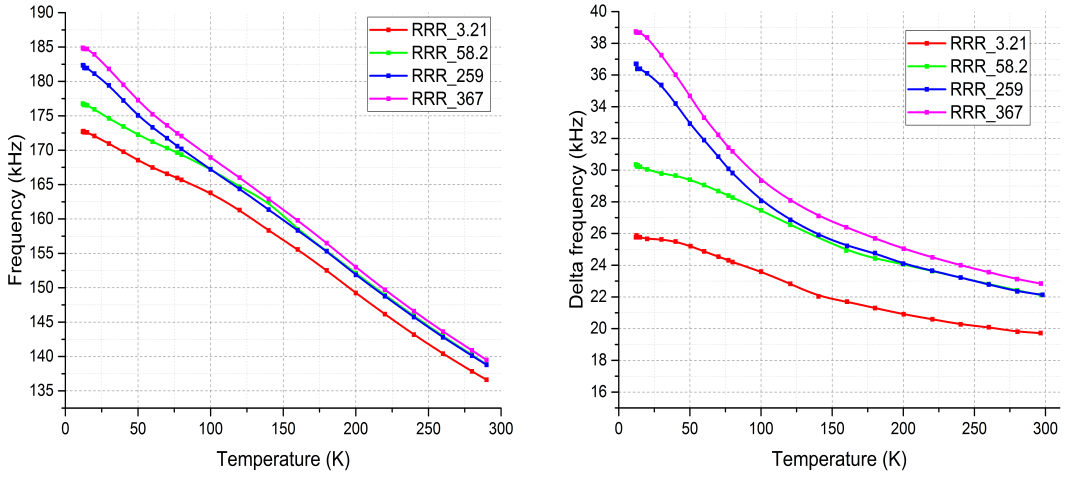

(a) (b)

Figure 4.23: (a) Variation of output from the multiplexed LC oscillator for all 4 samples (b) variation of delta frequency (δf) = f(L_x)- f(L_r) for all 4 samples

The output frequency for the sensor under the influence of Nb target having four different values are shown in figure 4.23 (a). It can be seen that the output has a response that correlates very closely with the inductance variations. As a result, the sensor attains a peak value of frequency when the RRR of the sample was very high and the lowest peak value when the RRR was low. A direct correlation between the frequency and conductivity was not always possible as the oscillator also has a small frequency shift due to the change in the series resistance of the coil. The δf plot shown in figure 4.23 (b) indicates that the ratio of the delta frequency should be a function of the RRR of the sample. It can also be observed that the δf frequency varies by about 20 kHz when the sensor along with the target was cooled and only by about 320 Hz when it was away from the target.

Table 4.3: Summery of results using method 3

4-probe method RRR	**Cold electronics method RRR**	**Percentage error**
259	285	+10.3 %
367	346	-5.6 %

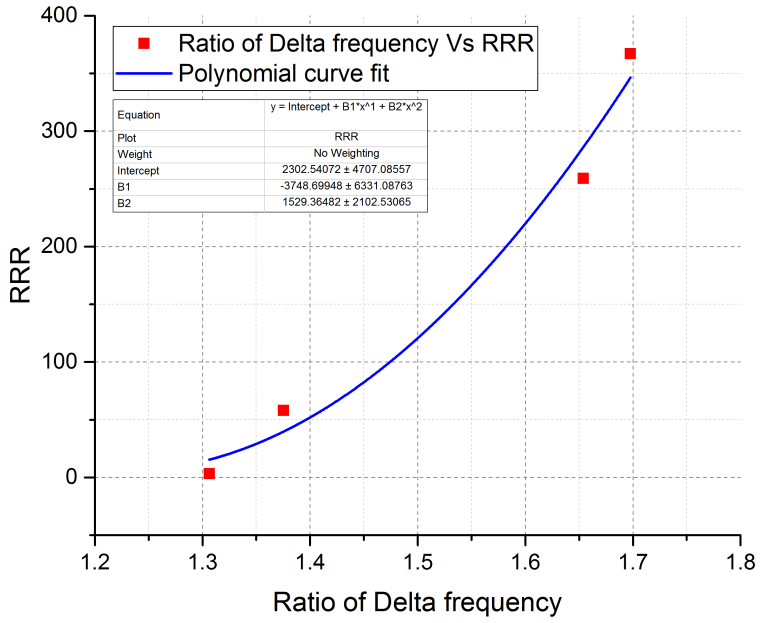

Figure 4.24: 2nd order regression curve fit for ratio of δf against the RRR values

A second order regression fit was done with the four sample data and the curve fit was used to determine the RRR values of the samples. It should be understood that the calibration curve fit will be a better approximation only when the number of samples are large (> 10). Due to the limitations in acquiring a large number of Nb samples with varied RRR values, the accuracy of this method could not be improved. The results are summarized in table 4.3.
The main advantage of this technique is that the senor does not require any additional expensive equipments like an impedance analyzer or lock in amplifier. A basic logic gate based counter can be used to accurately measure the output frequency with a good degree of accuracy. The switching scheme can also be implemented by a basic ring counter circuit. The only drawback of this technique is the need for more data points to accurately calibrate the sensor.

4.6.4 Conclusion from method 3 for RRR measurement

A RRR measurement method based on the series inductance change of the sensing coil was designed and tested. The sensing method was found to be easier to use in a production line environment for SRF cavities as it only requires the sensor

along with the electronics to be mounted inside the cryostat. The δf term was also found to be largely independent of the physical parameters of the sensing coil and depends only on the properties of the target. Using δf as the sensing parameter and the four samples of different RRR, a second order cure fit was done and can be used to measure the RRR of an unknown sample.

4.7 Conclusion

A detailed analysis of eddy current sensor, its principle of operation and use for cryogenic RRR measurement of a superconductor samples was presented in this chapter. This chapter introduced the concepts of normalized impedance plane and analysis for eddy current sensing. RRR measurement requirement in the field of accelerators were also discussed. A reference for measuring the RRR was generated using the 4-probe electrical resistivity measurement technique. Using the method as standard, three different non-contact type AC measurement techniques for measuring the RRR were developed.

The first method used the basic principles of eddy current measurement extended to cryogenic temperatures. The sensor parameters (a and b) were determined by calibrating the sensor using three samples of different RRR values. Once the parameters were determined, the RRR of an unknown sample was calculated and found to match with the standard measured using the 4-probe method. The errors in the measurement and methods to reduce these errors were discussed in detail.

The second method utilized the change in slope of L_s vs. frequency curve when the eddy current skin depth becomes equal to the thickness of the target, to measure the RRR of the sample. A MATLAB program to determine the inflection points from the L_s vs. frequency was also developed. From the value of the frequency at these inflection points, RRR can be estimated. It was found that determining the inflection point at the room temperature was difficult due the gradual change of slope over average of frequencies as shown in the plot, but had very clear inflection points at cryogenic temperature. Inflection point at room temperature could be estimated accurately by measuring the electrical conductivity and thickness of the sample. The method has the limitation for samples with high RRR values and large sample thickness as the inflection point would lie in very low frequency ($<$20 Hz) region.

The third method used the correlation between the resistivity change and the change in the inductance value of the senor. The cold electronics signal conditioning circuit to convert the inductance change to frequency change was developed for measuring the RRR of the samples. It was established from the experiment that the parameter δf canceled the temperature effects on the sensor and becomes a function of electrical conductivity. The sensor along with the electronics was tested down to 4.2 K and was found to work satisfactorily. A calibration chart of RRR vs.δf ratio was generated, using which the RRR of unknown samples can be determined. This method requires a large number of samples with wide range of RRR values to make the calibration chart accurate. It also has the advantage that, it can be made part of a fabrication line to accurately map the changes in RRR when the RF cavity is subjected to various production stages.

Chapter 5

Conclusions

5.1 Introduction

Development of sensors for cryogenic applications requires a detailed knowledge on various fields of science and engineering. The specific class of cryogenic sensors, namely eddy current sensors have been in low profile mainly due to a few inherent limitations. Eddy current sensors are shown to have numerous advantages over conventional sensors like the ease of fabrication, good sensitivity, low cost, etc. The primary objective of this thesis was to explore the possibility of using planar inductor based eddy current sensors at cryogenic temperatures. From the literature survey that was described in Chapter 1, it was concluded that minimal effort had gone into developing the eddy current sensors capable of operating down to 4.2 K mainly due to the innate limitation of the sensing principle. This implies that the impedance variation associated with a particular parameter change is also susceptible to temperature change. This means that the sensor becomes useless at cryogenic temperatures unless steps are taken to negate the effect of temperature and to calibrate specifically for cryogenic environments.

A set of three problems were chosen by taking into account few of the alternative solutions that were available in research as well as industry and planar inductor eddy current based solutions were chosen to overcome some of the critical limitations that plagued these sensors. Robotics and automation at cryogenic temperatures are becoming significant day by day with the advent of Mars rovers and space robotics. Most of these research areas require precise position tracking

(accurate to the micrometre scale) and work through an intermediate medium viz. glass or Kevlar. The current technologies that tackle this problem are largely based on potentiometric principles or optical sensors; as these are least affected by temperature variations. They all suffer from a major limitation of not working with an opaque intermediate medium. A planar inductor based position sensor was developed to overcome this limitation. As there was limited study available on designing PCB based sensors for cryogenic temperature, a detailed analysis was required to ascertain how an inductor based sensing element would perform under the cryogenic conditions. Parametric optimization of the sensing coils also had to be done. Another major drawback of eddy current sensors was that the electronics were usually kept at ambiance and at a distance from the sensing element that causes additional errors due to temperature gradients along the coupling line. To avoid this, a cold electronics based signal processing element was designed to convert the inductance change into a frequency variation. Various tests at cryogenic conditions had been carried out to select the components that would work at 4.2 K reliably. A testing setup and DAQ were developed to calibrate the sensor and determine the key parameters.

Another sensor that was required in space robotic applications is an angular rotation sensor (angular displacement). The currently available sensor uses a complex coil system and closed magnetic path principle to measure the angular displacement at 4.2 K. A modification of the previously developed displacement sensor can be used to measure the angular displacement as well. The developed sensor had a 2×2 array of coils as the sensing element and two multiplexer (MUX) ICs to switch among the four coils. Each of the coils becomes part of an LC oscillator when that is selected by the switching signal. A rotor segment was developed using etched PCB with a small copper sector that was made to rotate above the sensing element. When the sector comes under the influence of any one of the coils, the output frequency associated with that coil increases. The frequency will also be a function of the overlapped area of the sector with respect to the coil. The LC oscillator along with multiplexed inductors were characterized down to 4.2 K. The size of the rotor segment was also optimized to minimize the dead zones in sensing. A complete testing setup along with DAQ were developed and the sensor was calibrated against fixed steps in angular displacement.

The third problem tackled the issue of measurement of the RRR of an SRF cavity

as it is subjected to different stages of fabrication. Each fabrication step might alter the RRR of the cavity and therefore, an easy non-contact, non-destructive way of determining the RRR would improve the overall performance of the finished cavity. In view of this, planar inductor based eddy current methods for conductivity measurements were explored and eddy current principles of measurements were extended to cryogenic temperatures. Three approaches were explored each with their own advantages and disadvantages, all using planar inductor based sensing element for measurement.In the first method, the basic eddy current principle of impedance variation (L_s and R_s) was used and the normalized impedance plots at both the temperatures were constructed. The slope of the lift-off line is a function of the conductivity of the sample. The sensor was calibrated using samples of known RRR and the sensor parameters were determined. Once the parameters were established, the unknown RRR was obtained by knowing the change of slopes from the normalized impedance plots.

The second method used the eddy current penetration depth and its influence on the series inductance of the sensing element. It was shown that the plot of L_s vs. frequency has an inflection point, when the eddy current penetration depth equals thickness of the sample. This frequency is a function of the conductivity of the sample at the measured temperature. By determining the inflection point at both the temperatures, the RRR could be calculated by taking the ratio of the frequency. This method required less data analysis compared to the previous method but the use of the impedance analyzer and its related complications and the drawbacks.

The third method used the multiplexed LC oscillator circuit to convert the inductance changes to associated frequency changes and used the correlation between the frequency of output to the absolute change in resistivity of the target. By using a reference coil under the same temperature conditions but in absence of the target and taking the difference in frequency outputs, all effects on the sensing element that are common to all the four coils were canceled out. This difference in frequency (δf) was used as the parameter to measure the RRR of the sample. This method required comparatively less complex measurement instrumentation and a basic frequency counter or a multimeter can be used to accurately measure the RRR of the Nb sample.

Initial sections of this chapter dealt with the basic conclusions that were obtained

from the thesis considering the objectives that were mentioned in the introduction. The empirical findings that were discovered in the process of developing the sensors are also discussed. The implications of these studies along with the future scope of work are also reported. The final section deals with the concluding remarks about the thesis.

5.2 Outcome of studies

5.2.1 Planar inductor based position sensor for 4.2 K operation

- A planar inductor eddy current based proximity sensor was developed to operate down to 4.2 K.
- Design of sensing coil was carried out using Ansoft Maxwell software and its structural and thermal analysis were carried out using ANSYS software.
- An LC oscillator based signal processing circuit was designed using specifically selected and tested components and the performance of the circuit was analyzed to 4.2 K.
- A custom DAQ with experimental setup was developed to characterize and calibrate the sensor down to 4.2 K.
- The sensor was found to have a resolution of 40 μm in the range of 0.85 mm to 1.5 mm with an accuracy of $\pm$ 2μm and sensitivity of 14.77 μm/kHz.
- An Indian patent (IN Patent R20,164,035,984) was filed for the same.
- A paper was published in Senors and Actuators: A Physical, an international journal.

5.2.2 Multilayer planar inductor array based cryogenic angular position sensor

- A cryogenic angular position sensor based on multilayer planar inductor array was developed and tested at 4.2 K.

- Ansoft Maxwell software tool was used to show the variation of inductance when overlapping conducting area changes.
- A multiplexed LC oscillator based signal processing circuit was designed using selected and tested components and the performance of the circuit was analyzed down to 4.2 K.
- A LabVIEW based DAQ capable of switching different inductors and acquiring the corresponding output frequencies.
- Rotor segment sizes were optimized to minimize the dead zone associated with sensing angles and an appropriate segment size was selected.
- A 24 point calibration of the rotation sensor was done for the entire temperature range down to 4.2 K.
- The sensor was found to have an accuracy of ±2 °(at 77 K) and sensitivity of 407 Hz/°(at 77 K). Further improvements are possible with higher operating frequencies.
- A paper was published in Cryogenics, an international journal.

5.2.3 Planar inductor eddy current RRR measurement of Nb

Dual slope method for measuring RRR

- Impedance change associated with a coil in the presence of a conductor was used to measure the electrical conductivity of the target.
- Impedance changes were transformed into normalized impedance plane and the lift-off lines were determined for many different frequencies.
- Using standard samples of known RRR (using 4-probe measurement), the coil and temperature dependent parameters were determined at 290 K and 10 K.
- Lift-off lines for the unknown sample was also generated from the impedance measurement of the coil at the specified temperatures.

- From the slope of the lift-off lines at two temperatures, electrical conductivities as well as RRR were determined.
- The RRR of the unknown sample was measured with an accuracy of 1.42%
- This method for measuring RRR was data intensive and required expensive instruments like an impedance analyzer and associated complications.
- A paper was published in Instrumentation, an international journal.

Inflection point method for measuring RRR

- The relation between the eddy current penetration depth and the electrical conductivity of the target was used to measure the RRR of the sample.
- The L_s vs. frequency plot has an inflection point when the penetration depth becomes equal to the thickness of the target.
- Inflection point was determined from the L_s vs. frequency plot using a MATLAB program by observing the change of slope and knowing the thickness of the sample.
- Inflection points at both the temperatures were determined and from that, the RRR was measured.
- The unknown sample's RRR was measured with an accuracy of 5.61%.
- This method was not as data intensive as the previous one but it still required expensive instruments like an impedance analyzer and associated complications.

RRR measurement using cold electronic LC oscillator circuit

- The correlation between the resistivity variation of Nb and corresponding inductance variation of the sensing coil was used to estimate the RRR of the sample.
- One coil in the inductor array was kept as reference and all other frequencies were measured with respect to the reference coils frequency.

- This made the resulting frequency difference (δf) a function of only the material properties of the target (keeping lift-off constant).
- The ratio of δf at 290 K and 10 K was used to generate a calibration chart which can be used to measure the RRR of any other Nb sample.
- Measurement accuracy can be improved by including larger number of samples for generating the calibration chart.
- Method for measuring RRR is the least data intensive and can easily be incorporated into a schematic for estimating the RRR in a production line for fabricating RF cavities.
- This method does not require any complex instrumentation to estimate the RRR.

5.3 Implications

This thesis shows that planar inductor eddy current sensors can be used for a variety of applications in cryogenic environment. This sub class of sensors have been thoroughly avoided as can be seen from the literature that is available. Planar inductor based eddy current sensors have been shown as a low cost viable alternative to many of the sensors that have been shown to work at cryogenic temperatures (down to 4.2 K and even lower). This would open up a completely new set of PCB based planar inductors sensors for applications such as robotics in harsh cryogenic environment, cryogenic engines and cryogenic suspensions. This work would also put more light into the usage of cold electronics based signal conditioning elements integrated into sensing coil to negate some of the disadvantages of eddy current sensors. It was also shown that an array of planar inductors can be used as a versatile sensing element incorporating differential measurement techniques for cryogenic temperatures. These sensors can be used to measure a number of parameters including angular positions and 2D postion tracking. The sensors described in this thesis also substantiate the point that the simple solutions can be used to overcome few of the inherent limitations of eddy current sensors.

Another major implication of this thesis is the development of non-contact, non-destructive methods for RRR measurement of Nb for SRF cavities. Till date, there have been little work attempted to incorporate the eddy current principles for measurement at cryogenic temperatures (especially for electrical conductivity measurement). Multiple approaches are possible with each method having its own advantages and limitations. These methods can be extended to include an array of sensing coils to completely map the RRR of RF cavity in each stage of fabrication. This would improve the quality of th SRF cavities and also can be very helpful in the fabrication process.

5.4 Suggestions for future research

1. A study on the variation of electrical permittivity of FR4 material has to be undertaken at cryogenic temperatures.

2. A system for 2D tracking of a target in cryogenic environment using planar inductor array can be developed.

3. Calibration for RRR measurement techniques can to be improved by experimenting with a large number of samples with different RRR values.

4. Eddy current techniques can be extended to measure the RRR of thin film coated SRF cavities.

5. A complete RRR mapping of SRF cavities can be undertaken using an array of sensing coils around the cavity.

5.5 Conclusion

This thesis shows that planar inductor based eddy current sensors can be effectively used in numerous applications at cryogenic temperatures. The work also highlights the fact that eddy current principles of non-destructive testing can be extended to cryogenic temperatures by carefully designing the sensing element and using differential methods of sensing.

Bibliography

[1] Pasquale Arpaia, Luca De Vito, M Pezzetti, Francesco Picariello, and L Serio. State of the art and challenges in measurements and transducers for cryogenic monitoring. *Measurement*, 2018.

[2] RA Cloyd. Variable reluctance proximity sensors for cryogenic valve position indication. 1982.

[3] Steven D Roach. Designing and building an eddy current position sensor. *Sensors-the Journal of Applied Sensing Technology*, 15(9):56–74, 1998.

[4] KA Backes and JG Brisson. An inductive position sensor for the measurement of large displacements at low temperature. *Review of scientific instruments*, 69(2):599–602, 1998.

[5] O Krause, U Grözinger, D Lemke, A Böhm, and R Hofferbert. Magnetoresistive position sensors for cryogenic space applications. In *9th European Space Mechanisms and Tribology Symposium*, volume 480, pages 335–338, 2001.

[6] M Milushev, M Suesser, and F Wuechner. Investigation of two different types of displacement transducers in the cryogenic environment. *Cryogenics*, 44(3): 197–201, 2004.

[7] Qipeng Li and Fan Ding. Novel displacement eddy current sensor with temperature compensation for electrohydraulic valves. *Sensors and Actuators A: Physical*, 122(1):83–87, 2005.

[8] Peng Wang, Zhibin Fu, and Tianhuai Ding. A frameless eddy current sensor for cryogenic displacement measurement. *Sensors and Actuators A: Physical*, 159(1):7–11, 2010.

[9] Srinivas Rana, Boby George, and V Jagadeesh Kumar. Self-balancing signal conditioning circuit for a novel noncontact inductive displacement sensor. *IEEE Transactions on Instrumentation and Measurement*, 66(5):985–991, 2017.

[10] Henning Irle, Norbert Kost, and Franz-Josef Schmidt. Inductive angle sensor, May 22 2001. US Patent 6,236,199.

[11] Henning Irle, Norbert Kost, and Franz-Josef Schmidt. Inductive angle sensor having coupled oscillators with similar inductive response, July 3 2001. US Patent 6,255,810.

[12] V Ferrari, A Ghisla, D Marioli, A Taroni, P Fasolato, F Maggi, S Pelloso, and V Rossetti. Capacitive angular-position sensor. In *Advanced Microsystems for Automotive Applications 2003*, pages 301–312. Springer, 2003.

[13] Guy Bach and Bernard Dockwiller. Inductive angular-position sensor, August 18 2009. US Patent 7,576,533.

[14] Alain Carapelle, Nicolas Martin, and Thierry Chantraine. Precise through wall angular position sensor compatible with cryogenic temperature for space launcher. *Sensor Letters*, 11(10):1992–1995, 2013.

[15] Qifu Tang, Donglin Peng, Liang Wu, and Xihou Chen. An inductive angular displacement sensor based on planar coil and contrate rotor. *IEEE Sensors Journal*, 15(7):3947–3954, 2015.

[16] Ling-Ling Gong, Wan Chen, Wen Kang, Shu-Chen Sun, Zhi-Qiang Li, Lei Zhang, Yu-Feng Yang, Hui-Hua Lu, Xiao-Yu Li, Shu-Tao Zhao, et al. Hall sensor angle error and relative position calibrations for cryogenic permanent magnet undulator of high energy photon source test facility (heps-tf). *Radiation Detection Technology and Methods*, 1(2):17, 2017.

[17] RK Kirschman. Cold electronics: an overview. *Cryogenics*, 25(3):115–122, 1985.

[18] Yogesh Tugnawat and William Kuhn. Low temperature performance of cots electronic components for future mars missions. In *University of Idaho 12th NASA Symposium on VLSI Design*, 2005.

[19] RL Patterson, A Hammoud, and M Elbuluk. Assessment of electronics for cryogenic space exploration missions. *Cryogenics*, 46(2-3):231–236, 2006.

[20] Pedro Pereira, S Valtchev, João Pina, Anabela Gonçalves, M Ventim Neves, and AL Rodrigues. Power electronics performance in cryogenic environment: Evaluation for use in hts power devices. In *Journal of Physics: Conference Series*, volume 97, page 012219. IOP Publishing, 2008.

[21] Richard Patterson, Ahmad Hammoud, and Steven Scherer. Cryogenic behavior of the high temperature crystal oscillator px-570. 2011.

[22] RG Chambers and JG Park. Measurement of electrical resistivity by a mutual inductance method. *British Journal of Applied Physics*, 12(9):507, 1961.

[23] CV Dodd and WE Deeds. Analytical solutions to eddy-current probe-coil problems. *Journal of applied physics*, 39(6):2829–2838, 1968.

[24] CV Dodd. Thickness measurements using eddy current techniques. *Materials Evaluation*, 31:73, 1973.

[25] George Free. High-accuracy conductivity measurements in nonferrous metals. In *Eddy-Current Characterization of Materials and Structures*. ASTM International, 1981.

[26] AC Lynch, Anthony Edward Drake, and CH Dix. Measurement of eddy-current conductivity. *IEE Proceedings A (Physical Science, Measurement and Instrumentation, Management and Education, Reviews)*, 130(5):254–260, 1983.

[27] GR Metcalfe. The use of electrical conductivity measurements in detecting heat and fire damage in aircraft structure. In *NDT Technology in Aerospace, IEE Colloquium on*, pages 2–1. IET, 1990.

[28] KT Hartwig, CY Hua, and LC McDonald. Effect of primary coil size on eddy current decay resistivity measurements. *Cryogenics*, 31(3):153–158, 1991.

[29] Ya A Kraftmakher. Measurement of electrical resistivity via the effective magnetic susceptibility. *Measurement Science and Technology*, 2(3):253, 1991.

[30] John C Moulder, Erol Uzal, and James H Rose. Thickness and conductivity of metallic layers from eddy current measurements. *Review of scientific instruments*, 63(6):3455–3465, 1992.

[31] Erol Uzal and JH Rose. The impedance of eddy current probes above layered metals whose conductivity and permeability vary continuously. *IEEE Transactions on Magnetics*, 29(2):1869–1873, 1993.

[32] DJ Harrison, LD Jones, and SK Burke. Benchmark problems for defect size and shape determination in eddy-current nondestructive evaluation. *Journal of Nondestructive Evaluation*, 15(1):21–34, 1996.

[33] Cheng-Chi Tai, James H Rose, and John C Moulder. Thickness and conductivity of metallic layers from pulsed eddy-current measurements. *Review of scientific Instruments*, 67(11):3965–3972, 1996.

[34] Haydn NG Wadley and Bill W Choi. Eddy current determination of the electrical conductivity-temperature relation of cd1- xznxte alloys. *Journal of crystal growth*, 172(3-4):323–336, 1997.

[35] Yaakov Kraftmakher. Eddy currents: Contactless measurement of electrical resistivity. *American Journal of Physics*, 68(4):375–379, 2000.

[36] Ali M Niknejad and Robert G Meyer. Analysis of eddy-current losses over conductive substrates with applications to monolithic inductors and transformers. *IEEE Transactions on microwave theory and techniques*, 49(1):166–176, 2001.

[37] Mark P Blodgett, Chizoba V Ukpabi, and Peter B Nagy. Surface roughness influence on eddy current electrical conductivity measurements. Technical report, AIR FORCE RESEARCH LAB WRIGHT-PATTERSON AFB OH MATERIALS AND MANUFACTURING DIRECTORATE, 2003.

[38] KR Shao, YouGuang Guo, and JD Lavers. Multiresolution analysis for reconstruction of conductivity profiles in eddy current non-destructive evaluation using probe impedance data. *IEEE transactions on magnetics*, 2004.

[39] Nicola Bowler and Yongqiang Huang. Electrical conductivity measurement of metal plates using broadband eddy-current and four-point methods. *Measurement Science and Technology*, 16(11):2193, 2005.

[40] Xiandong Ma and Anthony J Peyton. Eddy current measurement of the electrical conductivity and porosity of metal foams. *IEEE Transactions on instrumentation and measurement*, 55(2):570–576, 2006.

[41] L Dziczkowski. Effect of eddy current frequency on measuring properties of devices used in non-destructive measurements of non-ferromagnetic metal plates. *Archives of Materials Science and Engineering*, 32(2):77–84, 2008.

[42] Leszek Dziczkowski. A definition of eddy current penetration depth useful for flaw detection and conductivity measurement. In *PAMM: Proceedings in Applied Mathematics and Mechanics*, volume 8, pages 10205–10206. Wiley Online Library, 2008.

[43] Javier García-Martín, Jaime Gómez-Gil, and Ernesto Vázquez-Sánchez. Non-destructive techniques based on eddy current testing. *Sensors*, 11(3):2525–2565, 2011.

[44] George Wendell Webb. Low-temperature electrical resistivity of pure niobium. *Physical Review*, 181(3):1127, 1969.

[45] Carmine Attanasio, Luigi Maritato, and Ruggero Vaglio. Residual surface resistance of polycrystalline superconductors. *Physical Review B*, 43(7):6128, 1991.

[46] M Bolore, B Bonin, Y Boudigou, S Heuveline, E Jacques, S Jaidane, F Koechlin, and H Safa. A new inductive method for measuring the rrr-value of niobium. Technical report, 1996.

[47] W Singer and D Proch. The eddy current method for rrr measurement of superconductive materials. In *Proceedings of the seventh workshop on RF superconductivity. V. 2*, 1996.

[48] H Safa, Y BOUDIGOU, E JACQUES, J KLEIN, S JAIDANE, and M BOLORE. Rrr mapping of srf cavities by a magnetometric method. In *Proc. of 8 th SRF Workshop, Abano Terme*, 1997.

[49] C Benvenuti, S Calatroni, P Darriulat, MA Peck, AM Valente, and CA Van't Hof. High-q, high gradient niobium-coated cavities at cern. In *Proc. 9th Workshop on RF Superconductivity, Santa Fe, USA*, 1999.

[50] C Benvenuti, S Calatroni, M Hakovirta, H Neupert, M Prada, AM Valente, et al. Cern studies on niobium-coated 1.5 ghz copper cavities. In *The 10th Workshop on RF Superconductivity, 2001, Tsukuba, Japan*, 2001.

[51] Kuchnir Moyses and Pierre Bauer. Apparatus for measuring rrr. Technical report, Fermi National Accelerator Lab., Batavia, IL (US), 2003.

[52] P Bauer, T Berenc, C Boffo, M Foley, M Kuchnir, Y Tereshkin, T Wokas, et al. Rrr measurements on niobium for superconducting rf cavities at fermilab. In *Proc. of 11th International Workshop on RF Superconductivity*, 2003.

[53] Z Charifoulline. Residual resistivity ratio (rrr) measurements of lhc superconducting nbti cable strands. *IEEE transactions on applied superconductivity*, 16(2):1188–1191, 2006.

[54] P Bauer, C Boffo, E Hahn, T Wokas, F McConologue, D Hicks, and M Foley. Recent rrr measurements on niobium for superconducting rf cavities at fermilab. In *Presented at*, number FERMILAB-CONF-05-298-TD, 2005.

[55] C Antoine, M Foley, and N Dhanaraj. Physical properties of niobium and specifications for fabrication of superconducting cavities. Technical report, Fermi National Accelerator Lab.(FNAL), Batavia, IL (United States), 2011.

[56] Roberto Russo. Quality measurement of niobium thin films for nb/cu superconducting rf cavities. *Measurement Science and Technology*, 18(8):2299, 2007.

[57] Waldemar Singer, Alexey Ermakov, and Xenia Singer. Rrr-measurement techniques on high purity niobium. *TTC report*, 2, 2010.

[58] Pashupati Dhakal, Gianluigi Ciovati, Peter Kneisel, and Ganapati Rao Myneni. Superconducting dc and rf properties of ingot niobium. *arXiv preprint arXiv:1202.0811*, 2012.

[59] M Darweschsad, G Friesinger, R Heller, et al. Development and test of the poloidal field prototype coil polo at the forschungszentrum karlsruhe. *Fusion engineering and design*, 36(2):227–250, 1997.

[60] M Darweschsad, G Fink, Grünhagen, and et al. Test of the euratom lct coil (nbti conductor) with forced flow he ii cooling. *Fusion engineering and design*, 45(4):361–375, 1999.

[61] John C Telinde. Strain gages in cryogenic environment. *Experimental Mechanics*, 10(9):394–400, 1970.

[62] C Ferrero. Stress analysis down to liquid helium temperature. *Cryogenics*, 30(3):249–254, 1990.

[63] Xinning Hu and et al. Output properties of fiber optic sensor for micro-displacement measurement at 77k and 4.2 k. *Cryogenics*, 49(6):302–304, 2009.

[64] M Milushev and et al. Investigation of two different types of displacement transducers in the cryogenic environment. *Cryogenics*, 44(3), 2004.

[65] KA Backes and JG Brisson. An inductive position sensor for the measurement of large displacements at low temperature. *Review of scientific instruments*, 69(2):599–602, 1998.

[66] Yaakov Kraftmakher. Eddy currents: contactless measurement of electrical resistivity. *American Journal of Physics*, 68(4):375–379, 2000.

[67] Ashraf B Islam, Syed K Islam, and Fahmida S Tulip. Design and optimization of printed circuit board inductors for wireless power transfer system. `http://dx.doi.org/10.4236/cs.2013.42032`, 2013.

[68] Janis. Janis SuperVariTemp Reservoir Cryostat. `http://www.janis.com/Products/productsoverview/SuperVariTempReservoirCryosta` 2017. Online: accessed 25 January 2017.

[69] Alexander H Slocum. Mechanisms to determine position and orientation in space, June 30 1987. US Patent 4,676,002.

[70] Pavel Kejik, S Reymond, and RS Popovic. Circular hall transducer for angular position sensing. In *Solid-State Sensors, Actuators and Microsystems Conference, 2007. TRANSDUCERS 2007. International*, pages 2593–2596. IEEE, 2007.

[71] CV Dodd and WE Deeds. Analytical solutions to eddy-current probe-coil problems. *Journal of applied physics*, 39(6):2829–2838, 1968.

[72] Leszek Dziczkowski. Eddy current measurements of surface roughness. *PAMM*, 10(1):605–606, 2010.

[73] Dominique Placko and Isabelle Dufour. Eddy current sensors for nondestructive inspection of graphite composite materials. In *Industry Applications Society Annual Meeting, 1992., Conference Record of the 1992 IEEE*, pages 1676–1682. IEEE, 1992.

[74] Peng Xu, Songling Huang, and Wei Zhao. Differential eddy current testing sensor composed of double gradient winding coils for crack detection. In *Sensors Applications Symposium (SAS), 2010 IEEE*, pages 59–63. IEEE, 2010.

[75] Hongbo Wang, Yongbin Liu, Wei Li, and Zhihua Feng. Design of ultrastable and high resolution eddy-current displacement sensor system. In *Industrial Electronics Society, IECON 2014-40th Annual Conference of the IEEE*, pages 2333–2339. IEEE, 2014.

[76] Hongbo Wang, Wei Li, and Zhihua Feng. Noncontact thickness measurement of metal films using eddy-current sensors immune to distance variation. *IEEE Transactions on Instrumentation and Measurement*, 64(9):2557–2564, 2015.

[77] Hasan Padamsee. *RF superconductivity: science, technology, and applications*. John Wiley & Sons, 2009.

[78] W Wasserbäh. Low-temperature thermal conductivity of plastically deformed niobium single crystals. *Philosophical Magazine A*, 38(4):401–431, 1978.

[79] Susan N Vernon. A single-sided eddy current method to measure electrical resistivity. *Mater. Eval.*, 46(12):1581–1587, 1988.

[80] M Bolore, B Bonin, Y Boudigou, S Heuveline, E Jacques, S Jaïdane, F Koechlin, and H Safa. A new inductive method for measuring the rrr-value of niobium. In *Proc. of the 7th Workshop on RF Superconductivity, CEA-Saclay, Gifsur-Yvette, France*, 1995.

[81] Susan N Vernon and Paul M Gammell. Eddy current method for measuring electrical resistivity and device for providing accurate phase detection, May 1 1990. US Patent 4,922,201.

[82] Fang Zhu. Development of capacitive position transducers through a mechatronic approach. 1992.

[83] S Ansermet, D Otter, RW Craddock, and JL Dancaster. Cooperative development of a piezoresistive pressure sensor with integrated signal conditioning for automotive and industrial applications. *Sensors and Actuators A: Physical*, 21(1-3):79–83, 1990.

[84] P Arun, Kuldeep Kumar, et al. Considerations for anderson-bridge experiment. *arXiv preprint arXiv:0804.3932*, 2008.

[85] Vojko Matko and Karel Jezernik. Greatly improved small inductance measurement using quartz crystal parasitic capacitance compensation. *Sensors*, 10(4):3954–3960, 2010.

[86] RamÃ3n PallÃ, John G Webster, et al. *Sensors and signal conditioning*. John Wiley & Sons, 2012.

[87] Moshiul Haque and Ernest Cox. Use of the cmos unbuffered inverter in oscillator circuits. *Texas Instruments, January*, 2004.

[88] Ron Mancini. Design of op amp sine wave oscillators. *Analog Applications*, 2000.

[89] Tianshi Wang. Analyzing oscillators using describing functions. *arXiv preprint arXiv:1710.02000*, 2017.

[90] A Cichocki and R Unbehauen. Appllication of switched-capacitor self-oscillating circuits to the conversion of rlc parameters into a frequency or digital signal. *Sensors and Actuators A: Physical*, 24(2):129–137, 1990.

[91] Emad Eldin Hegazi, Jacob Rael, and Asad Abidi. *The designer's guide to high-purity oscillators*. Springer Science & Business Media, 2006.

[92] Ramon Cerda. Pierce-gate crystal oscillator, an introduction. *Crytek Corporation*, page 1, 2008.

[93] Philippe A Passeraub, Pierre-André Besse, Christina de Raad, and Rade S Popovic. A differential relaxation oscillator as a versatile electronic interface for sensors. *Sensors and Actuators A: Physical*, 58(2):141–148, 1997.

Appendix A

Impedance measurement of cryogenic eddy current sensors using cold electronics

A.0.1 Introduction

Eddy current sensors utilize change in the impedance of the sensing element as a measure of change in the parameter measured [31, 40, 43, 73, 81]. The sensitivity and usefulness of the sensor mainly depends on the signal conditioning and signal conversion circuits which are used to measure this change [8, 82, 83]. There are mainly two different methods that are used to measure the impedance change. i.e. bridge circuits and oscillator circuits. Bridge circuits have been shown to be very useful as the measurement technique and is based on a balanced bridge (differential measurement) [84, 85]. But the main drawback of these circuits is their dependence on precisely calibrated components, a very stable excitation (current or voltage) and secondary stages of amplification. The sensed information is usually contained as voltage output as was shown in R. PallÃ et. al. (2012) [86]. This makes it susceptible to stray noise and hence added efforts are required to filter out the noise.

Whenever an eddy current sensor is used in cryogenic application, it utilizes long wires connecting sensor with signal conditioning circuits [8, 57, 80]. These interconnecting wires introduce large unpredictable errors in both inductance and series resistance. This cannot be entirely eliminated, as there is always a tem-

perature gradient along the interconnect and as a result, measurement based on balancing bridges always results in significant errors. This problem can only be eliminated if the sensor and the measurement circuit are as close to each other as possible and at the same temperature. This requires circuits that are specifically designed to operate at cryogenic temperatures.

Oscillator circuits are much simpler to design and usually contain a smaller number of components [87–89]. Oscillator circuits have shown to be much more compatible at cryogenic temperatures. Both [1, 8] have shown that oscillator circuits can be used as the variable conversion circuits for cryogenic eddy current sensor . Also, P. Sagar et. al (2017) [1] showed that LC oscillators work efficiently even at 4.2K. Using cold electronics, these oscillators can be made into an integrated sensor package operating at cryogenic temperatures which eliminates the need for long interconnectors and the associated errors. There is also an added advantage that the useful information (sensed parameter) is contained in the frequency and not in voltage [88–90]. This makes it less susceptible to stray noise and requires no additional filtering circuits.

The main drawback of using an oscillator to measure is that, sensors that utilize a change in impedance to measure certain parameter usually have two components to it. The real part (loss term) of the impedance and the imaginary part. It was shown in E. E Hegazi et. al (2006) [91] that in most of the applications, like electrical conductivity measurement, surface crack detection using eddy current sensors, both these terms are to be accurately measured and usually oscillators are a function of both. Determining or separating one from the other becomes impossible and hence it becomes useless in such applications. There have been works which suggest that a single oscillator can be used to measure both the loss term and the inductance term but certain approximations have to be made to obtain the same.

This work tries to overcome this issue by utilizing two different oscillator circuits and switching the sensing element between these two circuits. One oscillator circuit is tuned to be insensitive to the loss term of the sensing element and only sensitive towards the inductive reactance term. The other circuit is tuned to be extremely sensitive to the loss term but requires feeding of the inductance term determined from the previous oscillator. By utilizing two oscillator in tandem, we can determine both real and imaginary parts of the eddy current sensor impedance

to a high degree of accuracy. Here a planar multilayer PCB based coil is used as the sensing element which had explained in P. Sagar et. al (2017) [1]. The sensor is tested by trying to measure the change in impedance that occurs when a Nb target kept at specific distance is allowed to cool down to cryogenic temperature (77 K). This results in change in the sensing coil resistance as well as the inductance. The method is compared with a standard impedance analyzer instrument and errors are discussed.

A.0.2 LC Oscillator using unbuffered inverter

CMOS inverters have high input impedance, large gain and large bandwidth. These features make the CMOS inverter IC an ideal active component in an oscillator circuit. CMOS inverter based oscillator circuits are easy to design and occupy less space and componets than usual Op-Amp based oscillator circuits. They have an added adantage that these oscillators have also been shown to operate at 4.2 K without much change in its characteristics as shown in P. Sagar et. al (2017) [1].

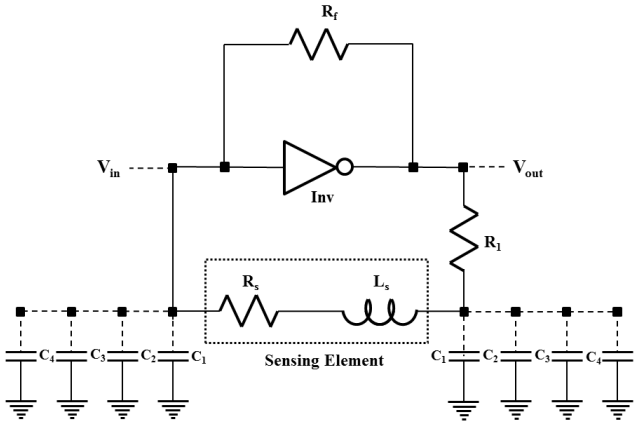

Figure A.1: LC Oscillator using unbuffered inverter

A detailed study of design of these circuits have been presented by M. Haque et. al (2004) [87]. This work derives a condition that is rarely considered while designing an LC oscillator using unbuffered inverter, i.e., the sufficient condition for the invariance of frequency with series resistance.

Condition for invariance of frequency with series resistance

Consider the circuit given in Fig. A.1. The voltage fedback into the inverter V_{in} is given by,

$$V_{in} = \frac{X_{C1}X_{C2}}{(X_{C1} + X_{LS} + R_S)(R_1 + X_{C1})}V_{out} \tag{A.1}$$

where, X_{C1},X_{C2} and X_{LS} are the corresponding capacitive and inductive reactance terms given by X_C=$\frac{1}{\omega C}$ and X_L= ωL.

$$V_{in} = \frac{V_{out}}{(1 - \omega^2 L_s C_1 + j\omega C_1 R_s)(1 + j\omega C_2 R_1)} \tag{A.2}$$

Splitting into real and imaginary terms and applying condition for oscillation, we get

$$\omega^2 = \frac{R_s}{R_1}\frac{1}{L_S C_2} + \frac{1}{L_S C_1} = \frac{1}{L_S C}(1 + \frac{Rs}{R_1}) \tag{A.3}$$

if C_1=C_2 and $R_1 >> R_s$, then

$$\omega^2 = \frac{1}{L_S C} \tag{A.4}$$

which implies that the ω becomes independent of R_S. Also from Eq. 2 the open loop gain can be calculated as,

$$|A| \geq \frac{R_1 R_s C}{L} \tag{A.5}$$

A Spice model for the inverter based oscillator was studied using LTSpice XVII and a series resistor was connected to an ideal inductor to model the effect of series resistance on the oscillator output frequency. The series resistance R_s was swept from 1Ω to 15Ω and the variation in frequency was plotted as shown in Fig. A.2. Two different conditions for $\frac{R_s}{R_1}$ was simulated and the resulting frequency outputs were plotted.

Fig. A.2 confirms that if $R_1 >> R_s$, f becomes independent of R_s. If $R_1 \simeq R_s$, then f becomes a linear function of R_s.

It has been shown by M. Haque et. al (2004)& R. Cerda (2008) [87, 92] that the effective input impedance can be adjusted by varying the feedback resistance of the circuit. Also, the inverter can be operated in a linear amplification regime by

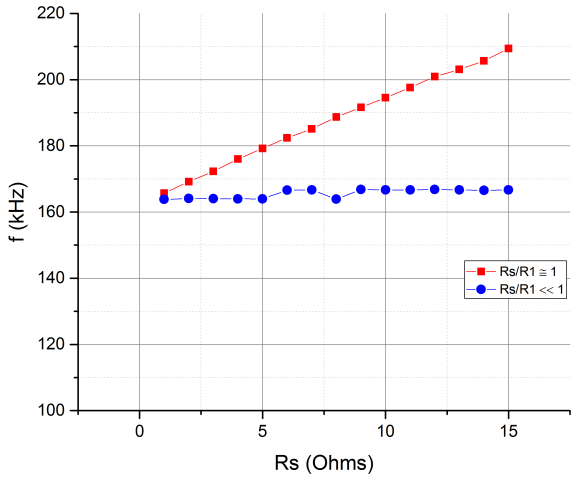

Figure A.2: Variation of frequency with R_s, keeping L_s, C and R_f constant

controlling the V_{in} to the circuit through the feedback network. It has also been reported that a NOT gate displays a fairly constant gain of around 20db and wide bandwidth sufficient for our application.

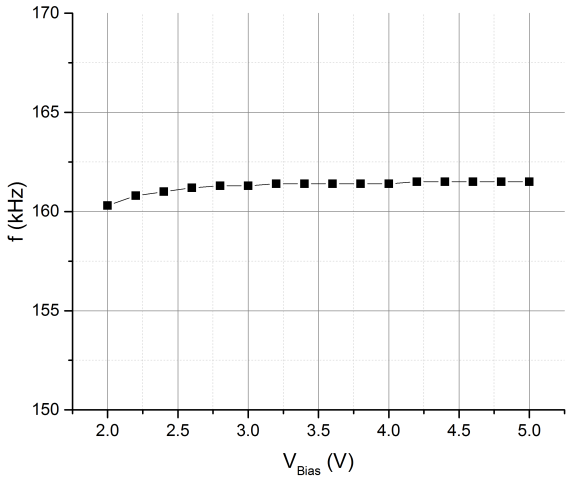

Figure A.3: Bias voltage vs frequency

The effects of bias voltage on LC oscillator is dealt in detail in M. Haque et. al (2004) [87]. Experimental results conforming the same is shown in Fig. A.3. Beyond a saturation bias voltage, the frequency becomes almost independent of it as shown in Fig. A.3.

Frequency dependent inductance

It has been established in the previous section that the LC oscillator's frequency is only a function of L and C. If C is precisely known, then L can be calculated. It should be understood that inductance also is a function of frequency. From the impedance plot of the eddy current sensor in the limited range of frequency, the inductance variation can be approximated to a second order curve fit with a high degree of accuracy.

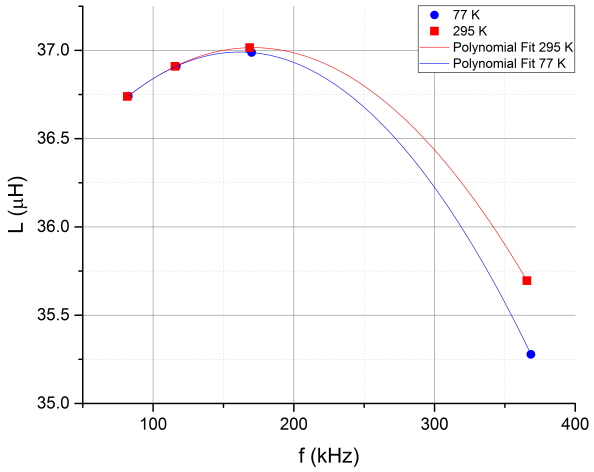

Figure A.4: Second order curve fit for inductance at 295 K and 77 K

To obtain the coefficients of the second order equation, four different capacitor sets were used. This varies the frequency of operation from a low to a high enough value. Utilizing four different capacitor combinations, four values of inductance at four different frequencies are obtained. Each set of capacitor value obeys the necessary condition for invariance with R_s and as a result errors are kept at a minimum. These inductance and frequency values are used to generate a second order curve fit as shown in Fig. A.4, which can be used to generate any intermediate inductance values within the designed frequencies. Fig. A.4 shows that at lower frequencies, both 295 K and 77 K curves are very close to each other even if the base resistance values of the sensing coils are $\sim 9\Omega$ (295 K) and $\sim 1.5\Omega$ (77 K). This again gives a clear indication that LC oscillator frequency becomes invariant of R_s.

Table A.1: Calculated Inductance compared with impedance analyzer data

	295K		
Displacement (mm)	$\mathbf{L}_{calc}$ **(μH)**	$\mathbf{L}_{meas}$ **(μH)**	**% error**
1.26	27.01	25.89	4.33
2.18	33.14	32.57	1.75
3.06	35.61	35.17	1.25
4.07	37.28	37.00	0.76
5.2	38.42	38.25	0.45

Displacement (mm)	77K		
1.26	$\mathbf{L}_{calc}$ **(μH)**	$\mathbf{L}_{meas}$ **(μH)**	**% error**
2.18	25.56	25.62	-0.23
3.06	32.25	32.48	-0.72
4.07	34.94	35.14	-0.57
5.2	36.68	36.98	-0.79

Experimental results

A Nb sample of specific dimensions (35mm × 35mm × 2mm) is used as the test target. The sample and the sensor are separated by utilizing Teflon spacers of specific thickness. The displacement is adjusted after each set of readings. The complete set of readings and its corresponding impedance analyzer data are shown is Table A.1. It can be seen that, at room temperature the error in measuring the inductance by the current method is well below 5% and the percentage error induced in the measurement increases as the distance between the sensor and target reduced. In the case of 77 K, this trend is reversed and the percentage error was found to be well below 1%. An optimum distance of 3 to 4 mm produces the best possible results with least % error in both the 77 K and 295 K region. Another point to note is that as the temperature of the sensing coil is reduced, the sensor becomes more and more like an ideal inductor. As a result, the errors associated with inductance measurement becomes significantly less at lower temperatures as can be seen from Table A.1.

A.0.3 Relaxation oscillator

A detailed analysis of a relaxation oscillator as a signal conditioning circuit for an inductive sensor is discussed by P. A. Passeraub et. al (1997) [93]. In this paper,

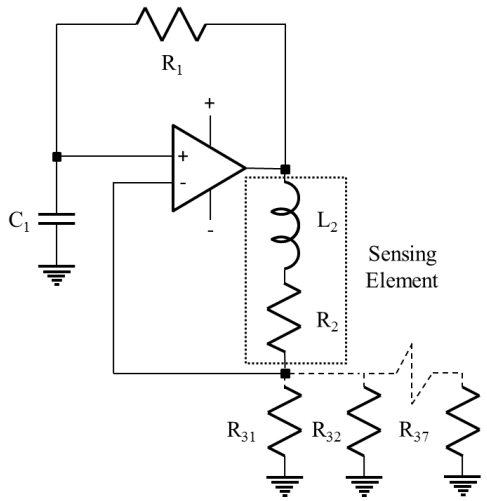

Figure A.5: Relaxation oscillator

we concentrate on negating some of the drawbacks reported by P. A. Passeraub et. al (1997) [93]. It must be understood that the series resistance (R_2) in Fig. A.5, has been varied and studied in [93], is a function of frequency itself meaning $R_2 = R_2(\omega)$. Again R_2 is a function of electrical conductivity of the target material, lift off distance and many other factors. If the sensor is designed to measure electrical conductivity (σ) of a target material, then R_2 becomes a strong function of σ. For an eddy current sensor designed to operate at cryogenic conditions, R_2 also becomes a strong function of temperature $R_2 = R_2(T)$ as the coil resistance will drastically decrease with temperature. Considering all these factors, both the components of impedance of the coil ($Z = R_2(\omega)+X_2(\omega)$) cannot be determined simultaneously by using a single relaxation oscillator circuit.

The equation for inductance calculation for a relaxation oscillator as shown in Fig. A.5 is given by,

$$L_2 = T\frac{R_2 + R_3}{4}\frac{1}{arctanh(\frac{R_2+R_3}{R_3}tanh(\frac{T}{4R_1C_1}))} \tag{A.6}$$

It can be seen that Eq. 6 which dictates the value of L_2 is a strong function of R_2. It means that we cannot effectively calculate the value of inductance until and unless an accurate value of $R_2(\omega)$ is known. we approach this as an inverse problem. Here, we utilize an LC oscillator circuit (described in previous section) and different capacitor combinations to calculate the function $L_2(\omega)$. This $L_2(\omega)$

at the oscillating frequency of relaxation oscillator is utilized to determine the value of R_2 which satisfies Eq. 6 within a defined degree of tolerance. This value of R_2 will be the series resistance of the eddy current sensor. The accuracy of measuring series resistance of inductor is dependent on the value of the switching resistance R_3. Selection of R_3 is found to be a function of the displacement between the sensor and the target. As a thumb rule, smaller displacements require smaller values of R_3 and vice versa.

Table A.2: Series resistance (R_S) at two different temperature for Nb sample

1 mm gap at 295K			
R3	**$R_s$measured**	**$R_s$calculated**	**%delta**
14.717	9.324	8.435	9.539
13.403	9.455	8.737	7.590
12.827	9.523	8.882	6.728
12.418	9.577	8.987	6.157
11.608	9.699	9.205	5.097
9.113	10.312	9.976	3.260
8.829	10.422	10.050	3.570
1 mm gap at 77K			
R3	**$R_s$measured**	**$R_s$calculated**	**%delta**
14.717	1.698	1.362	19.789
13.403	1.728	1.454	15.857
12.827	1.743	1.495	14.251
12.418	1.756	1.531	12.805
11.608	1.784	1.610	9.764
9.113	1.927	1.920	0.383
8.829	1.953	1.960	0.342

Algorithm for deducing series resistance R_2

A flow chart showing the process of calculating the series resistance R_2 is given in Fig. A.6. The entire process is divided into two cycles. 1) an inductance determining cycle 2) series resistance determining cycle. In each of the cycle, the sensing element is switched to that specific oscillator through a multiplexer circuit. In inductance determining cycle, four capacitors are switched one after the other and the frequencies are fed to a curve fit algorithm, which generates a second order fit. Once a fit is generated, the sensor is connected to the relaxation

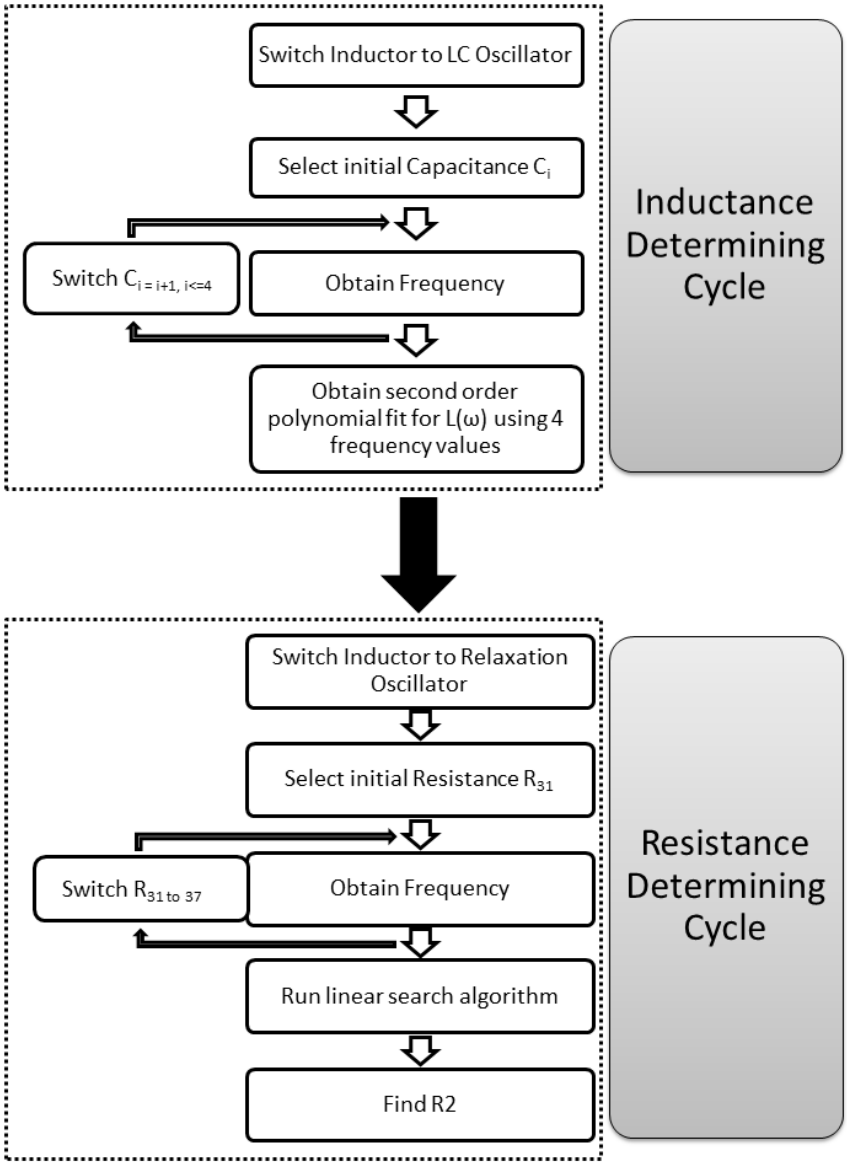

Figure A.6: Algorithm for measuring R_2

oscillator circuit. This circuit has a set of 7 resistors for R_3 (R_{31}-R_{37}). These were measured with high degree of accuracy using a nanovoltmeter and programmable current source. The initial value of the R_3 is set at the highest value and the frequency is acquired by the program. Similarly all the seven set of frequencies are acquired.

$$\%Tol \leq \frac{L_{2_{curve\ fit}}(\omega) - L_2(R_2, R_3, \omega)}{L_2(\omega)} \tag{A.7}$$

Next step involved is to send the (R_{3X}, ω , $L_{2_{curve\ fit}}$ (ω)) through a linear search algorithm designed to minimize the error when the value R_2 is changed. First a coarse search is done so that the value of R_2 with the given set of (R_{3X},frequency (f), L_2(f)) produces a pure real number. Once this condition is satisfied, a fine search is done, which brings the error down to within a defined tolerance value. The condition for termination of the loop is given by Eq. 7.

Experimental results

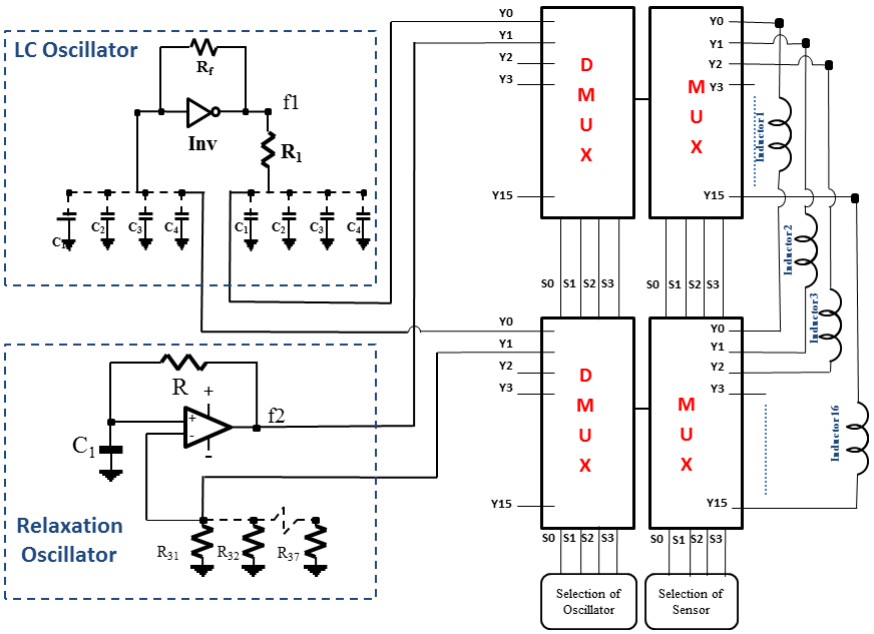

Figure A.7: Circuit for measuring impedance

A representative sample data set for the change in series resistance of the eddy current sensor calculated by the above described technique is given in Table A.2. It can be seen that at 1 mm displacement with a Nb target, the percentage error at room temperature is less than 5%. This can be attributed to higher error associated with inductance measurement with lower separation at room temperature. The percentage errors are less than 1% for 3-4 mm separation as the errors associated with inductance measurement is less than 1%.

The case is much improved for 77 K measurement. It can be seen from Table A.2, that at 1 mm, separation the percentage error associated with R_2 measurement is less than 0.5%. This makes it an ideal way to effectively measure the change in impedance of the coil for cryogenic eddy current sensor applications.

A.0.4 Circuit used for impedance measurement

The complete circuit that was used to measure the impedance of the eddy current sensor is shown in Fig. A.7. Two sets of cryo-compilable MUX IC's are used to switch between the oscillator circuits and between the different sensing elements. This was done to obtain the reference impedance at that specific temperature. This is required for generating the normalized impedance plots.

A.0.5 Conclusion

A dual switched oscillator technique for measuring the impedance of a planar eddy current cryogenic sensor was successfully demonstrated for two different temperatures. An LC oscillator using an unbuffered inverter was analyzed and a condition for invariance of frequency with a change in series resistance of the sensor was established. Spice simulation was done to confirm the same. Utilizing the designed conditions, and for a set of pre-calibrated capacitors, an inductance plot (variation of inductance with frequency) was determined and compared with impedance analyzer values. It was able to accurately measure inductance even with large changes in series resistance R_2. A relaxation oscillator circuit was used in conjunction with the previously determined inductance plot to calculate the series resistance R_2. This involved utilizing a linear search algorithm to effectively search for the value of R_2 that gives the least error in calculating inductance. Utilizing the two oscillators in tandem, the impedance of the eddy current sensor with a Nb target was calculated at two different temperatures and the percentage errors were determined by comparing them to an impedance analyzer data.

A.0.6 Linear search algorithm flow chart

A flow chart depicting the algorithm used to determine the series resistance is shown in Fig. A.8. The algorithm was implemented as a subroutine in MATLAB

and called from inside the DAQ program in LabVIEW after acquiring frequency.

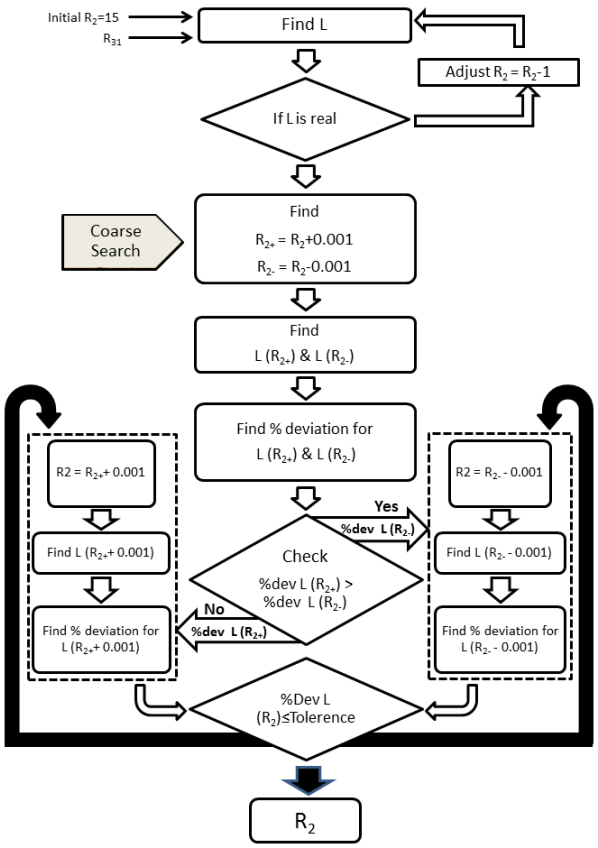

Figure A.8: Flow chart for linear search algorithm

Usually, around 120-150 iterations results in convergence of the algorithm towards the minimum error. The percentage tolerance selected for this experiment was 0.01%. This resulted in measurement errors which were less than 0.5%.

Appendix B

Error analysis

Whenever a measurement is made, there are two basic kinds of uncertainties, systematic and random uncertainties. Systematic uncertainties are those due to faults in the measuring instrument or in the techniques used in the experiment. Random uncertainties are associated with unpredictable variations in the experimental conditions under which the experiment is being performed, or are due to a deficiency in defining the quantity being measured. Of these two types of uncertainties, random uncertainties are much easier to deal with and to quantify. There is no general procedure for estimating the magnitude of systematic uncertainties as there is for random uncertainties. Only an experimenter whose skill has come through long experience can consistently detect systematic uncertainties and prevent or correct them. If an experiment has low systematic uncertainty it is said to be accurate. If an experiment has low random uncertainty it is said to be precise.

Random uncertainty is often associated with the concept of standard deviation. To understand these concepts, first we have associate it with arithmetic mean of measurement. The mean of a set of numbers is defined as the sum of all the numbers divided by the number of them. In our experiment, if we measure the frequency output at a fixed temperature and fixed position of a sensor N different times, if f_1, f_2, ... f_N are the values of frequencies measured each time, then,

$$f_m = \frac{f_1 + f_2 + ...f_N}{N} = \frac{1}{N}\Sigma_{i=1}^{N} f_i \tag{B.1}$$

A widely accepted quantitative measure of scatter is the sample standard devia-

tion, f_s. For the special case where all data points have equal weight, the sample standard deviation is defined by the equation,

$$f_s = \sqrt{\frac{\Sigma_{i=1}^{N} (f_i - f_m)^2}{N-1}} \tag{B.2}$$

The standard deviation f_s defined by equation B.2 provides the random uncertainty estimate for any one of the measurements used to compute f_s. The mean value of the measurements have less random uncertainty than any one of the individual measurements. It can be shown that the standard deviation of the mean value of a set of measurements σ_{fm} is given by,

$$\sigma_{fm} = \sqrt{\frac{\Sigma_{i=1}^{N} (f_i - f_m)^2}{N(N-1)}} = \frac{f_s}{\sqrt{N}} \tag{B.3}$$

All the uncertainties in measurements in the current thesis are measured through these steps and the reported errors are the mean standard deviation in measurement σ_{fm}.

Appendix C

LabVIEW programs to acquire data from the different sensors

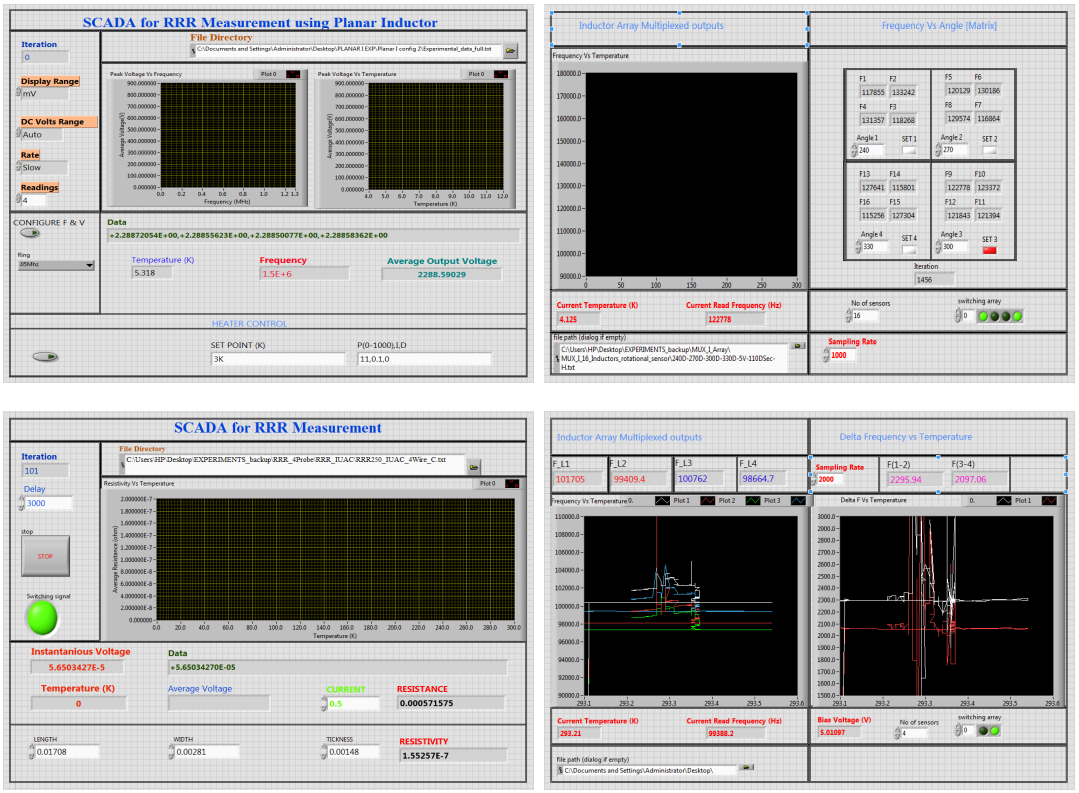

Figure C.1: SCADA front panel for the different LabVIEW programs

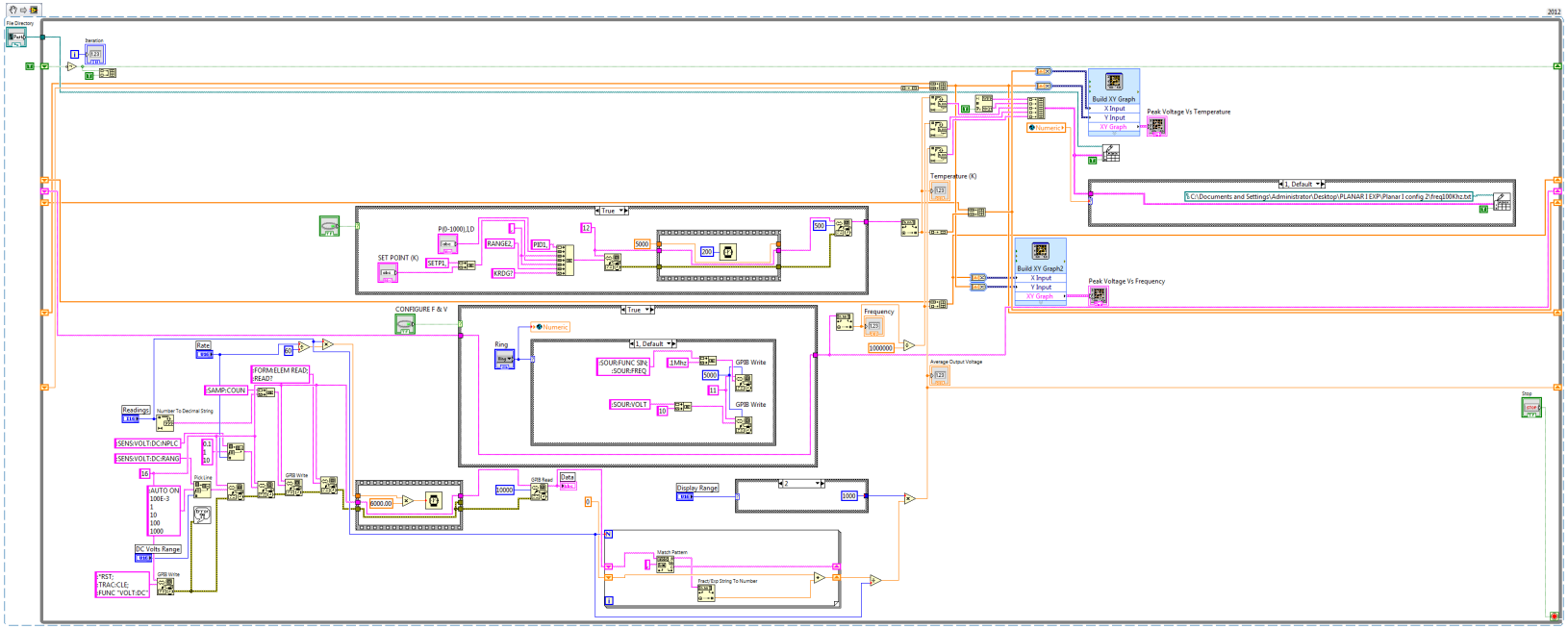

Figure C.2: LabVIEW program back panel for acquiring output frequency from the cryogenic position sensor

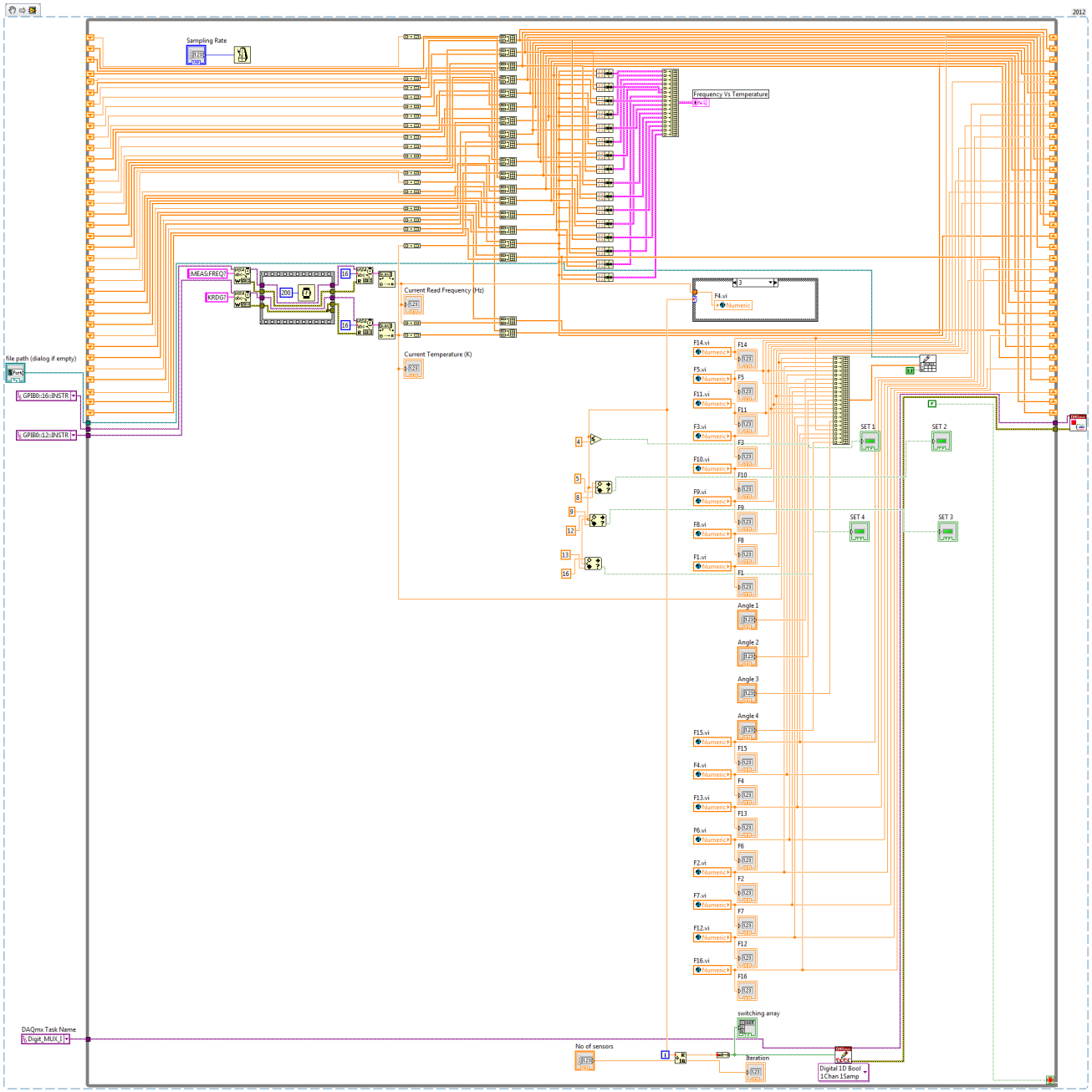

Figure C.3: LabVIEW program back panel for acquiring output frequency from sixteen inductors used for angular position measurement

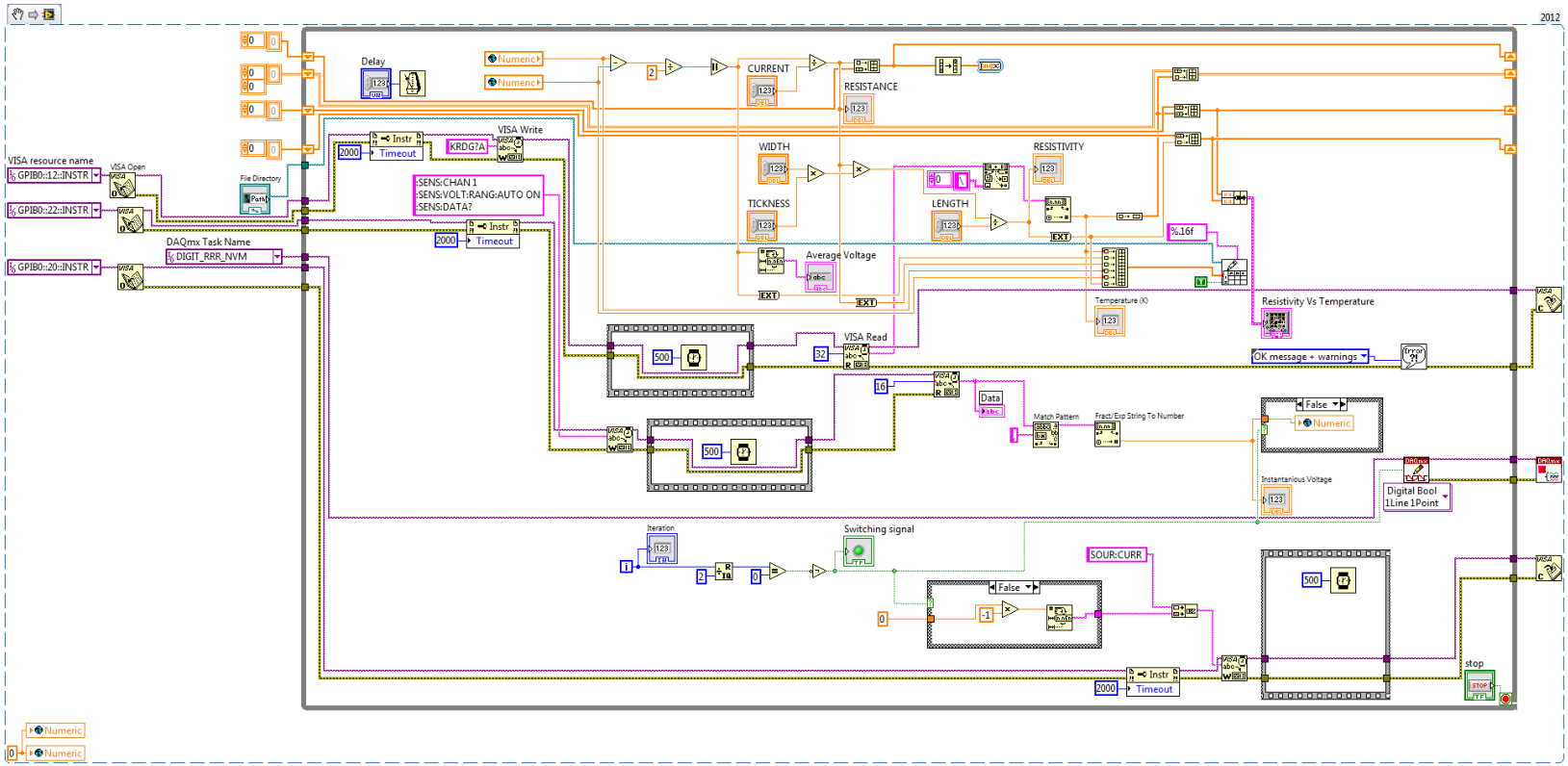

Figure C.4: LabVIEW program back panel for acquiring restisivity values using 4-probe measurement method

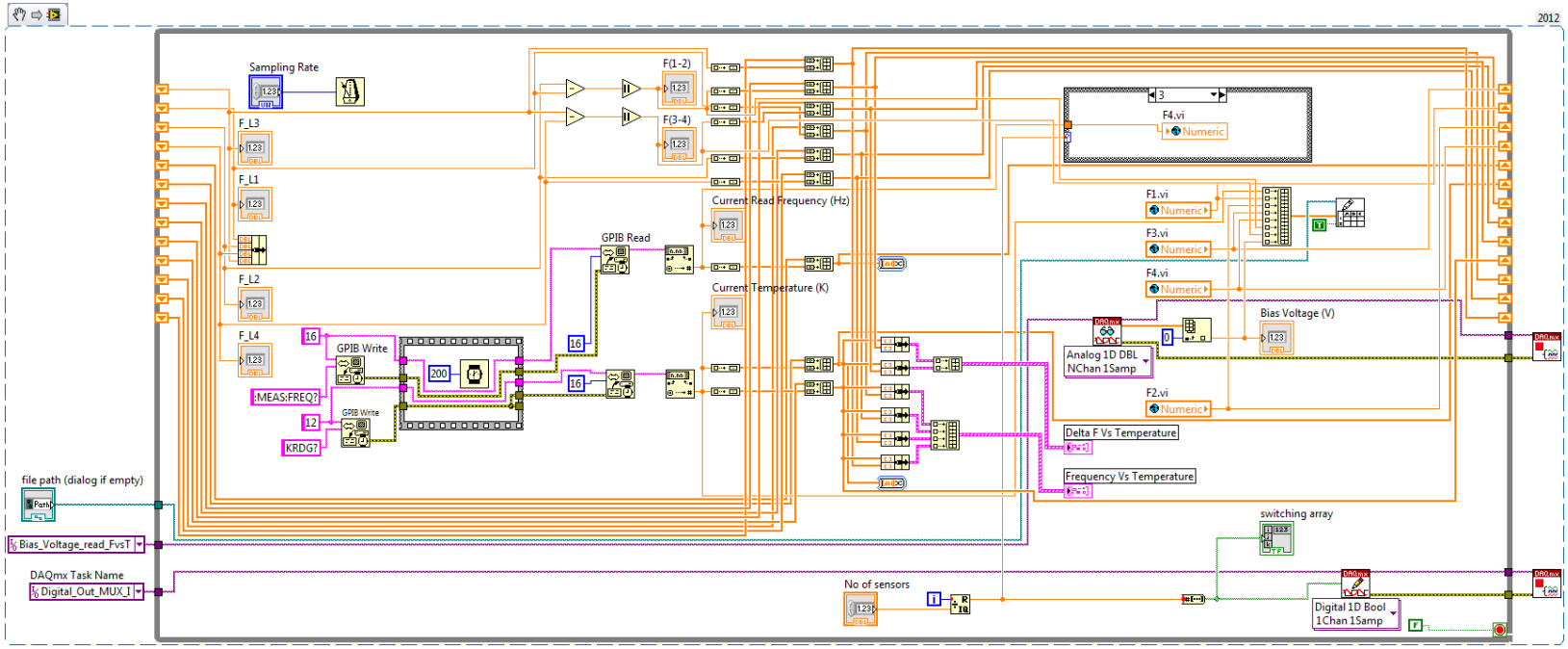

Figure C.5: LabVIEW program back panel for acquiring output frequency from four inductors in order to measure RRR using mutiplexed LC oscillator circuit